A FIELD THEORETIC APPROACH TO ROUGHNESS CORRECTIONS OF CASIMIR ENERGIES

BY

HUA-YAO WU

A Dissertation submitted to the

Graduate School—Newark

Rutgers, The State University of New Jersey

in partial fulfillment of the requirements

for the degree of

Doctor of Philosophy

Graduate Program in Physics

Written under the direction of

Martin Schaden

and approved by

Newark, New Jersey

October, 2014

ABSTRACT OF THE DISSERTATION

A Field Theoretic Approach to Roughness Corrections of Casimir Energies

by

Hua-Yao Wu

Dissertation Director: Martin Schaden

A systematic field theoretic description of the surface roughness corrections to the Casimir effect is developed. I use the multiple-scattering formalism. The Casimir energy is expressed in terms of the free Green's function and single-body scattering matrix. Finite temperature corrections to the Casimir force are obtained by Matsubara's formalism. The leading thermal corrections at high and low temperatures are presented and discussed. A statistical description of surface roughness is given and I construct the generating functional for roughness correlations. The latter allows me to incorporate roughness in a Quantum Field Theoretic (QFT) framework.

I first consider a massless scalar field in the presence of parallel plates where one of which has a rough surface. In this case, semi-transparent boundary conditions are imposed by δ-function potentials. In the strong coupling limit the δ-function potential imposes Dirichlet boundary conditions. The Feynman rules of this equivalent $2+1$-dimensional model are derived and its counterterms constructed. The two-loop contribution to the free energy of this model gives the leading roughness correction to the Casimir energy. The resummation of high-momentum loops shows that roughness effectively leads to a change in the mean separation of the order σ^2/l_c and reduces reflection.

The scalar model subsequently is generalized to the electromagnetic case. I derive the dielectric roughness corrections to the electromagnetic Casimir energy in a perturbative framework of the effective low-energy field theory for dielectric materials of Schwinger. It describes the interaction of electromagnetic fields with materials whose plasma frequency ω_p sets the low-energy scale. I show that the perturbative expansion of the single-interface scattering matrix in the amplitude of the profile is sensitive to short-wavelength components of the roughness correlation function. Generalized counterterms are introduced to subtract and correct these unphysical high-momentum contributions to the loop expansion. To leading perturbative order, the counterterms reproduce the phenomenological plasmon model. The renormalized low-energy theory is insensitive to the high-momentum behavior of the roughness correlation function and remains finite in the uncorrelated ($l_c \to 0$) limit. I compare these predictions with the unrenormalized model and with experiment.

Acknowledgements

First and foremost, I would like to thank my thesis adviser, Dr. Martin Schaden, who has provided me valuable guidance, full support and strong encouragement all along my Ph.D. studies. His constructive criticisms and amazing physics intuition always led me into the regions of thought that would not have been explored otherwise. It has been an honor of mine to be his first Ph.D. student. Dr. Schaden will always be my mentor in physics.

Most of the work presented here was done in collaboration with Dr. Schaden, Dr. K. V. Shajesh, and Junming Liu. I would like to express my sincere gratitude to each of our group members for their discussions and invaluable input. I also want to thank my Ph.D. dissertation committee members - Dr. Zhen Wu, Dr. Daniel Murnick, Dr. Keun H. Ahn, and Dr. Vitaly A. Shneidman - for their time and support.

I am indebted to my parents, Bo-Min Wu and Bing-Ru Shen, and my cousins, Guan-Ying Shen and Guan-Xiong Shen. Your unconditional love, whole-hearted support, and continuous faith in me have enabled me to discover my potentials, achieve my goals and fulfill my dream.

Last but not least, my time at Rutgers was made enjoyable in large part due to my friends. I owe thanks to them all, and especially to Scott Y. Lin, Felix Chuang, Nai Yun Hsu, Wen Yu Song, Ying Han Chen, An Cheng Ruo, Holly Chiu, Tzu Tai, Tiffany Chiu, and Wei Hao Huang; your warm friendship and support will always be cherished. I would like to express my special appreciation for my girlfriend Victoria Chiu who stuck with me during the long months of writing,

your company and invaluable encouragement are my most precious supports in those days, thank you for standing by me throughout this journey.

Dedication

I dedicate this thesis to my father, Bo-Min Wu, my mother, Bing-Ru Shen and myself.

Table of Contents

List of Figures

Chapter 1
A brief introduction to the Casimir effect

In 1948 [5], Dutch physicist Hendrik Casimir first demonstrated that two neutral parallel conducting plates in vacuum attract. The origin of this attractive force can be traced to the quantum mechanical effect that a perfect vacuum is still filled with unavoidable fluctuations of the electromagnetic field due to the Heisenberg uncertainty principle. The dependence of this zero point energy on the separation of two parallel plates results in the Casimir force between them. This fluctuation-induced force is the electromagnetic dominant force at submicron scales. However, due to the lack of experimental evidence, this unexpected new discovery received relatively little attention in the following decades. The first convincing experimental evidence was presented four decades after Casimir's prediction of this long-range electromagnetic force. Lamoreaux in 1997 [6], measured the Casimir force of a torsion pendulum at distances of 0.6 to 6 micrometers in good agreement with the theoretical prediction. The subsequent irrefutable experimental confirmation of the Casimir force in the submicron regime using Atomic Force Microscopy (AFM) techniques, since then has widespread implications from fundamental physics to nanothecnology as well as in chemistry and biology.

The following is a brief survey of major theoretical and experimental developments in this field. The rest of this Chapter will be organized as follows. In Section 1.1, I present, historically, how Casimir first came up his ideas of fluctuation-induced quantum force, Casimir force, and its close connections with the van der Waals force. Section 1.2 shows the UV divergence problem in the calculation of vaccum energy of multiple objects. I will discuss the origin of this problem and different treatments. Section 1.3 presents the material and geometry effects on Casimir energy. Section 1.4 introduce the major experimental advances with slight emphasis on the influence of surface roughness for measureing the Casimir force.

1.1 The Casimir Effect - A Fluctuation-induced Force

1.1.1 Casimir-Polder interaction

One of the unique aspects of quantum mechanics is Heisenbergs uncertainty principle. It implies spontaneous changes of quantum fields, so-called quantum fluctuations, that give rise to various phenomena such as spontaneous emission, the Lamb shift and the Casimir effect. The first example of a fluctuation-induced interaction between nonpolar molecules was given by Fritz London in 1930 [7, 8]. He used second-order perturbation theory in the Coulomb interaction between the electrons and nuclei of two atoms forming a dimer. He found that the distribution of the electrons of an atom forms spontaneous dipoles that instantaneously induce polarization of nearby atoms and results in an attractive force between them. The interaction energy decreases with the separation of two atoms as $1/R^6$ and is given by,

$$E_{London} \sim -\frac{\hbar}{R^6}\int_0^\infty d\omega\ \alpha_1(\omega)\alpha_2(\omega), \tag{1.1}$$

where R is the separation distance between two dipoles and α_1, α_2 are the dipole polarizabilities of the respective atoms. This is London's famous explanation for the attractive interaction Van der Waals [9] postulated almost 20 years earlier to explain the liquid-gas phase transition. However, when Verwey and Overbeek studied the stability of colloidal dispersions and its dependancy on the ionic strength of the electrolyte [10], they found that the attractive interaction must fall faster than the London potential of Eq.(1.1) predicts. Overbeek pointed out that the deviation must be due to relativistic retardation effects due to the finite speed of light. Eq.(1.1) is the limit of the attractive force when the separation are much smaller than the wavelength (c/ω) of the atomic frequencies. Heuristically one can argue for a cutoff of the order of c/λ in the frequency integral of Eq.(1.1) [11], since the orientation of dipoles at higher frequencies essentially are uncorrelated. Casimir and Polder considered this retardation effect [12] in their calculations of the attractive force between two atoms quantitatively. Their result is now known as the Casimir-Polder force,

$$E_{Casimir-Polder} = -\frac{23\hbar c}{4\pi}\frac{\alpha_1\alpha_2}{r^7} \tag{1.2}$$

The interaction in Eq.(1.2) is not only of a quantum but also of a relativistic nature. The relativistive correction to the van der Waals interaction increases with the separation and retardation dominates for atomic separations greater than a hundred nanometers. The faster $1/R^7$ decrease is consistent with Verwey and Overbeek's experimental observations.

1.1.2 Vaccum energy

As we have seen, the van der Waals force is closely related to the Casimir-Polder force which is its retarded version to the interaction between macroscopic dielectric objects. Following the work of [12], Casimir sought a more elementary derivation of this result. He was inspired by the results because the simplicity of Eq.(1.2). In 1947, he visited Copenhagen and introduced his work on the retarded van der Waals force to Neils Bohr mentioning his quest for a "simpler and more elegant derivation." Neils Bohr suggested a connection between the Casimir's effect and the zero-point energy (ZPE). This comment motivated another paper published in the same year by Casimir, as the sole author, entitled *On* *the attraction between two perfectly conducting plates.* This short paper, all of two and a half pages long, concludes that there is an attractive force exerted between two perfect metallic plates due to the vacuum state energy [5]. In the paper, instead of a description in terms of fluctuating *dipoles*, Casimir calculated the ZPE of the fluctuating electromagnetic *fields* in the presence of the two plates. This change in the point of view requires one to consider the quantized local action of fields in the framework of quantum field theory.

In quantum field theory, quantized free fields, such as the electromagnetic field, can be described by a set of oscillators of all frequencies. The energy of each mode is given by the harmonic oscillator energy $E_n = \hbar\omega(n + \frac{1}{2})$ where $\hbar\omega$ is the energy of a single quantum, and $n = 0, 1, 2, ...$ is the number of them. The zero point energy of the ground (vacuum) state with n = 0 quanta thus is

$$E_0 = \sum_j \frac{1}{2}\hbar\omega_j, \tag{1.3}$$

where j represents the quantum numbers of a field mode. For the free electromagnetic field in Minkowski space, the modes are labeled by a continuous wave vector $\mathbf{k}$ with $\omega(\mathbf{k}) = c\mathbf{k}$ and E_0 is infinite. In bounded regions, such as a box, only some discrete wave vectors satisfy the boundary conditions,

$$E_{0b} = \sum_{\mathbf{k}} \frac{1}{2}\hbar\omega_{\mathbf{k}} \qquad \text{with discrete } \mathbf{k}. \tag{1.4}$$

Although the sum in Eq.(1.4) is also ultraviolet divergent, differences between such *infinite* energies may be finite.

1.2 Regularization

The vacuum energy due to ZP-fluctuations in general is infinite. The UV divergences arise from infinite degrees of freedom of fluctuating quantum fields. In quantum field theory, these arise from ultraviolet contributions to loop integrals.

To extract physical information from ultraviolet divergent theories, various regularization and renormalization procedures were developed. In general, one first introduces a regularization that yields finite expressions and chooses parameters of the model to reproduce some experimental data. The regularization is then removed while adjusting the model parameters so that the chosen data are reproduced. A renormalizable theory generally only requires a finite, fixed number of data as experimental input and yields finite correlation functions in this limit.

In non-renormalizable effective low-energy field theories such the one we are considering depend on an infinite number of parameters. To render the model insensitive to UV-effects, generally [13] requires input of an infinite amount of experimental data. As we will see below, such effective low-energy field theories nevertheless retain some predictive power in the infrared, i.e. used judiciously, they can accurately predict low-energy experiments.

1.2.1 Single body

To obtain finite UV-independent contributions to the Casimir energy of a single contiguous body in an effective model, various regularizations and subtractions have been proposed. The standard UV-analysis treatments with special approaches are required because of the presence of boundaries. The heat kernel expansion [14, 15], which is the asymptotic expansion of the spectral function for high temperatures. It is related to (generalized) *zeta function regularization.* In this approach, one changes the power of the frequency, $\omega_{\mathbf{k}}$, in the mode sum of Eq.(1.3) as,

$$E_0(s) = \frac{\alpha^{2s}}{2} \sum_j \omega_j^{1-2s} \tag{1.5}$$

where the α is an factor introduced to maintain dimensionality. The expression Eq.(1.5) converges for $Re[s] > 3/2$. To proceed, we replace the powers of the frequency by integral,

$$\omega_j^{1-2s} = \int_0^\infty \frac{d\beta}{\beta} \frac{\beta^{s-\frac{1}{2}}}{\Gamma(s-\frac{1}{2})} e^{-\beta\omega_j^2} \tag{1.6}$$

and rewrite Eq.(1.5) as,

$$E_0(s) = \frac{\alpha^{2s}}{2} \int_0^\infty \frac{d\beta}{\beta} \frac{\beta^{s-\frac{1}{2}}}{\Gamma(s-\frac{1}{2})} H(\beta) \tag{1.7}$$

where

$$H(\beta) = \sum_j e^{-\beta\omega_j^2} \tag{1.8}$$

is the *heat kernel* which normally refers to the solution of the heat conduction equation. The heat kernel expansion for small β (high temperatures) is related to the Casimir effect because it reveales the divergences of the vacuum energy integral for small β. We see this by expanding $H(\beta)$ asymptotically for small β,

$$H(\beta) = \frac{1}{(4\pi\beta)^{3/2}} \Big(a_0 + a_{1/2}\sqrt{\beta} + a_1\beta + a_{3/2}\beta^{3/2} + ... \Big) \tag{1.9}$$

the constants $a_0, a_{1/2}, ...$ are the *heat kernel coefficients.* Consider a system having a volume V bounded by a surface S with a background field $U(\mathbf{r})$. The heat kernel coefficients in this case can be represented as a sum of two local, surface and volume, integrals,

$$a_{k/2} = \int_V d\mathbf{r} b_{k/2}(\mathbf{r}) + \int_S d\mu(\eta) c_{k/2}(\eta). \tag{1.10}$$

where η is a coordinate on the surface. $b_{k/2}$ and $c_{k/2}$ are functions of the local field $U(\mathbf{r})$ living in bulk V or on the surface S. They depend only on topological characteristics of the system and on boundary comditions. Combine the Eq.(1.9) and Eq.(1.5), the integration of Eq.(1.7) in the interval $\beta \in [0, 1]$ leads to the divergent part of the vaccum energy in terms of the regularization parameter δ [16],

$$E_0^{div}(\delta) = \frac{3a_0}{2\pi^2}\frac{1}{\delta^4} + \frac{a_{1/2}}{4\pi^{3/2}}\frac{1}{\delta^3} + \frac{\bar{a}_1}{8\pi^2}\frac{1}{\delta^2} + \frac{\bar{a}_2}{16\pi^2} ln\ \delta. \tag{1.11}$$

where $\bar{a}_1 = a_1, \bar{a}_2 = a_2$ for massless fields. All terms in Eq.(1.11) diverge for $\delta \to 0$. The coefficents proportional to the volume, surface area , etc. are associated with the system geometry. To remove the divergences, one normally has to introduce corresponding counterterms in the volume, surface area etc. contributions to the total energy of the system and redefines the bare parameters of the model by physical ones obtained from measured values. In Eq.(1.11), a_0 is the volume of the domain and $a_{1/2}$ is the surface area of its boundary. a_1 reflects the average curvature and topological characteristics. The geometric origin of a_2 on the other hand is hard to describe because the associated divergence is logarithmic. Resolving this ambiguity usually requires the introduction of an external length scale from the high energy regime that makes low-energy predictions of the model dependent on the scale at which high-energy contributions are subtracted. Case by case considerations in this case are necessary for different configurations.

1.2.2 Two disjoint bodies

As we discussed in the last section, divergences of the vacuum energy can be expressed through the heat kernel coefficients in Eq.(1.11). These coefficients are represented by Eq.(1.10) as integrals over local potentials and topological features. The removal of these divergences is not trivial for a single body systems. However, if only interaction forces between *disjoint objects* are of interest, the divergences can be removed by a geometrical subtractions [17] procedure that does not depend on the UV-regularization. The idea of the "geometric" operation can be traced back to Power [18] who used it to calculate the Casimir force between parallel metallic plates without employing any intermediate regularization. Svaiter [19] recognized and succinctly emphasized the physical nature of this scheme.

The total energy E_{12} of a two body system may be decomposed as,

$$E_{12} = E_0 + \Delta E_1 + \Delta E_2 + \Delta E_{12} \tag{1.12}$$

where E_0 is the energy of empty space without objects, ΔE_1 and ΔE_2 are the changes in the total energy in the presence of either body and ΔE_{12} is the change in energy due to their interaction. To see the subtraction procedure, we rearrange Eq.(1.12) as,

$$\begin{aligned} \Delta E_{12} &= E_{12} - E_0 - \Delta E_1 - \Delta E_2 \\ &= E_{12} - (E_0 + \Delta E_1) - (E_0 + \Delta E_2) + E_0 \\ &= E_{12} - E_1 - E_2 + E_0 \end{aligned} \tag{1.13}$$

The expression Eq.(1.13) gives the interaction energy of interest in terms of one-body vacuum energies only. E_1, E_2 now are the total energies of either single body present in the vaccum and E_{12} is that of the single body consisting of both objects. Each of them possess the divergences exactly expressed in form of Eq.(1.11). The local heat kernel coefficients in Eq.(1.11) do not contain any information about the other objects nor the distances between them. The local nature of ultraviolet divergences thus implies the complete cancellation of infinite parts between E_0, E_1, E_2 and, E_{12}. The singularites arising from the complex shape of the individual objects are subtracted in this linear combination and the procedure does not depend on the regularization. This geometric treatment was extended to calculate the Casimir interaction for many body systems [20]. The N-body interaction energies were shown [21] to be finite as long as not all N objects intersect at a common point.

1.3 Geometry and material effects

Kenneth and Klich, in 2006 [22], computed the two bodies interaction Casimir energy, ΔE_{12} in Eq.(1.13), from the functional determinants of disjoint potentials. They obtain the interaction energy

$$\Delta E_{12} = \frac{1}{2}\int_{-\infty}^{\infty} \frac{d\zeta}{2\pi} \mathrm{Tr}\ \ln\Big[1 - G_0 T_1 G_0 T_2\Big] \tag{1.14}$$

in terms of the free Green's function, G_0, and the scattering matrices, $T_1,\ T_2$, associated with the individual objects. The result is not only formally concise but also physically revealing. It connects this abstractive quantum effect to the relatively transparent classical notion of "light scattering". As the theory demonstrates, the Casimir force between interacting objects can be found if the electromagnetic scattering matrices of each individual object are known. The one-body scattering matrices T_i in Eq.(1.14) contain all the geometic and material information on each single body relevant to the scattering of electromagnetic waves and imply how the Casimir force depends on these characteristics. Because the computation of electromagnetic scattering matrices is difficult, the calculation of the Casimir energy for geometries and configurations other than parallel plates with real materials and surface roughness remains difficult.

In 1956, Lifshitz [23, 24] generalized Casmir's original work of the ideal metal and developed a macroscopic theory for two semi-infinite slabs of materials with known dielectric permittivity separated by vaccum,

$$E_L = \frac{1}{(2\pi)^2}\int\int d^2\mathbf{k}d\zeta\Big\{ln\Big[1 - r_{TE}^2 e^{-2a\kappa}\Big] + ln\Big[1 - r_{TM}^2 e^{-2a\kappa}\Big]\Big\} \tag{1.15}$$

Here a is the distance between the two slabs and r_{TE}, r_{TM} are the familiar Fresnel reflection coefficients,

$$r_{TE} = \frac{\kappa - \kappa_\varepsilon}{\kappa + \kappa_\varepsilon}, \qquad r_{TM} = \frac{\varepsilon\kappa - \kappa_\varepsilon}{\varepsilon\kappa + \kappa_\varepsilon} \tag{1.16}$$
$$with \quad \kappa^2 = k^2 + \zeta^2, \qquad \kappa_\varepsilon^2 = k^2 + \varepsilon\zeta^2$$

The theory provides a unified description of the Van der Waals and the Casimir interaction between planar dielectrics at zero temperature. Schwinger in 1978 [25] extended Lifshitz's results to include the finite temperature correction to the force in the framework of an effective low energy field theory.

The Casimir energy of non-planar configurations have also been investigated. The first Casimir energy of a curved geometry was obtained by Boyer in 1968. Casimir in 1953 [26] had suggested that the repulsive force on a charged sphere (a model for an electron) might be balanced by an attractive Casimir force. Boyer calculated the surface tension due to the Casimir force on a perfectly conducting spherical shell [27] but found it is repulsive. The result was unexpected but different methods, such as the multiple-reflection expansion (Balian and Duplantier 1977 [28]), the Green's function method (DeRaad and Milton 1981 [29]), and the zeta function method, have confirmed his original calculation. Since then various other geometries like infinitely long circular cylinder [29], cylinders of triangular [30] and rectangular shapes, rectangular boxes [31, 32], wedges [33, 34, 35], and objects of arbitrary shapes have been considered and obtained with various approaches like, mode summation method, zeta function method [36], heat and cylinder kernel method [37], multiple scattering formalism [28, 22, 38], and world-line technique [39], to better understand the sign and magnitude of the Casimir energy [40, 17]. A review is given in the book by Bordag et al. [16].

1.4 Experimental advances in measuring Casimir effects

The theoretical descriptions of the Casimir effect for real macroscopic materials presented in this chapter imply that the measurement of the Casimir force is a complicated scientific and technological problem. The strong dependence on separation, as well as geometrical and material properties of the objects makes a comparison between experiment and theory challenging. The first attempt to measure the Casimir force was by Sparnaay in 1958 [41]. He used the original configuration of two flat metal plates balanced by springs. The measurement was consistent with the existence of a long range attractive force, but its error was over 100% and no quantitative determination was feasible. One of the major difficulties in these early experiments is the problem of how to make two surfaces parallel at small distances. To circumvent this problem, Derjaguin proposed and Lamoreaux, in 1997 [6], used configuration in which the Casimir force between a gold plated and a gold coated sphere is measured using a torsion pendulum. These measurements agreed with the Lifshitz theory to an accuracy of about 5%. In following years, new measurement technology was employed by Mohideen et al [42, 43, 44] on the plate-sphere configuration using increased-sensitivity atomic force microscopy (AFM). They claimed accuracy of within 5% with theories. This new method demonstrated, for the first time, the influence of the nonzero skin depth and surface roughness on the Casimir force. Another way to tackle the parallelity is using micromechanical torsional oscillators conducted by Decca et al [45, 46, 47, 48, 49]. These experiments allowed a definitive choice between different theoretical approaches to the thermal Casimir force with real metal surfaces.

Since then, the surface roughness effect has been carefully investigated by a series of measurements, using AFM, [50, 51, 4] performed by Palasantzas's group. It was found that a sharp increase in the force was attributed to particularly high islands of the surface profile that can be seen in some of the AFM scans of the gold surfaces. The pronounced effect of such islands is beyond the scope of a perturbative analysis and was explained by a semi-empirical approach [52] based on the proximity force approximation (PFA). However, in their paper [4], gold films with 100nm and 200nm thickness of relatively low roughness appear to be almost free of such buildup effects. The forces in these cases, contrary to previous calculation, are smaller than the PFA predictions at small separations. Providing a conceptual explanation and quantitative prediction in the framework of low energy effective theory to these unexpected results would be the main work of this thesis.

Chapter 2

Theoretical foundations

2.1 Multiple scattering approach to the Casimir energy

Let us begin by considering a massless scalar field, ϕ, interacting with a, time-independent, and positive local potential $V(\mathbf{x})$ described by the Lagrangian density,

$$L(\phi(x)) = \frac{1}{2}\partial_\mu\phi(x)\partial^\mu\phi(x) - \frac{1}{2}V(\mathbf{x})\phi(x)^2. \tag{2.1}$$

Here and in the following we use a Minkowski metric with signature (1,-1,-1,-1) and natural units h=c=1. The corresponding action when the scalar field is linearly coupled to an external source $P_\omega(\mathbf{x})$ is

$$S = \int d\mathbf{x} \int \frac{d\omega}{2\pi}\Big[\frac{1}{2}\phi^*_\omega(\Delta + \omega^2 - V(\mathbf{x}) + i\varepsilon)\phi_\omega + P_\omega(\mathbf{x})\phi_\omega\Big]. \tag{2.2}$$

Where ϕ_ω is the Fourier transform in frequency space of ϕ. Eq.(2.2) defines the dynamics of this system. The quantum field theory corresponding to the action of Eq.(2.2), is given by the generating functional for the correlations of ϕ_ω as,

$$Z[P] = \int D[\phi_\omega]e^{iS(\phi_\omega,P_\omega)}. \tag{2.3}$$

The imaginary, $i\varepsilon$, "mass" term in Eq.(2.2) dampens the contribution from large values of ϕ_ω and makes the functional integral in Eq.(2.3) well defined. Since the action of this model is quadratic in ϕ_ω, this quantum field theory is completely determined by the two-point Green's function $G(\mathbf{x},\mathbf{x}';\omega)$ that is the solution of the PDE,

$$-\Big[\Delta + \omega^2 - V(\mathbf{x}) + i\varepsilon\Big]G(\mathbf{x},\mathbf{x}';\omega) \;=\; \delta^{(3)}(\mathbf{x}-\mathbf{x}') \tag{2.4}$$

To obtain an explicit expression for Eq.(2.3), we introduce the shifted field, ϕ'_ω,

$$\phi'_\omega = \phi_\omega + \int d\mathbf{x}' G(\mathbf{x},\mathbf{x}';\omega) P_\omega(\mathbf{x}'). \tag{2.5}$$

In terms of this field, the functional integral of Eq.(2.3) factorizes,

$$\begin{aligned} Z[P] = exp\Big[-\frac{1}{2}\int d\mathbf{x}d\mathbf{x}'\int\frac{d\omega}{2\pi}P_\omega(\mathbf{x})G(\mathbf{x},\mathbf{x}';\omega)P_\omega(\mathbf{x}')\Big] \times \\ \int D[\phi'_\omega]exp\Big[i\frac{1}{2}\int d\mathbf{x}\int\frac{d\omega}{2\pi}\Big[\phi'^*_\omega(\Delta+\omega^2-V(\mathbf{x})+i\varepsilon)\phi'_\omega\Big]\Big] \end{aligned} \tag{2.6}$$

into a constant $Z[0]$, that does not depend on the source P, and a Gaussian dependence on the source,

$$Z[P] = Z[0]exp\Big[-\frac{1}{2}\int d\mathbf{x}d\mathbf{x}'\int\frac{d\omega}{2\pi}P_\omega(\mathbf{x})G(\mathbf{x},\mathbf{x}';\omega)P_\omega(\mathbf{x}')\Big]. \tag{2.7}$$

The poles of the propagator G for complex ω are in the second and fourth quadrant due to the $i\varepsilon$ and the fact that the potential is real. The frequency integral along the real axis of the complex plane can thus be deformed to an integral along the imaginary frequency axis with the substitution $\omega \rightarrow i\zeta$,.

The functional integral for Z[0] similarly can be continued to the determinant of an elliptic operator [1]

$$\begin{aligned} Z[0] &= \int D[\phi'_\omega]exp\Big[\frac{i}{2}\int d\mathbf{x}\int\frac{d\omega}{2\pi}\phi'^*_\omega(\Delta+\omega^2-V(\mathbf{x})+i\varepsilon)\phi'_\omega\Big] \\ &\sim \Big[det(\Delta+\omega^2-V(\mathbf{x})+i\varepsilon)\Big]^{-\frac{1}{2}} \\ &\sim \Big[det(1+V(\mathbf{x})G_0)\Big]^{-\frac{1}{2}}. \end{aligned} \tag{2.8}$$

Where the proportionality constant does not depend on the potential $V(\mathbf{x})$ and the Green's function $G_0(\mathbf{x},\mathbf{x}';\omega)$ satisfies the differential equation,

$$-\Big[\Delta+\omega^2+i\varepsilon\Big]G_0(\mathbf{x},\mathbf{x}';\omega) = \delta^{(3)}(\mathbf{x}-\mathbf{x}') \tag{2.9}$$

[1] This continuation is slightly more complicated: because one also has to continue the integration variables, one has to consider a finite time interval for which the frequency spectrum is discrete.

The change in the zero-point energy due to the potential $V(\mathbf{x})$ is the Casimir energy formally given by,

$$\begin{aligned} E_c &= F_V - F_{V=0} \\ &= \frac{1}{2}\int \frac{d\zeta}{2\pi} Trln\Big[1 + V(\mathbf{x})G_0\Big] \\ &= -\frac{1}{2}\int \frac{d\zeta}{2\pi} TrlnGG_0^{-1}. \end{aligned} \tag{2.10}$$

The last expression is due to the identity,

$$G = \Big(1 + V(\mathbf{x})G_0\Big)^{-1} G_0. \tag{2.11}$$

Eq.(2.10) serves as the central formula for calculating the Casimir energy. To expose the multi-scattering content of Eq.(2.10), we follow standard scattering theory [53] as reviewed by Kenneth and Klich in [54], and define the single-body scattering T-matrix as,

$$\begin{aligned} T &= \bar{S} - 1 \\ &= V - VG_0V + VG_0VG_0V - ... \\ &= \frac{V}{1 + G_0V}. \end{aligned} \tag{2.12}$$

Comparing Eq.(2.12) and Eq.(2.11), the Casmir free energy Eq.(2.10) may also be written in terms of scttering matrix T,

$$\begin{aligned} E_c &= -\frac{1}{2}\int \frac{d\zeta}{2\pi} Trln\frac{1}{1 + G_0V} \\ &= -\frac{1}{2}\int \frac{d\zeta}{2\pi} TrlnV^{-1}T. \end{aligned} \tag{2.13}$$

The formula above formally gives the Casimir free energy for a single body in vaccum. For two disjoint objects, we separate the potential V into two parts,

$$V = V_1 + V_2, \tag{2.14}$$

Eq.(2.12) in this case can be rewritten in the form,

$$\begin{aligned} T &= \frac{(V_1+V_2)}{1+G_0(V_1+V_2)} \\ &= (V_1+V_2)\frac{1}{1+G_0V_1}\frac{(1+G_0V_1)(1+G_0V_2)}{1+G_0(V_1+V_2)}\frac{1}{1+G_0V_2} \\ &= (V_1+V_2)(1-G_0T_1)(1-G_0T_1G_0T_2)^{-1}(1-G_0T_2) \end{aligned} \tag{2.15}$$

where the scattering matrices for the individual objects are given by,

$$T_i = V_i(1+G_0V_i)^{-1}, \qquad i = 1,2. \tag{2.16}$$

Combining Eq.(2.15) with Eq.(2.13), the total Casimir energy of the two-body system is,

$$\begin{aligned} E_c &= -\frac{1}{2}\int\frac{d\zeta}{2\pi}Trln\Big[(V_1+V_2)^{-1}T\Big] \\ &= -\frac{1}{2}\int\frac{d\zeta}{2\pi}Trln\Big[(1-G_0T_1)(1-G_0T_1G_0T_2)^{-1}(1-G_0T_2)\Big] \\ &= -\frac{1}{2}\int\frac{d\zeta}{2\pi}Tr\Big[lnV_1^{-1}T_1 - ln(1-G_0T_1G_0T_2) + lnV_2^{-1}T_2\Big] \\ &= E_{c1}+E_{c12}+E_{c2}, \end{aligned} \tag{2.17}$$

where E_{c1} and E_{c2} are the one-body Casimir energies and E_{c12} is the two-body interaction energy between them, given by

$$\begin{aligned} E_{c12} &= \frac{1}{2}\int\frac{d\zeta}{2\pi}Trln\Big[1-G_0T_1G_0T_2\Big] \\ &= \frac{1}{2}\int\frac{d\zeta}{2\pi}Trln\Big[1-V_1G_1V_2G_2\Big], \end{aligned} \tag{2.18}$$

where the Green's functions in the presence of a single individual object are,

$$G_i = (1+G_0V_i)^{-1}G_0, \qquad i = 1,2. \tag{2.19}$$

The first expression in Eq.(2.18) was given by Emig et al in [55], and by Kenneth and Klich in [54]. The latter is appropriate if the individual Green's functions are known. One should emphasize that only the free propagator, G_0, contains all the information on the separation and relative positioning of the two objects. All relevant characteristics (material and geometric) of each dielectric object are represented by its scattering T_i matrix. Note that since high momentum contributions are exponentially suppressed in G_0, the Volterra series of E_{c12} in powers of G_0T_i,

$$\begin{aligned} E_{c12} &= \frac{1}{2}\int \frac{d\zeta}{2\pi} Trln\Big[1 - G_0T_1G_0T_2\Big] \\ &= \frac{1}{2}\int \frac{d\zeta}{2\pi} Tr\Big[1 - G_0T_1G_0T_2 + \frac{1}{2}G_0T_1G_0T_2G_0T_1G_0T_2 - ... \end{aligned} \tag{2.20}$$

converges when the individual scattering matrices are well defined.

2.2 Temperature

The multiple scattering formalism discussed in the last section is appropriate at zero temperature. In reality this is rarely the case and effects from thermal fluctuations of real photons often have to be included in practice.

A few years after Casimir's [5] seminal paper, Lifshitz [23], in his generalization, included the effect of finite temperature. This, however, led to some controversies in subsequent years. Schwinger and associates [25] showed that the finite temperature correction depends on how the material properties are extrapolated to zero frequency. The conventional approach to finite temperature effect is to sum over Matsubara frequenciesinstead of integrating along the imaginary frequency axis,

$$\zeta \to \zeta_n = 2\pi n/\beta, \qquad \beta = \frac{1}{kT} \tag{2.21}$$

$$\int_0^\infty \frac{d\zeta}{2\pi} \to \frac{1}{\beta}\sum_{n=0}^{\infty}{}' \tag{2.22}$$

the prime being the instruction to count the $n = 0$ term in the sum with half weight. For two parallel perfectly conducting slabs separated by a a distance a in vacuum, this leads to the following formula for the Casimir pressure in the limit of an ideal metal with dielectric permittivity $\varepsilon \to \infty$,

$$P_T = -\frac{1}{4\pi\beta a^3}\sum_{n=0}^{\infty}{}' \int_{nt}^{\infty} y^2 dy \frac{1}{e^y - 1}, \qquad t = \frac{4\pi a}{\beta} \tag{2.23}$$

It is straightforward to obtain the high and low temperature limits for the pressure from Eq.(2.23),

$$\begin{aligned} P_T &\sim -\frac{1}{4\pi\beta a^3}\zeta(3) - \frac{1}{2\pi\beta a^3}\left(1 + t + \frac{t^2}{2}\right)e^{-t}, \qquad \beta << 4\pi a \\ P_T &\sim -\frac{\pi^2}{240 a^4}\left[1 + \frac{16}{3}\frac{a^4}{\beta^4} - \frac{240}{\pi}\frac{a}{\beta}e^{-\pi\beta/a}\right], \qquad \beta >> 4\pi a \end{aligned} \tag{2.24}$$

However the procedure is controversial [56] because taking the $\varepsilon \to \infty$ limit before or after letting the $\zeta \to 0$ leads to different contributions from the TE zero mode. The difference in the order of the limits leads to different results in both the (low and high) temperature regimes for the Casimir pressure of an ideal metal. According to Milton [57], one should consider the finite temperature limit of an imperfect metal. The low temperature Casimir pressure of an ideal in this scheme is given by,

$$P_T \sim -\frac{\pi^2}{240 a^4}\left[1 + \frac{16}{3}(aT)^4\right] + \frac{\zeta(3)}{8\pi a^3}T, \qquad \beta >> 4\pi a \tag{2.25}$$

The term linear in T is absent in the previous result, Eq.(2.24), obtained by Lifshitz and other authors [57]. At distances between the plates of the order of $1\mu m$, the linear dependence in T dominates other terms at room temperature (300K) $aT \sim 0.1$. At high temperatures, the Casimir effect in this limit is reduced by a factor 1/2 compared to Eq.(2.24) and is given by,

$$P_T \sim -\frac{\zeta(3)}{8\pi a^3}T, \qquad \beta << 4\pi a \tag{2.26}$$

The linear dependence on temperature at high temperature limit in this case agrees with the behavior expected from the classical Debye-H$\ddot{u}$ckel theory.

2.3 Statistic description of random roughness

To construct a perturbation theory for roughness corrections, a theoretical description of the surface structure has to be first given. We start by considering arbitrary surface profile, $h(\mathbf{x})$, giving the height deviation from a homogeneous planar surface at the two-dimensional transverse coordinate $\mathbf{x}$. In principle, with full knowledge of the profile function $h(\mathbf{x})$, one can exactly compute (at least numerically) the Casimir force between rough slabs with the corresponding boundary conditions. However for a random fluctuating rough plate, the function $h(\mathbf{x})$ can be extremely complex and it is impractical to describe such surfaces microscopically. In Sec. 2.4 we instead will model the generating functional of the roughness correlation functions.

On the other hand, a set of surfaces that have been produced by similar processes and treatments will have statistical similarities that will distinguish them from others. It thus should be possible [58] to characterize such a statistical ensemble of surfaces by a few macroscopic parameters (like size and relative distances between grains). We therefore first present this statistical description of random surface profiles. Note that contrary to the description by the correlators in Sec. 2.4, this statistical description by ensembles is not very useful for deterministically produced (i.e. machined) profiles.

2.3.1 Height Probability Distributions

In general, a random rough surface is statistically described by n-point height probability distribution function $P_n(\mathbf{x}_1, h_1; ...; \mathbf{x}_n, h_n)$ where,

$$P_n(\mathbf{x}_1, h_1; ...; \mathbf{x}_n, h_n) dh_1 ... dh_n \tag{2.27}$$

is the probability of finding surface points at transverse coordinates $(\mathbf{x}_1, ...\mathbf{x}_n)$ with heights between $(h_1, h_2, ..., h_n)$ and $(h_1 + dh_1, h_2 + dh_2, ..., h_n + dh_n)$. This statistical modal to describes an ensemble of *static surfaces* by their average profile characteristics such as rms heights and correlation lengths. In most cases one only requires P_1 and P_2 to obtain acceptable predictions.

From the probability functions, one can calculate the ensemble averages of any functional of the random variables $(h_1, h_2..., h_n)$ through the integral,

$$\langle H\rangle(\mathbf{x}_1, ..., \mathbf{x}_n) = \int H(h_1, ...h_n)P_n(\mathbf{x}_1, h_1; ...; \mathbf{x}_n, h_n)dh_1...dh_n. \tag{2.28}$$

For example, the mean height as a function of transverse position is expressed by,

$$\langle h\rangle(\mathbf{x}) = \int hP_1(\mathbf{x}, h)dh. \tag{2.29}$$

and the height-height two-points correlation function C_2 is,

$$C_2(\mathbf{x}_1, \mathbf{x}_2) = \langle h_1h_2\rangle = \int h_1h_2P_2(\mathbf{x}_1, h_1; \mathbf{x}_2, h_2)dh_1dh_2 \tag{2.30}$$

If the rough surface is homogeneous and the correlation functions, C_n, depend only on distances, $|\mathbf{x}_j - \mathbf{x}_1|$, between the space points on the surface.

$$\langle C_n\rangle(\mathbf{x}_1, ..., \mathbf{x}_n) = \langle C_n\rangle(0, |\mathbf{x}_2 - \mathbf{x}_1|, ..., |\mathbf{x}_n - \mathbf{x}_1|) \tag{2.31}$$

In these cases, the mean height does not depend on the position and one can find a reference plane such that $\langle h\rangle = 0$. Common assumptions for such surfaces are, (i) the surface heights have a Gaussian distribution,

$$P_1(h) = \frac{1}{\sigma\sqrt{2\pi}}exp\Big(-\frac{h^2}{2\sigma^2}\Big) \tag{2.32}$$

(ii) The root mean square height (variance) is

$$\langle h^2\rangle = \int h^2P_1(0, h)dh = \sigma^2 \tag{2.33}$$

The rms height is widely used (combined with correlation length) to characterize the"degree of roughness" - the larger the σ, the rougher the surface.

Similarly, the height-height correlation function can be written as,

$$\begin{aligned} C_2(\mathbf{x}_1, \mathbf{x}_2) &= \langle h_1(0) h_2(|\mathbf{x}_2 - \mathbf{x}_1|)\rangle \\ &= \int h_1 h_2 P_2(0, h_1; |\mathbf{x}_2 - \mathbf{x}_1|, h_2) dh_1 dh_2 \end{aligned} \tag{2.34}$$

It is useful to consider the random varying surface as a superposition of gratings of different periods and amplitudes. One introduces the Fourier expansion [59] of the correlation function, C_n,

$$\bar{C_n} = \int dr_2 dr_3 ....dr_n e^{i(\mathbf{q}_2\cdot\mathbf{r}_2 + \mathbf{q}_3\cdot\mathbf{r}_3 + ...\mathbf{q}_n\cdot\mathbf{r}_n)} C_n \tag{2.35}$$

where $\mathbf{r}_n = \vec{x}_n - \vec{x}_1$ and $\mathbf{q}$ is the in-plane wave-vector. If the spectrum fuction, $\bar{C_n}$, decreases slowly with increasing $\mathbf{q}$, short period components of the roughness remain sizable. In the limit of small correlation length, there is little relation between the heights of any two points and the surface is very irregular. On the other hand, if the spectral correlation function vanishes rapidly for large $\mathbf{q}$, the profile varies slowly and the surface is rather smooth.

We so far considered ensemble averages, which require a set of rough surfaces generated by a similar homogeneous random process. However, if only a single surface is avalible, the spatial averages of the particular profile functional are ensemble averages,

$$H(0, \mathbf{x}_1 ....., \mathbf{x}_n) = \lim_{A\to\infty} \frac{1}{A} \int_A d\mathbf{x}' H[h(\mathbf{x}')...h(\mathbf{x}' + \mathbf{x}_n)] \tag{2.36}$$

It happens frequently that each surface of the ensemble carries the same statistical properties about the homogeneous random process as every other surface. The spatial averages for any surface are then all equal and coincide with the ensemble average. The homogeneous random process, in this case, is said to be ergodic.

2.3.2 Numerical method for generating random rough surface

As discussed in the last section, random rough surfaces are characterized by their statistical properties. The most important of these are the height distribution and height correlation functions. Experimental determination of these functions are affected by systematic problems such as sampling intervals, the distance between recording points, and surface extent [1]. A short sampling interval can significantly change the short-range behavior of the correlation function. The long-range behavior is mostly determined by the surface extent. Measurements would be more reliable if there is a numerical reference to which one can compare the data.

The technique to numerically generate roughness profiles with prescribed correlations is based on the "moving average method" [60]. Consider a rough surface characterized by a set of correlated random numbers $z_{i,j}$ that represent the height of the surface at the discrete positions $\mathbf{r} = (x_i, y_j)$. To generate these correlated heights a set of normally distributed random numbers $v_{i,j}$ with zero mean is first generated. The correlated data are obtained as a moving average of these numbers,

$$z_{i,j} = \sum_{k=-N}^{N} \sum_{l=-M}^{M} v_{i+k,j+l} w_{k,l} \tag{2.37}$$

with fixed weights $w_{k,l}$. N and M give the number of points in the row and column of the set of the simulated data. The weights are normalized,

$$\sum_{k} \sum_{l} w_{k,l} = 1 \tag{2.38}$$

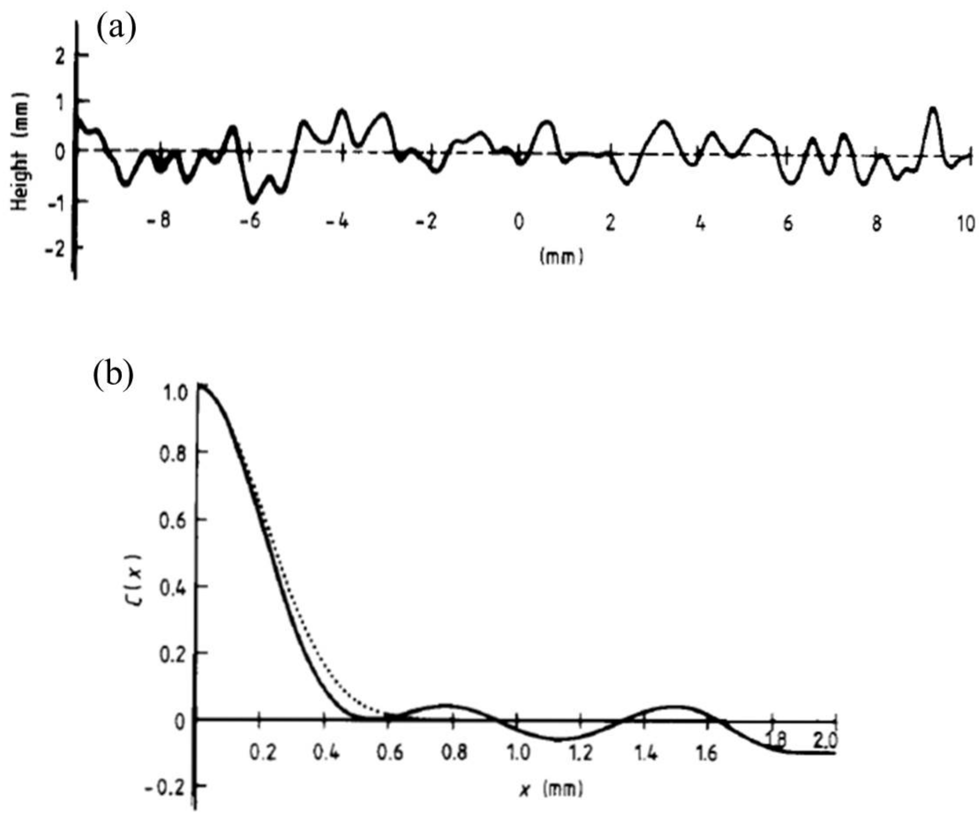

Figure 2.1: Gaussian surface and its correlation function.[1] (a) Surface profile. (b) Height correlation function: full curve, the simulated surface correlation function; dotted curve, theoretical gaussian correlation function. rms : 0.4mm, Correlation length : 0.3mm

To determined the weights, $w_{k,l}$, that correspond to the desired correlation function $\bar{C}_2$, we evaluate the Fourier spectrum,

$$\begin{aligned} \bar{C}_2 &= \sum_i \sum_j \sum_{i'} \sum_{j'} e^{i(\mathbf{q}\cdot\mathbf{r}+\mathbf{q}'\cdot\mathbf{r}')} \langle z_{i,j} z_{i',j'} \rangle \\ &= \bar{w}_{\mathbf{q}} \bar{w}_{\mathbf{q}'} \langle \bar{v}_{\mathbf{q}} \bar{v}_{\mathbf{q}'} \rangle \end{aligned} \tag{2.39}$$

where $\bar{w}_{\mathbf{q}}$ and $\bar{v}_{\mathbf{q}}$ are the Fourier transform of the weighting and distribution functions. For homogeneous and isotropic surfaces, the correlation function C_2 only dependes on the distances between two points. In those cases, Eq.(2.39) reduces to,

$$w_{k,l} = FT\Big[\frac{\sqrt{\bar{C}_2}}{\langle \bar{v}_{\mathbf{q}} \bar{v}_{-\mathbf{q}} \rangle}\Big] \tag{2.40}$$

For a Gaussian correlation function of C_2 the weighting functions are themselves Gaussian,

$$w_{k,l} = \frac{2}{\pi} exp\Big\{ -2\Big[\Big(\frac{x_k}{\lambda_x}\Big)^2 + \Big(\frac{y_l}{\lambda_y}\Big)^2\Big]\Big\} \tag{2.41}$$

An example of a 1-dimensional rough surface generated by this technique is shown in Fig. 2.1. The correlation function for the surface Fig. 2.1(a) is shown in Fig. 2.1(b) as a full curve. The corresponding gaussian correlation function it is an approximation to is the dotted line of Fig. 2b. The two curves are in reasonably good agreement, limited only by the finite number of points and the finite extent of the surface.

2.4 Field theoretic description of roughness correlations

The main purpose of this thesis is to obtain a systematic perturbative expansion of roughness corrections to Casimir energies. In the spirit of a path-integral approach to Quantum Field Theory (QFT), we here construct a generating functional for the roughness correlations. We consider the standard Casimir configuration of two semi-infinite parallel plates. A Cartesian coordinate system with z-axis normal to the plates will be used.To simplify the presentation, one of the slabs will be assumed to be perfectly flat. We will see that to leading order in the roughness profile, this simplification in fact suffices to also obtain the Casimir pressure between two rough plates if their profiles are uncorrelated. The roughness profile function $h(\mathbf{x})$ at the mean height $\langle z \rangle = 0$ gives the precise position of the rough surface as a function of the transverse coordinates $\mathbf{x} = (x, y)$.

The plates are assumed to be large enough for translational invariance to approximately hold on the surface. The n-point correlation functions of the profile

$h(\mathbf{x})$ for a large plate of area A are the averages:

$$\begin{aligned}
D_1 = \langle h(\mathbf{x}_1)\rangle \quad &:= \int_A \frac{d\mathbf{x}}{A} h(\mathbf{x}+\mathbf{x}_1) \qquad (2.42)\\
D_2(\mathbf{x}_1-\mathbf{x}_2) = \langle h(\mathbf{x}_1)h(\mathbf{x}_2)\rangle \quad &:= \int_A \frac{d\mathbf{x}}{A} h(\mathbf{x}+\mathbf{x}_1)h(\mathbf{x}+\mathbf{x}_2)\\
\vdots \quad &\quad \vdots\\
D_n(\mathbf{x}_1-\mathbf{x}_2,\ldots,\mathbf{x}_{n-1}-\mathbf{x}_n) = \langle h(\mathbf{x}_1)\ldots h(\mathbf{x}_n)\rangle \quad &:= \int_A \frac{d\mathbf{x}}{A} h(\mathbf{x}+\mathbf{x}_1)\ldots h(\mathbf{x}+\mathbf{x}_n)
\end{aligned}$$

When the plate is far moved from any other object, all these n-point single body correlation functions, at least in principle, could be measured. The mean position at $\langle z\rangle = 0$ of the rough plate is fixed by requiring that

$$D_1 = \langle h(x)\rangle = 0 \qquad (2.43)$$

We can introduce a single generating functional, $Z_h[\alpha]$, to collect all correlation functions of Eq.(2.42)

$$Z_h[\alpha] = \sum_{n=2}^{\infty} \frac{1}{n!} \iint \alpha(\mathbf{x}_1)\alpha(\mathbf{x}_2)...\alpha(\mathbf{x}_n) D_n(\mathbf{x}_1,...,\mathbf{x}_n) d\mathbf{x}_1 d\mathbf{x}_2...d\mathbf{x}_n \qquad (2.44)$$

and directly model $Z_h[\alpha]$ instead of individual correlation functions. With the restriction of Eq.(2.43), the simplest model for the correlations of a rough plate is entirely determined by the two-point correlation function D_2 of the profile. The generating functional of such a (quadratic) Gaussian model is of the form,

$$Z_h^{(2)}[\alpha] = exp\Big[\frac{1}{2}\{\alpha|D_2|\alpha\}\Big], \qquad (2.45)$$

With,

$$\{\alpha|D_2|\alpha\} := \iint \alpha(\mathbf{x}_1) D_2(\mathbf{x}_1-\mathbf{x}_2)\alpha(\mathbf{x}_2) d\mathbf{x}_1 d\mathbf{x}_2. \qquad (2.46)$$

In general, Eq.(2.45) just gives the leading term in a cumulant expansion of Z_h. Stochastic roughness is fully described by the covariance of the profile and a Gaussian model by definition is exact in this case. A Gaussian model also suffices to extract corrections to the free energy to leading order in the roughness profile.

To leading order in the variance σ^2 even the correlations of a corrugated profile $h_\omega(\mathbf{x}) = \sigma\sin(\omega x)$ can be described by such a Gaussian model.

$$D_2^\omega(\mathbf{x}-\mathbf{y}) = \sigma^2 \int \frac{dr}{\text{Ł}} \sin(\omega(x+r))\sin(\omega(y+r)) = \frac{\sigma^2}{2}\cos(\omega(x-y)) \quad (2.47)$$

But the four-point correlation in this case is only half of what the Gaussian model predicts,

$$\begin{aligned}
&D_4^\omega(\mathbf{x}_1,\mathbf{x}_2,\mathbf{x}_3,\mathbf{x}_4)\\
&= \sigma^4 \int \frac{dr}{\text{Ł}} sin(\omega(\mathbf{x}_1+r))sin(\omega(\mathbf{x}_2+r))sin(\omega(\mathbf{x}_3+r))sin(\omega(\mathbf{x}_4+r))\\
&= \frac{1}{2}(D_2^\omega(\mathbf{x}_1-\mathbf{x}_2)D_2^\omega(\mathbf{x}_3-\mathbf{x}_4) + D_2^\omega(\mathbf{x}_1-\mathbf{x}_3)D_2^\omega(\mathbf{x}_2-\mathbf{x}_4)\\
&+D_2^\omega(\mathbf{x}_1-\mathbf{x}_4)D_2^\omega(\mathbf{x}_2-\mathbf{x}_3)).
\end{aligned} \quad (2.48)$$

The mathematical basis for a field theoretic approach to roughness is that any analytic functional $F[h]$ of the profile $h(\mathbf{x})$ with translation-invariant coefficients can be evaluated using the generating functional $Z_h[\alpha]$. To see this, first consider the evaluation of a monomial in the Taylor expansion of $F[h]$ for small profiles $h(\mathbf{x})$,

$$\begin{aligned}
F[h] &= \sum_n \iint d\mathbf{x}_1 d\mathbf{x}_2 \ldots d\mathbf{x}_n F_n(\mathbf{x}_1-\mathbf{x}_2,\ldots,\mathbf{x}_{n-1}-\mathbf{x}_n)h(\mathbf{x}_1)h(\mathbf{x}_2)\ldots h(\mathbf{x}_n)\\
&= \sum_n \frac{1}{A}\int_A d\mathbf{x} \iint d\mathbf{x}_1 \ldots d\mathbf{x}_n F_n(\mathbf{x}_1-\mathbf{x}_2,\ldots,\mathbf{x}_{n-1}-\mathbf{x}_n)h(\mathbf{x}+\mathbf{x}_1)\ldots h(\mathbf{x}+\mathbf{x}_n)\\
&= \sum_n \iint d\mathbf{x}_1 \ldots d\mathbf{x}_n F_n(\mathbf{x}_1-\mathbf{x}_2,\ldots,\mathbf{x}_{n-1}-\mathbf{x}_n)D_n(\mathbf{x}_1-\mathbf{x}_2,\ldots,\mathbf{x}_{n-1}-\mathbf{x}_n)
\end{aligned} \quad (2.49)$$

The second equality in Eq.(2.49) uses the translational invariance of the coefficient functions F_n (but assumes no regularity of the profile $h(\mathbf{x})$ itself). No further assumptions are required and Eq.(2.49) holds for any profile (random or corrugated) on a sufficiently large plate. Assuming that all coefficient functions F_n in the Taylor expansion of the functional $F[h]$ are translation invariant and that the expansion converges for the particular profile, Eq.(2.49) implies that one may formally evaluate $F[h]$ by applying the functional derivative,

$$F[h] = F[\frac{\delta}{\delta\alpha}]\; Z_h[\alpha]\Big|_{\alpha=0}\;. \tag{2.50}$$

The field theoretic description of the surface correlations in Eq.(2.49) and Eq.(2.50), in principle, is not only valid for stochastic roughness but also for any deterministic profile. The perturbation theory based on Eq.(2.44) therefore allows to calculate the corrections due to arbitrary surface profiles by employing the corresponding correlation functions D_n. It remains to determine the dependence of the partition function of the fields on the profiles of on average parallel plates.

Chapter 3

Perturbative roughness corrections to the Casimir energy due to a massless scalar field

3.1 The Model

3.1.1 Effective Action

Let us consider a scalar field, ϕ, interacting with delta-function potentials describing two semitransparent parallel rough plate. The Lagrangian density for this model is:

$$L(\phi(\mathbf{x}, z)) = \frac{1}{2}\partial_\mu \phi(\mathbf{x}, z)\partial^\mu \phi(\mathbf{x}, z) - V_{int}(\mathbf{x}, z)\phi(\mathbf{x}, z)^2. \tag{3.1}$$

with,

$$V_{int}(\mathbf{x}, z) = \lambda\delta(z - h(\mathbf{x}) - a) + \bar{\lambda}\delta(z). \tag{3.2}$$

The $h(\mathbf{x}) << a/2$ is the roughness profile of the upper plate surfaces at average position $\langle z \rangle = 0$. λ and $\bar{\lambda}$ are the corresponding coupling constants describing the transparency of the plates. The limit λ or $\bar{\lambda} \to \infty$ suppresses tunneling through the infinitesimally thin plate and one recovers Dirichlet boundary conditions on the surfaces. For finite coupling, the plate is semitransparent. Although the scalar model appears far removed from reality, it is simple and sufficient for analyzing the main features we will encounter in the electrodynamic case. It, in particular, essentially describes the thin-plate limit of the electric contribution to the Casimir force [61].

The classical action of Eq.(3.1) determines the generating functional of the quantum theory and defines the generating funcional of connected Green's functions $W[j]$ in the presence of an external source $j(x_i)$,

$$Z[j] = e^{-iW[j]} = \int D[\phi] exp\Big[i \int d^4x \Big(L(\phi) + j\phi\Big)\Big] \tag{3.3}$$

Consider the functional derivative of $W[j]$ with respect to $j(x_i)$,

$$\frac{\delta}{\delta j(x_i)} W[j] = i \frac{\delta}{\delta j(x_i)} \log Z = -\frac{\int D[\phi] e^{i\int (L+j\phi)} \phi(x_i)}{\int D[\phi] e^{i\int(L+j\phi)}} = -\langle \Omega | \phi(x_i) | \Omega \rangle_j \tag{3.4}$$

the last expression in Eq.(3.4) is the vacuum expectation value of the scalar $\phi(x_i)$ field in the presence of a nonzero source $j(x_i)$. It is analogous to the thermodynamic variable conjugate to $j(x_i)$. One defines the quantity $\phi_{cl}(x_i)$ as,

$$\phi_{cl}(x_i) = \langle \Omega | \phi(x_i) | \Omega \rangle_j \tag{3.5}$$

The field, ϕ_{cl}, satisfies the classical equation of motion of the system. One performs the Legendre transform of $W[j]$ to obtain the effective action, $\Gamma[\phi_{cl}]$, of ϕ_{cl},

$$\Gamma[\phi_{cl}] = -W[j] - \int d^4y j(y_i) \phi_{cl}(y_i) \tag{3.6}$$

The stable ground states of the theory are minima of Gamma because,

$$\begin{aligned}
\frac{\delta}{\delta \phi_{cl}(x_i)} \Gamma[\phi_{cl}] \quad &= -\frac{\delta}{\delta \phi_{cl}(x_i)} W[j] - \int d^4y \frac{\delta j(y_i)}{\delta \phi_{cl}(x_i)} \phi_{cl}(y_i) - j(x_i) \\
&= -\int d^4y \frac{\delta j(y_i)}{\delta \phi_{cl}(x_i)} \frac{\delta W[j]}{\delta j(y_i)} - \int d^4y \frac{\delta j(y_i)}{\delta \phi_{cl}(x_i)} \phi_{cl}(y_i) - j(x_i) \\
&= -j(x_i)
\end{aligned} \tag{3.7}$$

In a perturbative analysis, the effective action separates into that for two flat plates and corrections due to their roughness,

$$\Gamma = \Gamma^{(0)} + \Gamma^{(h)} \tag{3.8}$$

The zeroth order vertices generated by, $\Gamma^{(0)}$, are obtained by solving the Green's function of two flat surfaces. The roughness $\Gamma^{(h)}$, will be computed perturbatively in a loop expansion of the roughness profile.

3.1.2 Perturbation in the roughness profile

When the average height of the profile is much smaller than the separation between two plates, the interaction of Eq.(3.2) in terms of Hamiltonian can be expanded as:

$$\begin{aligned} H_{int}[h,\phi] &= H^{(\varepsilon)}[h] + \sum_n \int d\mathbf{x}dz[\lambda\delta(z-h(\mathbf{x})-a) + \bar{\lambda}\delta(z)]\phi_n(\mathbf{x},z)^2 \\ &= H^{(\varepsilon)}[h] + \sum_n \int d\mathbf{x}\frac{1}{2}[\lambda\phi_n^2(\mathbf{x},a+h(\mathbf{x})) + \bar{\lambda}\phi_n^2(\mathbf{x},0)] \\ &\sim H^{(\varepsilon)}[h] + \sum_n H^{(0)}_{int}[\phi_n] + H^{(1)}_{int}[h,\phi_n] + H^{(2)}_{int}[h,\phi_n] + ... \end{aligned} \tag{3.9}$$

with,

$$H^{(0)}_{int}[\phi] = \int d\mathbf{x}\Big[\frac{\lambda}{2}\phi_n^2(\mathbf{x},a) + \frac{\bar{\lambda}}{2}\phi_n^2(\mathbf{x},0)\Big], \tag{3.10a}$$

$$H^{(m)}_{int}[h,\phi] = \frac{\lambda}{2}\int d\mathbf{x}\frac{h^m(\mathbf{x})}{m!}\frac{\partial^m}{\partial a^m}\phi_n^2(\mathbf{x},a) \quad \text{for} \quad m>0, \tag{3.10b}$$

$$H^{(\varepsilon)}[h] = \int d\mathbf{x}h(\mathbf{x})c_1^{(\varepsilon)}(a;\lambda,\bar{\lambda},T) + \frac{1}{2}\iint d\mathbf{x}d\mathbf{y}h(\mathbf{x})c_2^{(\varepsilon)}(\mathbf{x}-\mathbf{y};\lambda)h(\mathbf{y}) + ... \tag{3.10c}$$

$H^{(0)}_{int}$ gives the interaction of the scalar field with two flat plates. $H^{(m)}_{int}$ is the mth order corrections to the potential in the profile. The additional terms $H^{(\varepsilon)}$ in the expression Eq.(3.9) and Eq.(3.10c) are counterterms to all orders in the profile $h(\mathbf{x})$. They are local and do not depend on the dynamical field ϕ. Only the one-point counterterm, $c_1^{(\varepsilon)}(a;\lambda,\bar{\lambda},T)$, depends on the plate separation a, temperature T and both couplings λ, $\bar{\lambda}$. This finite counterterm enforces the constraint $\langle h\rangle = 0$ at any temperature and separation when the interaction with the scalar field ϕ is turned on. It ensures that the parameter a represents the mean separation of the plates even when $\lambda,$ and $\bar{\lambda}$ do not vanish. The two-point counterterm, $c_2^{(\varepsilon)}(\mathbf{x}-\mathbf{y};\lambda)$, guarantees that the measured correlation $\langle h(\mathbf{x})h(\mathbf{y})\rangle$ at temperature $T=0$ is given by $D_2(\mathbf{x}-\mathbf{y})$ when the two plates are far apart and $\lambda > 0$. $c_2^{(\varepsilon)}(\mathbf{x}-\mathbf{y};\lambda)$ by construction does not depend on the separation a, temperature T, or the coupling strength $\bar{\lambda}$ of the distant plate. It removes all the a independent Casimir free energy contribution to the force. The $(n > 1)$-point counterterms ensure that the corresponding n-points correlation of the profile also remains unchanged at $T = 0$ when the plates are far apart and the interaction with the scalar is switched on. The model requires an infinite number of counterterms and is not renormalizable.

The generating functional for a free massless scalar field in equilibrium at temperature T can be written in Matsubara's formalism [62] as,

$$\begin{aligned} Z_0[j;T] &= \int D[\phi_n] exp\Big[-\frac{1}{2}\partial_\mu\phi_n\partial^\mu\phi_n + j_n\phi_n\Big] \\ &= exp\Big[-\frac{1}{T}\mathcal{F}^{(0)} + \frac{T}{2}\sum_n (j_n|G_n^0|j_n)\Big], \end{aligned} \tag{3.11}$$

where $\mathcal{F}^{(0)} = -\frac{\pi^2 T^4 V}{90}$ is the Helmholtz free energy of a massless scalar field in a three-dimensional Euclidean space of volume V and,

$$(j_n|G_n^0|j_n) := \int d^3x \int d^3y j_n(\vec{x}) G_n^0(\vec{x}-\vec{y}) j_n(\vec{y}). \tag{3.12}$$

The free thermal Greens-function,

$$G_n^0(\vec{x}-\vec{y}) = \frac{e^{-2\pi nT|\vec{x}-\vec{y}|}}{4\pi|\vec{x}-\vec{y}|}, \tag{3.13}$$

satisfies the differential equation,

$$(\zeta_n^2 - \nabla^2) G_n^0(\vec{x}-\vec{y}) = \delta(\vec{x}-\vec{y}) \qquad \text{with} \quad \zeta_n = 2\pi nT. \tag{3.14}$$

The generating function of thermal Green's functions at temperature T of the interacting model is:

$$\begin{aligned} Z[j,h;T,a] &= exp\Big[-\frac{1}{T}H_{int}[h,\frac{\delta}{\delta j}]\Big] Z^{||}[j;T,a] \qquad (3.15) \\ &= exp\Big\{-\frac{1}{T}\Big[H^{(\varepsilon)}[h] + \sum_{m=1}\sum_n H_{int}^{(m)}\Big[h,\frac{\delta}{\delta j_n}\Big]\Big]\Big\} Z^{||}[j;T,a] \end{aligned}$$

$Z^{||}[j;T,a]$ contains all the information of the two flat parallel plates. It generates the thermal Green's functions of the scalar field to all orders in the presence of the two plates separated by a distance a,

$$\begin{aligned} Z^{||}[j;T,a] &= exp\Big[-\frac{1}{T}\sum_n H^{(0)}_{int}\Big[\frac{\delta}{\delta j_n}\Big]\Big]Z_0[j;T] \\ &= exp\Big[-\frac{1}{T}\sum_n \int d\mathbf{x}\Big[\lambda\frac{\delta^2}{\delta j_n(\mathbf{x},a)^2}+\bar{\lambda}\frac{\delta^2}{\delta j_n(\mathbf{x},a)^2}\Big]\Big]Z_0[j;T] \\ &= exp\Big[-\frac{1}{T}\mathcal{F}^{||}(T;a,\lambda,\bar{\lambda})+\frac{T}{2}\sum_n (j_n|G^{||}_n|j_n)\Big]. \end{aligned} \tag{3.16}$$

Here $\mathcal{F}^{||}$ is the free energy of a massless scalar field in the presence of two semitransparent parallel plates. The detailed derivation of $\mathcal{F}^{||}$ is given in A.1. $H_{int}[h,\frac{\delta}{\delta j}]$ in Eq.(3.15) includes all the interaction with the roughness profile. Since all the Greens functions for two flat plates are translationally invariant, the dependence on the roughness profile in the field theoretic description may be obtained by replacing $h(\mathbf{x})$ by the derivative operator $h \rightarrow \frac{\delta}{\delta\alpha}$ acting on the roughness generating functional $Z_h[\alpha]$. From the QFT point of view this promotes the roughness profile to a field on a two-dimensional surface all of whose correlators are known. Note that this field is not dynamical in the sense that only the n=0 Matsubara frequency contributes. With a Gaussian generating functional of roughness correlations, the generating functional of the two interacting scalar fields, ϕ and h, is of the form,

$$\begin{aligned} Z^{(\varepsilon)}[j,\alpha;T,a] &= exp\Big[-\frac{1}{T}H^{(\varepsilon)}\Big[\frac{\delta}{\delta\alpha}\Big]-\frac{1}{T}\sum_{m=1}\sum_n H^{(m)}_{int}\Big[\frac{\delta}{\delta\alpha},\frac{\delta}{\delta j}\Big]\Big] \\ &\times\ exp\Big[\frac{1}{2}\{\alpha|D_2|\alpha\}+\frac{T}{2}\sum_n (j_n|G^{||}_n|j_n)\Big]. \end{aligned} \tag{3.17}$$

The thermal Green's function, $G^{||}_n$, of a scalar thermal mode in the presence of two flat parallel plates satisfies the partial differential equation,

$$(\zeta_n^2-\nabla^2+\lambda\delta(z-a)+\bar{\lambda}\delta(z))G^{||}_n(\mathbf{x}-\mathbf{y},z,z')=\delta(z-z')\delta(\mathbf{x}-\mathbf{y})$$
$$\text{with} \quad \zeta_n = 2\pi nT. \tag{3.18}$$

For a flat surface with transverse translational symmetry, the solution, $G_n^{||}$, can be expressed by the reduced Green's function $g^{||}$ as,

$$\begin{aligned}\langle\phi_n(\mathbf{x},z)\phi_n(\mathbf{y},z')\rangle^{||} &= G_n^{||}(\mathbf{x}-\mathbf{y},z,z') \\ &= \int \frac{d\mathbf{k}}{(2\pi)^2} e^{i\mathbf{k}(\mathbf{x}-\mathbf{y})} g^{||}(z,z';\kappa_n),\end{aligned} \tag{3.19}$$

with $\kappa_n^2 = \zeta_n^2 + \mathbf{k}^2 = (2\pi nT)^2 + \mathbf{k}^2$. Inserting Eq.(3.19) to Eq.(3.18) gives the ordinary second-order differential equation satisfied by $g^{||}(z,z';\kappa)$,

$$\left[\kappa^2 - \frac{d^2}{dz^2} + \lambda\delta(z-a) + \bar{\lambda}\delta(z)\right] g^{||}(z,z';\kappa) = \delta(z-z'). \tag{3.20}$$

The solution to the differential equation above is well known [20] and listed below A.2,

$$g^{||}(z,z';\kappa) = \frac{e^{-\kappa|z-z'|}}{2\kappa} - \frac{\Delta^{-1}}{2\kappa}[e^{-\kappa|z-a|}, e^{-\kappa|z|}] \cdot A \tag{3.21}$$

$$\begin{aligned}\text{with} \qquad A &= \begin{bmatrix} t & -te^{-\kappa a}\bar{t} \\ -te^{-\kappa a}\bar{t} & \bar{t} \end{bmatrix} \cdot \begin{bmatrix} e^{-\kappa|z'-a|} \\ e^{-\kappa|z'|} \end{bmatrix} \\ \Delta &= 1 - t\bar{t}e^{-2\kappa a}\ , \quad t = \frac{\lambda}{2\kappa+\lambda} \ \text{ and } \ \bar{t} = \frac{\bar{\lambda}}{2\kappa+\bar{\lambda}}.\end{aligned}$$

3.2 Feynman Rules

We now derive the perturbative expansion with associated Feynman rules for the scattering matrix based on Eq.(3.17). Since the δ-function potentials Eq.(3.2) constraint the interaction on the rough surface, it will be advantageous to derive the Feynman rules in transverse momentum space.

3.2.1 Propagators

The model on the plane has four propagators. In transverse momentum space they are given by Eqs. (A.15a),(A.15b), (A.15c) of Appendix A and by the Fourier transform $d(\mathbf{k})$ of D_2. On the two-dimensional plane, $\phi_n(\mathbf{x}, a)$ and $\frac{\partial}{\partial a}\phi_n(\mathbf{x}, a)$ are independent and distinct modes. Introducing their Fourier components,

$$\psi_n(\mathbf{k}) := \int d\mathbf{x} e^{i\mathbf{k}\mathbf{x}} \phi_n(\mathbf{x}, a) \quad \text{and} \quad \tilde{\psi}_n(\mathbf{k}) := \int d\mathbf{x} e^{i\mathbf{k}\mathbf{x}} \phi'_n(\mathbf{x}, a) \ , \tag{3.22}$$

the four nonvanishing propagators of the surface model in (two-dimensional) Fourier space are

$$\langle\psi_n(\mathbf{k})\psi_n(-\mathbf{k})\rangle^{\parallel} = g_{00}^{(f)}(\kappa_n) + g_{00}^{(s)}(\kappa_n) = \frac{1}{\lambda + 2\kappa_n} - \frac{2\kappa_n t_n^2 \bar{t}_n e^{-2\kappa_n a}}{\lambda^2 \Delta_n}, \tag{3.23a}$$

$$\langle\psi_n(\mathbf{k})\tilde{\psi}_n(-\mathbf{k})\rangle^{\parallel} = g_{01}^{(s)}(\kappa_n) = g_{10}^{(s)}(\kappa_n) = 0 + \frac{\kappa_n t_n \bar{t}_n e^{-2\kappa_n a}}{\lambda \Delta_n}, \tag{3.23b}$$

$$\langle\tilde{\psi}_n(\mathbf{k})\tilde{\psi}_n(-\mathbf{k})\rangle^{\parallel} = g_{11}^{(f)}(\kappa_n) + g_{11}^{(s)}(\kappa_n) = -\frac{\kappa_n}{2} - \frac{\kappa_n \bar{t}_n e^{-2\kappa_n a}}{2\Delta_n}, \tag{3.23c}$$

$$\langle h(\mathbf{k})h(-\mathbf{k})\rangle = d^{(f)}(\kappa_0) = \int d\mathbf{x} D_2(\mathbf{x}) e^{i\mathbf{k}\mathbf{x}} = 2\pi\sigma^2\ell^2 e^{-\ell^2\mathbf{k}^2/2} \ , \tag{3.23d}$$

with

$$\Delta_n := 1 - t_n \bar{t}_n e^{-2\kappa_n a} \ , \qquad t_n := \frac{\lambda}{\lambda + 2\kappa_n}$$
$$\bar{t}_n := \frac{\bar{\lambda}}{\bar{\lambda} + 2\kappa_n} \ , \qquad \kappa_n := \sqrt{(2\pi n T)^2 + \mathbf{k}^2} \ . \tag{3.24}$$

In Eq.(3.23) we have decomposed the propagators into separation dependent, (s)oft parts that are exponentially suppressed for $a\kappa >> 1$ and (f)ast parts that remain in the limit $a \to \infty$. Note that g_{00} and g_{01} vanish in the strong coupling (Dirichlet) limit $\lambda \to \infty$, whereas correlations of the normal derivative on the surface described by g_{11} do not. There are no transitions between thermal modes in this model and the quantities t_n, $\bar{t}_n$ and Δ_n defined in Eq.(3.24) are diagonal and functions of κ_n only. For simplicity, the two-point correlation function for the profile is assumed to be a Gaussian Eq.(3.23d). It is characterized by the variance σ^2 and correlation length, ℓ of the profile only. To describe realistic gold films, more sophisticated correlation functions [63] would be required for electromagnetic roughness corrections. It in fact appears impossible to reproduce experimental observations of the Casimir force with a single roughness scale [64]. Relatively rare, but high peaks of the roughness profile appear to dominate the correction at separations close to contact [65]. Although the results here only employ a simple Gaussian form, other correlation functions that vanish faster than any power of the transverse momentum are equally admissible and do not change our considerations and conclusions qualitatively.

The separation between two plates sets the low energy scale in this model. At large distances, the roughness correction is insensitive to local differences of the roughness profiles. For small separations $a \lesssim \ell$ the absolute magnitude of the correction does depends sensitively on the form of the correlation function in Eq.(3.23d). A quantitative comparison with experiments currently is possible only in the electromagnetic case, which is not considered here but will be discussed in the next chapter.

We collect the $\psi, \tilde{\psi}$ propagators of Eq.(3.23) in the matrix,

$$\mathbf{g}(\kappa) = \begin{pmatrix} g_{00}(\kappa) & g_{01}(\kappa) \\ g_{10}(\kappa) & g_{11}(\kappa) \end{pmatrix} , \tag{3.25}$$

whose negative inverse $\mathbf{\Gamma}^{(0)}$ is the matrix of two-point vertices for vanishing profile

$h = 0$,

$$\mathbf{\Gamma}^{(0)}(\kappa) := -\mathbf{g}^{-1}(\kappa) = -\frac{1}{det[\mathbf{g}(\kappa)]}\begin{pmatrix} g_{11}(\kappa) & -g_{01}(\kappa) \\ -g_{10}(\kappa) & g_{00}(\kappa) \end{pmatrix} \tag{3.26}$$

$$= -\begin{pmatrix} \lambda + 2\kappa(1+\bar{t}e^{-2\kappa a}) & 2\bar{t}e^{-2\kappa a} \\ 2\bar{t}e^{-2\kappa a} & -\frac{2}{\kappa}(1-\bar{t}e^{-2\kappa a}) \end{pmatrix}$$

$$= 2\begin{pmatrix} -\kappa & 0 \\ 0 & \kappa^{-1} \end{pmatrix} - \begin{pmatrix} \lambda & 0 \\ 0 & 0 \end{pmatrix} - 2\bar{t}e^{-2\kappa a}\begin{pmatrix} \kappa & 1 \\ 1 & \kappa^{-1} \end{pmatrix} .$$

The corresponding generating functional of tree-level two-point vertices is,

$$\Gamma^{(0)}[\psi, \tilde{\psi}] = \frac{1}{2}\sum_n \int \frac{d\mathbf{k}}{(2\pi)^2}(\psi_n(\mathbf{k}), \tilde{\psi}_n(\mathbf{k})) \cdot \mathbf{\Gamma}^{(0)}(\kappa_n) \cdot \begin{pmatrix} \psi_n(-\mathbf{k}) \\ \tilde{\psi}_n(-\mathbf{k}) \end{pmatrix} , \tag{3.27}$$

The dependence of $\mathbf{\Gamma}^{(0)}$ on the coupling λ is only in the $\psi\psi$-component and is linear. A finite effective action implies vanishing ψ but does not constrain $\tilde{\psi}$ in the strong coupling (Dirichlet) limit. Note that the quadratic form $\Gamma^{(0)}[\psi, \tilde{\psi}]$ is an indefinite metric on the function space.

The vertex function $\mathbf{\Gamma}^{(0)}(\kappa_n)$ is diagonal in the Fourier-space of $(\mathbf{k}, \zeta_n)$-modes and the free energy can be obtained,

$$\frac{1}{2}\ln[-\det \mathbf{\Gamma}^{(0)}(\kappa_n)] = \frac{1}{2}\ln(\frac{4\Delta_n}{1-t_n}) = \frac{1}{2}\ln(\Delta_n) + \frac{1}{2}\ln(1+\frac{\lambda}{2\kappa_n}) + \ln 2 . \tag{3.28}$$

Comparing with Eqs. (A.1) and (A.6), Eq.(3.28) is interpreted as the contribution to the free energy of a thermal mode in the presence of two parallel flat plates. Eq.(3.28) includes the contribution to the free energy due to the plate itself but not that due to the other (distant) plate. This corroborates that the (negative) effective action for the surface modes of a flat plate is given by Eq.(3.27).

3.2.2 Vertices

The interaction in Eq.(3.10) is quadratic in the scalar ϕ and the profile $h(\mathbf{x})$ is not dynamic. Primitive vertices thus are diagonal in the Matsubara frequency and we

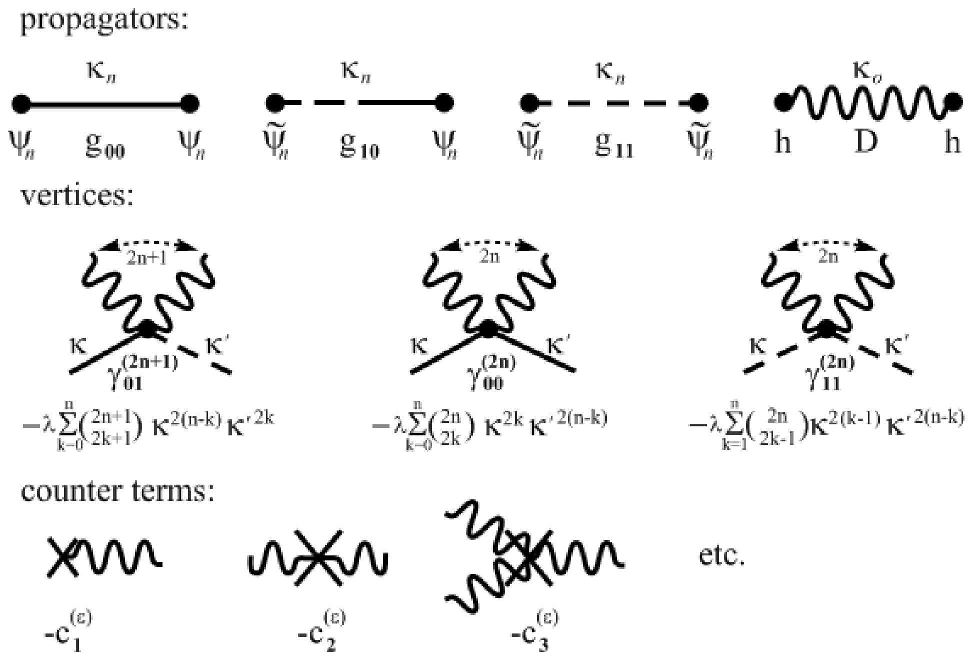

Figure 3.1: Propagators, vertices and counter terms of the $2+1$ dimensional field theory on the planar surface. The 'roughness field' h corresponds to wavy- and the two dynamical surface fields to solid- and dashed- lines. Counter term vertices are depicted as crosses. Apart from c_1, the theory only requires counter terms with an *even* number of h-legs. See the main text for details.

need only specify their dependence on $\kappa_n = \sqrt{\zeta_n^2 + \mathbf{k}^2}$ and $\kappa_n' = \sqrt{\zeta_n^2 + \mathbf{k}'^2}$. The interaction $H_{\text{int}}^{(1)}$ in Eq.(3.10b) leads to transitions between the ψ- and $\tilde{\psi}$-modes. It corresponds to the three-point vertex $\gamma_{10}^{(1)}$ in fig. 3.1,

$$\gamma_{01}^{(1)}(\kappa, \kappa') = \gamma_{10}^{(1)}(\kappa', \kappa) = -\lambda \ . \tag{3.29}$$

Expressions for primitive $(m+2)$-point vertices $\gamma^{(m)}$ with m external roughness profiles are similarly obtained from Eq.(3.10b) by noting that in Fourier space $(\partial/\partial a)^m \phi_n(\mathbf{k}, a)$ may be replaced by $\kappa_n^2 (\partial/\partial a)^{m-2} \phi_n(\mathbf{k}, a)$ due to Eq.(3.20). Primitive vertices with an odd number of profiles leading to transitions between ψ and $\tilde{\psi}$ modes are,

$$\gamma_{01}^{(2n+1)}(\kappa, \kappa') = \gamma_{10}^{(2n+1)}(\kappa', \kappa) = -\lambda \sum_{k=0}^{n} \binom{2n+1}{2k} \kappa^{2k} \kappa'^{\,2(n-k)} \ . \tag{3.30}$$

Vertices with an even number of profiles do not cause transitions between ψ and $\tilde{\psi}$ fields,

$$\gamma_{00}^{(2n)}(\kappa,\kappa') = -\lambda \sum_{k=0}^{n} \binom{2n}{2k} \kappa^{2k}\kappa'^{\,2(n-k)}$$
$$\gamma_{11}^{(2n)}(\kappa,\kappa') = -\lambda \sum_{k=1}^{n} \binom{2n}{2k-1} \kappa^{2(k-1)}\kappa'^{\,2(n-k)} \ . \qquad (3.31)$$

The diagrammatic form of these vertices is shown in fig. 3.1.

Introducing the Fourier-transform $h(\mathbf{k}) = \int d\mathbf{x} e^{i\mathbf{k}\mathbf{x}} h(\mathbf{x})$ of the profile, the primitive vertices may be collected to vertex functionals generating the interactions of the n^{th} Matsubara mode with the profile,

$$\begin{aligned}
V_n^{00}(\mathbf{k},\mathbf{k}') &:= \frac{1}{\lambda}\sum_{m=1}^{\infty}\frac{(2\pi)^2}{(2m)!}\left[\prod_{j=1}^{2m}\int\frac{d\mathbf{k}_j}{(2\pi)^2}h(\mathbf{k}_j)\right]\delta(\mathbf{k}+\mathbf{k}'+\sum_{j=1}^{2m}\mathbf{k}_j)\ \gamma_{00}^{(2m)}(\kappa_n,\kappa_n') \\
V_n^{01}(\mathbf{k},\mathbf{k}') &:= \frac{1}{\lambda}\sum_{m=0}^{\infty}\frac{(2\pi)^2}{(2m+1)!}\left[\prod_{j=1}^{2m+1}\int\frac{d\mathbf{k}_j}{(2\pi)^2}h(\mathbf{k}_j)\right]\delta(\mathbf{k}+\mathbf{k}'+\sum_{j=1}^{2m+1}\mathbf{k}_j) \\
&\times\ \gamma_{01}^{(2m+1)}(\kappa_n,\kappa_n') \\
V_n^{10}(\mathbf{k},\mathbf{k}') &:= V_n^{01}(\mathbf{k}',\mathbf{k}) \qquad (3.32) \\
V_n^{11}(\mathbf{k},\mathbf{k}') &:= \frac{1}{\lambda}\sum_{m=1}^{\infty}\frac{(2\pi)^2}{(2m)!}\left[\prod_{j=1}^{2m}\int\frac{d\mathbf{k}_j}{(2\pi)^2}h(\mathbf{k}_j)\right]\delta(\mathbf{k}+\mathbf{k}'+\sum_{j=1}^{2m}\mathbf{k}_j)\ \gamma_{11}^{(2m)}(\kappa_n,\kappa_n')\ .
\end{aligned}$$

Together with Eq.(3.26) the interactions of Eq.(3.32) determine the vertex functional $\Gamma[\psi,\tilde{\psi};h]$ for any given profile $h(\mathbf{x})$,

$$\Gamma[\psi,\tilde{\psi};h] = \Gamma^{(0)}[\psi,\tilde{\psi}] + \Gamma^{(h)}[\psi,\tilde{\psi}] \qquad (3.33)$$

with,

$$\begin{aligned}
\Gamma^{(h)}[\psi,\tilde{\psi}] &= \frac{\lambda}{2}\sum_n\int\frac{d\mathbf{k}d\mathbf{k}'}{(2\pi)^4}(\psi_n(\mathbf{k}),\tilde{\psi}_n(\mathbf{k}))\cdot\mathbf{V}_n[h](\mathbf{k},\mathbf{k}')\cdot\begin{pmatrix}\psi_n(\mathbf{k}')\\ \tilde{\psi}_n(\mathbf{k}')\end{pmatrix} \\
\mathbf{V}_n[h] &= \begin{pmatrix} V_n^{00} & V_n^{01} \\ V_n^{10} & V_n^{11}\end{pmatrix} \ . \qquad (3.34)
\end{aligned}$$

3.2.3 Counter terms

The 2-point correlation function of the roughness profile of Eq.(3.23d) decays exponentially at large momenta and the vertex functional given by Eq.(3.33) is quadratic in the field ϕ. One-particle-irreducible (1PI) vertex functions with only external ϕ-fields thus are finite if all 1PI vertices with only external roughness fields are. One therefore only requires counter terms for n-point vertex functions of the roughness profile.

The 1-point counterterm, $c_1^{(\varepsilon)}$, is finite for $\varepsilon \to 0^+$ and vanishes for $a \to \infty$. This counterterm is necessary for an unambiguous definition of the separation a. It ensures that Eq.(2.43) holds at all temperatures, separations and couplings. The parameter a otherwise would not always represent the mean separation of the plates. $c_1^{(\varepsilon)}$ is the only counterterm that depends on the plate separation a, temperature T and *both* coupling constants λ and $\bar{\lambda}$. To leading order in the loop expansion, the equation $\langle h\rangle = 0$ is depicted in the first line of fig. 3.2 and given by,

$$\begin{aligned} \left[\frac{\delta Z^{(\varepsilon)}[j,\alpha;T,a]}{\delta\alpha}\right]_{\alpha=0} &= \langle h(\mathbf{x})\rangle = 0 \\ &= c_1^{(\varepsilon=0)}(a;\lambda,\bar{\lambda}) - T\sum_n \int \frac{d\mathbf{k}}{(2\pi)^2}\gamma_{10}^{(1)}(\kappa,\kappa')g_{10}(\kappa_n) \end{aligned} \tag{3.35}$$

we obtain,

$$\begin{aligned} c_1^{(\varepsilon=0)}(a;\lambda,\bar{\lambda})\Big|_{\text{1-loop}} &= -T\lambda\sum_n\int\frac{d\mathbf{k}}{(2\pi)^2}g_{10}(\kappa_n) = -\frac{\partial}{\partial a}\frac{T}{4\pi}\sum_{n=-\infty}^{\infty}\int_{2\pi|n|T}^{\infty}\kappa d\kappa\ln(\Delta) \\ &= -\frac{\partial}{\partial a}f^{(2)}(T;\lambda,\bar{\lambda},a) \\ &\xrightarrow[\lambda,\bar{\lambda}\sim\infty]{} -\frac{\partial}{\partial a}\sum_{m=-\infty}^{\infty}\sum_{n=1}^{\infty}\frac{-a/\pi^2}{[(2na)^2+(m/T)^2]^2} \xrightarrow[2Ta\ll 1]{} -\frac{\pi^2}{480a^4} \end{aligned} \tag{3.36}$$

where $f^{(2)}(T;\lambda,\bar{\lambda},a)$ is the Casimir free energy per unit area at finite temperature on two semitransparent plates due to a massless scalar field given in Eq.(A.6). The last line in Eq.(3.36) reproduces the Casimir pressure on Dirichlet plates

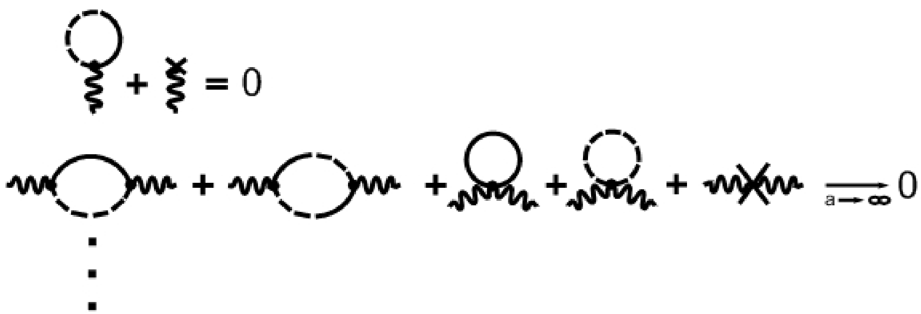

Figure 3.2: Feynman graphs for c_1 and c_2 counter-terms to one loop. c_1 is finite but eliminates all tadpole contributions and guarantees that $\langle h \rangle = 0$ for any coupling, temperature and separation. Counter terms $c_2, c_4, \ldots$ are local and guarantee that corrections to prescribed roughness correlations vanish at $T = 0$ in the limit $a \to \infty$.

at finite [66] and at zero temperature [5]. It is no coincidence that $c_1^{(\varepsilon)}$ is the Casimir pressure since this counter term compensates for changes in the Casimir free energy due to $\langle h \rangle \neq 0$. Since it maintains $\langle h \rangle = 0$, the counterterm $c_1^{(\varepsilon=0)}$ cancels all one-particle reducible contributions to the free energy.

Counterterms with more than one external roughness field ensure that prescribed correlation functions of the profile remain unchanged at $T = 0$ when the two plates are (infinitely) far apart. Since $g_{01}^{(f)} = 0$, counter terms with an *odd* number of external h-fields vanish in the limit $a \to \infty$. These counter terms by definition depend only on the coupling λ and on the cutoff ε and can be computed using the fast parts of propagators in Eq.(3.23) that survive the $a \to \infty$ limit. Apart from c_1 the model requires only counter terms $c_{2n}^{(\varepsilon)}$ with an even number of external roughness profiles. To leading order in the loop expansion, $c_2^{(\varepsilon)}(q;\lambda)$ is obtained by evaluating the second row of diagrams in fig 3.2 at $T = 0$ in the limit $a \to \infty$. For $1/\lambda \gg \varepsilon \to 0^+$

$$\lim_{a\to\infty} \Big[\frac{\delta^2 Z^{(\varepsilon)}[j,\alpha;T,a]}{\delta\alpha\delta\alpha'} \Big]_{\alpha,\alpha'=0} = \langle h(\mathbf{k}) h(-\mathbf{k}) \rangle = d^{(f)}(\kappa_0) \tag{3.37}$$

one obtains,

$$
\begin{aligned}
c_2^{(\varepsilon)}(q;\lambda) &= \frac{\lambda^2}{2}\int_{-\infty}^{\infty}\frac{d\zeta}{2\pi}\int\frac{d\mathbf{k}}{(2\pi)^2}\frac{(\kappa-\kappa' e^{-\varepsilon\kappa'})e^{-\varepsilon\kappa}}{2\kappa+\lambda} \quad \text{with} \quad \begin{aligned}\kappa^2 &= \zeta^2+\mathbf{k}^2\\ \kappa'^2 &= \zeta^2+(\mathbf{q}-\mathbf{k})^2\end{aligned}\\
&= \frac{\lambda^2}{32\pi^2}\left[\frac{7}{\varepsilon^3}-\frac{3\lambda}{2\varepsilon^2}+\frac{3\lambda^2-q^2}{6\varepsilon}+\frac{q^2\lambda(23-24\gamma_E-24\ln(\varepsilon\lambda))}{36}+\right.\\
&\quad \left.+\frac{\lambda^3(1-3\ln 2)}{6}+\frac{5q\lambda^2}{6}+\frac{q^3}{3}-\frac{\lambda(\lambda+2q)^3}{12q}\ln(1+\frac{2q}{\lambda})+\mathcal{O}(\lambda\varepsilon)\right]
\end{aligned} \tag{3.38}
$$

For Dirichlet boundary conditions on considers the strong coupling limit $0 < 1/\lambda \ll \varepsilon \to 0^+$. The two-point counter term in this case simplifies to,

$$
c_2^{(\varepsilon)}(q;\infty) = \frac{\lambda}{2}\int_{-\infty}^{\infty}\frac{d\zeta}{2\pi}\int\frac{d\mathbf{k}}{(2\pi)^2}(\kappa-\kappa' e^{-\varepsilon\kappa'})e^{-\varepsilon\kappa} = \frac{\lambda}{32\pi^2}\left[\frac{45}{\varepsilon^4}+\frac{q^2}{6\varepsilon^2}+\frac{q^4}{24}\right]+\mathcal{O}(q\varepsilon) \tag{3.39}
$$

The Feynman rules derived above define the loop expansion of this model. The total transverse momentum and thermal mode number are conserved at each vertex (assigning the time-independent h-field the Matsubara frequency $\zeta_n = 0$). This is a 2+1-dimensional thermal field theory: the presence of another plate in a third spatial dimension manifests itself in the non-local dependence of propagators on the length scale "a". From the point of view of the two-dimensional brane, this length scale could as well represent the Compton wave length of a massive particle. The model on the surface is holographic in the sense of [67, 68, 69].

3.3 The Dirichlet (strong coupling) limit

The vertices $\gamma_{00}^{(2n)}$, $\gamma_{11}^{(2n)}$, $\gamma_{01}^{(2n+1)}$, and $\gamma_{10}^{(2n+1)}$ in Eqs. (3.30) and (3.31) are all proportional to λ. To leading order in the strong coupling expansion, the propagators g_{00}, g_{01}, g_{10} are of order λ^{-1} and g_{11} is of order λ^0. The leading superficial order in λ of a Feynman diagram, N_λ, in the strong coupling regime thus is given by,

$$
N_\lambda = \#\gamma_{00} + \#\gamma_{01} + \#\gamma_{10} + \#\gamma_{11} - \#g_{00} - \#g_{01} - \#g_{10} \,, \tag{3.40}
$$

where $\#X$ denotes the number of X's the diagram is composed of. Moreover the model conserves the number of scalar surface fields and the ψ and $\tilde{\psi}$ fields of propagators correspond to those of vertices, since the action is quadratic and $\langle h(\mathbf{x})\rangle$ vanishes. *Vacuum* diagrams thus satisfy the additional constraints,

$$\begin{aligned}
2\#\gamma_{00} + \#\gamma_{01} + \#\gamma_{10} &= 2\#g_{00} + \#g_{01} + \#g_{10} \\
2\#\gamma_{11} + \#\gamma_{01} + \#\gamma_{10} &= 2\#g_{11} + \#g_{01} + \#g_{10} \\
\#\gamma_{01} = \#\gamma_{10} \quad &, \quad \#g_{01} = \#g_{10} \ .
\end{aligned} \tag{3.41}$$

Combining Eq.(3.41) with Eq.(3.40), the leading superficial order of an individual connected vacuum diagram is given by the number of g_{11} (λ^0 order) propagators it contains,

$$N_\lambda(\text{vac}) = \#g_{11} = \#\gamma_{11} + \#g_{00} - \#\gamma_{00} \ . \tag{3.42}$$

If the strong coupling (Dirichlet) limit of the free energy is to exist, superficially divergent contributions with $N_\lambda(\text{vac}) > 0$ have to cancel. Such delicate cancellations generally arise due to underlying symmetries and are the consequence of associated Ward identities. A finite strong coupling limit for *any* profile in this sense is a non-trivial condition on the surface model defined by Eq.(3.33) and Eq.(3.34). That a Ward-like identity may ensure the existence of the strong coupling limit is suggested by the vertex functional $\Gamma^{(0)}$ for a flat plate given in Eq.(3.27). It evidently satisfies the identity,

$$\frac{\delta}{\delta\tilde{\psi}_n(\mathbf{k})}\frac{\partial}{\partial\lambda}\Gamma^{(0)} = 0 \ . \tag{3.43}$$

Eq.(3.43) can be interpreted as stating that for vanishing profile the normal derivative $\tilde{\psi}$ need not vanish when Dirichlet boundary conditions are enforced. The original interaction with the profile by the δ-function potential of Eq.(3.9) constrains the ϕ-field at strong coupling but not its normal derivative. The strong coupling limit otherwise would not correspond to Dirichlet boundary conditions.

Even for non-vanishing profile, when ψ and $\tilde{\psi}$ are coupled by $V^{01}[h]$, the strong coupling limit must not require *both* surface fields to vanish. One therefore expects an h-dependent linear combination of ψ and $\tilde{\psi}$ to survive strong coupling and a generalization of Eq.(3.27) to hold for the vertex functional $\Gamma[\psi, \tilde{\psi}; h]$. Writing the linear combination of thermal modes in terms of an h-dependent functional $A_n[h]$, the generalization of Eq.(3.43) takes the form,

$$\left[\frac{\delta}{\delta\tilde{\psi}_n(\mathbf{k})} + \int \frac{d\mathbf{k}'}{(2\pi)^2} A_n(\mathbf{k}, \mathbf{k}'; h) \frac{\delta}{\delta\psi_n(\mathbf{k}')}\right] \frac{\partial}{\partial\lambda} \Gamma[\psi, \tilde{\psi}; h] = 0 \ . \tag{3.44}$$

Inserting Eq.(3.33) and Eq.(3.34) in Eq.(3.44) and varying $\psi(\mathbf{k})$ and $\tilde{\psi}(\mathbf{k})$ leads to the two functional relations,

$$A_n[h] \cdot (\mathbb{1} - V_n^{00}[h]) = V_n^{10}[h] \quad \text{and} \quad A_n[h] \cdot V_n^{01}[h] + V_n^{11}[h] = 0 \ . \tag{3.45}$$

A solution $A_n[h]$ to Eq.(3.45) exists only if,

$$V_n^{11}[h] + V_n^{10}[h](\mathbb{1} - V_n^{00}[h])^{-1} V_n^{01}[h] = 0 \ , \tag{3.46}$$

for any profile h. We have explicitly verified Eq.(3.46) to sixth order in the profile $h(\mathbf{k})$. Although we here do not provide a (combinatoric) proof of Eq.(3.46) to all orders, note that Eq.(3.44) determines $A[h]$ and $V^{11}[h]$ for any choice of V^{10} and V^{00}. Requiring that solutions to the wave equation with Dirichlet boundary conditions are not trivial in this sense determines the interaction $V_n^{11}[h]$ in terms of $V^{10}[h]$ and $V^{00}[h]$. Eq.(3.46) can be viewed as generating γ_{11}-vertices that are consistent with proposed γ_{01} and γ_{00} vertices. It is an indication of the consistency of the model that we can verify that vertices with up to six external roughness fields indeed satisfy Eq.(3.46). We will not require higher vertices in our calculations and may safely assume that Eq.(3.46) in fact holds to all orders in this model.

We still need to show that Eq.(3.46) is sufficient for a finite strong coupling limit of the effective action. In the following a connected Feynman diagram

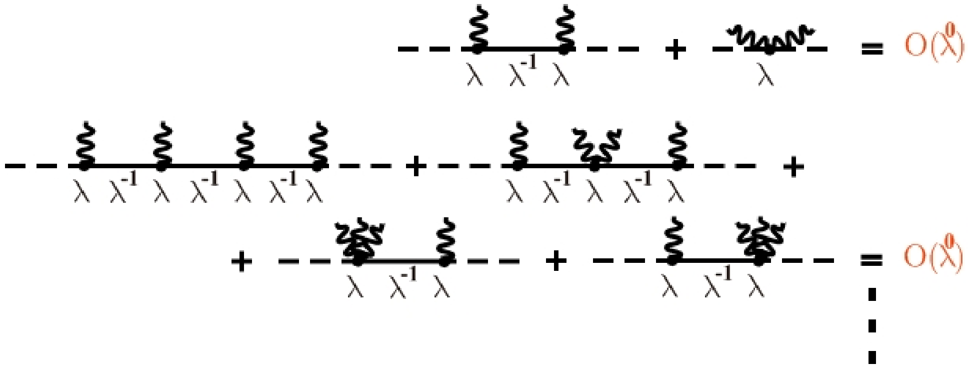

Figure 3.3: Cancellation of the leading order in λ of contributions to $\tilde{\psi}$-irreducible $\tilde{\psi}\tilde{\psi}$-vertices. The solid lines represent g_{00}-propagators which at strong coupling are $\lambda^{-1} + \mathcal{O}(1)$. $\tilde{\psi}$-irreducible $\tilde{\psi}\tilde{\psi}$-vertices thus are of leading superficial $\mathcal{O}(\lambda)$. For the vertices of Eqs. (3.31) and (3.30), the leading superficial order cancels for any set of momenta and $\tilde{\psi}$-irreducible $\tilde{\psi}\tilde{\psi}$-vertices in fact are of $\mathcal{O}(1)$.

is called $\tilde{\psi}$-reducible if it becomes disjoint by removing a single g_{11} propagator and any number of d-propagators[1]. In this quadratic model, a vertex thus is $\tilde{\psi}$-irreducible only if it contains no internal g_{11} propagators. The analog of Eq.(3.41) for a $\tilde{\psi}$-irreducible vertex diagram with two external $\tilde{\psi}$-lines and no internal g_{11} propagators implies that,

$$
\begin{aligned}
2\#\gamma_{00} + \#\gamma_{01} + \#\gamma_{10} &= 2\#g_{00} + \#g_{01} + \#g_{10} \\
2\#\gamma_{11} + \#\gamma_{01} + \#\gamma_{10} &= 2 + \#g_{01} + \#g_{10}.
\end{aligned} \tag{3.47}
$$

Its leading superficial order in λ therefore is,

$$
\begin{aligned}
N_\lambda(\tilde{\psi}\text{-irred. } \tilde{\psi}\tilde{\psi}\text{-vertex}) &= \#\gamma_{00} + \#\gamma_{01} + \#\gamma_{10} + \#\gamma_{11} - \#g_{00} - \#g_{01} - \#g_{10} \\
&= \#\gamma_{11} + \#g_{00} - \#\gamma_{00} = 1\ .
\end{aligned} \tag{3.48}
$$

Eq. (3.46) on the other hand implies that the leading order in λ of all contributions to an $\tilde{\psi}$-irreducible $\tilde{\psi}\tilde{\psi}$-vertex in fact cancels. The superficial order in λ in Eq.(3.48) does not account for this cancellation among contributions of the

[1]A diagram that can only be separated by cutting g_{00}, g_{01}, g_{10} propagators and any number of h-lines is $\tilde{\psi}$-irreducible. A one-particle reducible diagram thus can be $\tilde{\psi}$-irreducible.

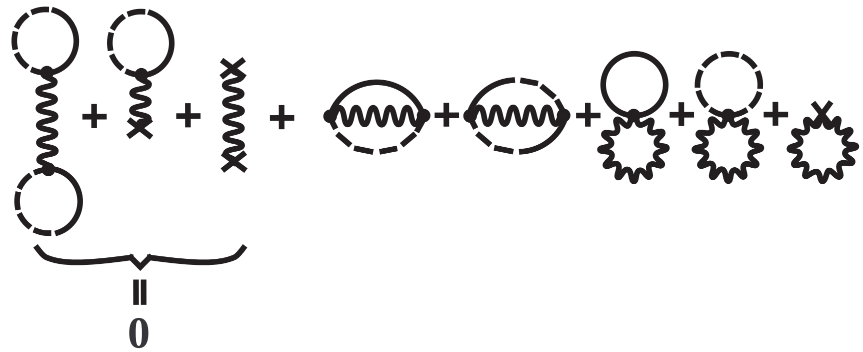

Figure 3.4: Two-loop vacuum diagrams

same superficial order and a $\tilde{\psi}$-irreducible $\tilde{\psi}\tilde{\psi}$-vertex therefore is at most of order λ^0.

The superficial order in the coupling λ of a vacuum diagram was found to be just $\#g_{11}$ in Eq.(3.42). This is precisely the number of $\tilde{\psi}$-irreducible $\tilde{\psi}\tilde{\psi}$-vertices the diagram contains. Since we have just seen that Eq.(3.46) implies that a $\tilde{\psi}$-irreducible $\tilde{\psi}\tilde{\psi}$-vertex in fact contributes at most in $\mathcal{O}(\lambda^0)$, the combined contribution to the free energy of all vacuum diagrams with a given number of g_{11} propagators also is at most of order $\mathcal{O}(1)$. Eq.(3.44) thus ensures a finite free energy in the strong coupling (Dirichlet) limit.

3.4 Two-loop contribution to the free energy: the leading roughness correction

The two-loop vacuum diagrams of Fig. 3.4 give the leading roughness correction to the free-energy. The contribution from the last five diagrams is,

$$\begin{aligned}\Delta f^{(2)} &= \Big(V_n^{10} g_{00}(\kappa_n') V_n^{01} g_{11}(\kappa_n) + V_n^{10} g_{01}(\kappa_n') V_n^{10} g_{01}(\kappa_n)\Big)_{m=0} d(\mathbf{k}-\mathbf{k}') \\ &+ \Big(V_n^{00} g_{00}(\kappa_n) + V_n^{11} g_{11}(\kappa_n) + c_{2n}^{(\varepsilon)}\Big)_{m=1} d(0) \qquad (3.49)\end{aligned}$$

The evaluation of Eq.(3.49) simplifies and is more transparent in the Dirichlet limit for both plates. The correction to the Casimir free energy per unit area of a massless scalar field for two parallel plates due to roughness of one plate in this case is given by the expression [70],

$$\Delta f_{\rm D}^{(2)}(\sigma,\ell;a,T) = -T\sum_n \int \frac{d\mathbf{k}d\mathbf{k}'}{(2\pi)^4}\frac{\kappa_n\kappa'_n\, d(\mathbf{k}-\mathbf{k}')}{(e^{2a\kappa_n}-1)(1-e^{-2a\kappa'_n})}\ , \tag{3.50}$$

where $d(\mathbf{k}-\mathbf{k}')$ is the two-point correlation function of the roughness profile. There in addition is a correction to the free energy due to roughness of an isolated plate. It does not depend on the separation a and therefore does not lead to a modification of the force on a rough plate and will be ignored. The correction to the interaction of Eq.(3.50) depends on the exact form of $d(\mathbf{k}-\mathbf{k}')$, but some conclusions about its general behavior can be drawn in the limit of large ($\ell \gg a$) and of small ($\ell \ll a$) correlation length.

For $\ell \gg a$, the support of the roughness correlation $d(\mathbf{k}-\mathbf{k}')$ is restricted to $|\mathbf{k}-\mathbf{k}'|a \ll 1$. One may replace κ' by κ in the integrand without large error. With $\sigma^2 = (2\pi)^{-2}\int d\mathbf{k}d(\mathbf{k})$ this gives the universal limit,

$$\begin{aligned}\Delta f_{\rm D}^{(2)}(\sigma,\ell\gg a,T) &\sim -\frac{\sigma^2}{2}\frac{\partial^2}{\partial a^2}f^{(2)}(T;\lambda\to\infty,\bar\lambda\to\infty,a) \\ &= \frac{\sigma^2}{2}\frac{\partial^2}{\partial a^2}\sum_{m=-\infty}^{\infty}\sum_{n=1}^{\infty}\frac{-a/\pi^2}{[(2na)^2+(m/T)^2]^2} \quad \xrightarrow[2Ta\ll 1]{} \quad -\frac{\pi^2\sigma^2}{240a^5}\ ,\end{aligned} \tag{3.51}$$

which does not depend on the specific form of the correlation function $d(\mathbf{k})$. As should be expected [71], Eq.(3.51) coincides with the roughness correction in limit of large correlation length so-called proximity force approximation (PFA) [72, 16].

In the opposite limit of short correlation length, $\ell \ll a$, or at large separations, the $\mathbf{k}$-integral is exponentially restricted to the domain $|\mathbf{k}| \lesssim 1/a$ whereas the $\mathbf{k}'$-integral in Eq.(3.50) is finite only because roughness correlations are negligible for $|\mathbf{k}'| \gg 1/\ell \gg 1/a$. The leading behavior of the roughness correction at

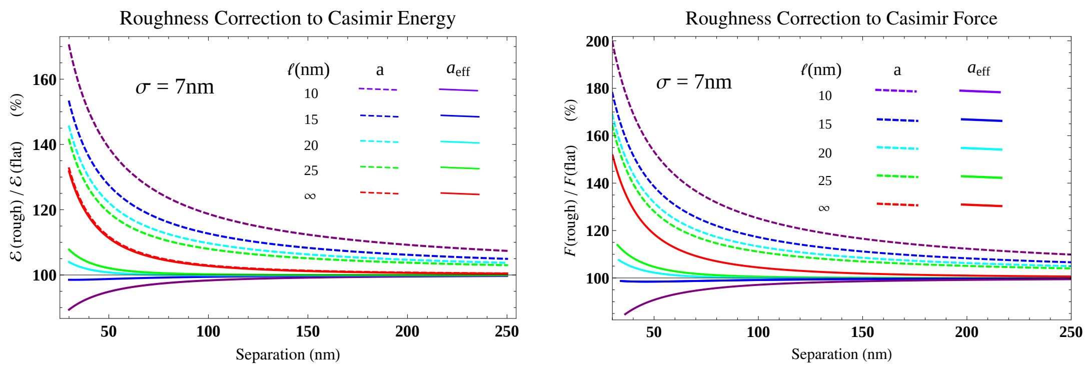

Figure 3.5: (color online) Relative roughness corrections to the Casimir energy and Casimir force in % due to a scalar satisfying Dirichlet boundary conditions on two plates, one of which is flat, the profile of the other is characterized by its variance $\sigma^2 = 49\text{nm}^2$ and correlation length ℓ. In two-loop approximation the correction is proportional to σ^2. Pairs of dashed and solid curves of the same color correspond to the same $\ell = 10\text{nm}$ (violet), 15nm (blue), 20nm (cyan), 25nm (green) and $\ell = \infty$ (from the outer pair of curves to the inner). Dashed curves represent the correction as a function of the mean separation a, whereas solid curves show it as a function of the effective separation $a_{\text{eff}} = a - \frac{\sigma^2}{\ell}\sqrt{\frac{\pi}{2}}$. The (red) PFA correction for $\ell = \infty$ is the same in both cases.

separations $a \gg \ell$ thus is,

$$\begin{aligned}\Delta f^{(2)}(\ell \ll a, \lambda \sim \infty) &\sim -\int \frac{d\mathbf{k}'}{(2\pi)^2} k'\, d(\mathbf{k}') \times T \sum_n \int \frac{d\mathbf{k}}{(2\pi)^2} \frac{\kappa_n}{(e^{2a\kappa_n} - 1)} \\ &= -\left(\frac{\sigma^2}{\ell}\sqrt{\frac{\pi}{2}}\right) \times \frac{\partial}{\partial a} f^{(2)}(T; \infty, \infty, a) \qquad (3.52) \\ &= f^{(2)}(T; \infty, \infty, a^D_{\text{eff}}) - f^{(2)}(T; \infty, \infty, a) + \mathcal{O}\left(\frac{\sigma^4}{a^5 \ell^2}\right) ,\end{aligned}$$

where $f^{(2)}(T; \infty, \infty, a)$ is the free energy of Eq.(A.6) for two flat parallel Dirichlet planes at separation a and

$$a^D_{\text{eff}} = a - \int \frac{d\mathbf{k}}{(2\pi)^2} k\, d(\mathbf{k}) \sim a - \frac{\sigma^2}{\ell}\sqrt{\frac{\pi}{2}} \,. \qquad (3.53)$$

The shift away from the mean of the profile is always of order σ^2/ℓ, but the proportionality constant depends somewhat on the shape of the correlation function $d(\mathbf{k})$ and is $\sqrt{\pi/2} \sim 1.25\ldots$ for the one of Eq.(3.23d) only. Note that this displacement in the apparent surface of the profile is within the "thickness" of the profile for $\sigma < \ell$. This mild condition is a requirement for the validity of the loop expansion and generally is satisfied by natural surfaces whose roughness is due to random dislocations of surface atoms. However, it should be noted that surfaces with $\sigma > \ell$ can be artificially created. In this case a loop expansion of the free energy in σ^2/ℓ^2 is not applicable [73, 74].

Even though the shift in Eq.(3.53) generally is quite small and well within the profile's thickness, its effect on the roughness correction can be dramatic. As shown in Fig. 3.5, or as can be deduced by examining Eq.(3.50), the perturbative roughness correction tends to *increase* with *decreasing* correlation length when the mean separation between the two plates is used as reference. The correction is quite large even for $a \gg \ell$ and easily exceeds 20% at experimentally accessible separations for typical roughness profiles [50, 51, 75]. However, this effect to a great extent is eliminated by redefining the effective planar 'surface' of a rough plate. As shown in Fig. 3.5, the residual roughness correction *decreases* with *decreasing* correlation length ℓ if the effective separation a^D_{eff} of Eq.(3.53) is used for the separation. Thus, at least to leading order in the loop expansion, the main effect of roughness is to define the reference plane of the plate. This reference plane generally is *not* the mean of the profile.

To determine the absolute separation of rough plates can be experimentally challenging. The previous considerations suggest that one could instead experimentally calibrate the (effective) separation of two plates in a manner that eliminates asymptotic $1/a^4$ corrections to the Casimir interaction energy of flat parallel plates (or asymptotic $1/a^5$-corrections to the force). In terms of this definition of the separation, the leading asymptotic correction to the force for large $a \gg \ell$ is of order $1/a^6$ only. Note that PFA-corrections, corresponding to infinite correlation length, are of this order and are not altered by this procedure. Such an intrinsic determination of the effective separation a^D_{eff} eliminates systematic errors due to electrostatic and other means of deducing the average separation of rough surfaces and facilitates a theoretical interpretation of experiments. However, the suggested calibration suffers from the fact that the Casimir force and therefore the signal-to-noise ratio decrease rapidly with increasing separation. A truly asymptotic calibration is impractical and a compromise necessary. Fig. 3.5 suggests that intermediate separations (100nm $< a <$ 300nm) could be used to optimize this procedure in most experimental situations. In terms of the asymptotically optimal separation, corrections to the Casimir force of two flat plates are much smaller and under better theoretical control.

An improved definition of the effective separation is necessary to avoid the conclusion that unitarity is violated because the reflection coefficient of a rough plate at long wavelengths ($a \gg \ell$) is larger than for a perfectly reflecting mirror. With an improved definition, the scattering matrix of a rough plate and the corresponding Casimir force ought to both *decrease* in magnitude compared to those for a flat (perfectly reflecting) Dirichlet plate. One furthermore expects the scattering matrix and Casimir force to *decrease* in magnitude with decreasing ℓ for $a \gg \ell$. Both physical requirements are met for $a \gg \ell$ by using the effective separation a^D_{eff} defined in Eq.(3.53). The corresponding force is always weaker than the PFA suggests. We now show that this improved definition of the separation to a rough plate leads to a scattering matrix with acceptable properties in the limit $\ell \ll a$.

3.5 The limit $a \gg \ell$: An effective low-energy field theory.

In the limit $\ell \ll a$ the two-point correlation function $D_2(\mathbf{x})$ of the profile is *localized* to $|\mathbf{x}| \lesssim \ell \ll a$ and we can use renormalization group techniques[76] to analyze the situation. In this limit we can approximately "integrate out" high momentum contributions and construct an effective theory of surface fields for wave numbers $|\mathbf{k}| \lesssim 1/a$. In the present model, the separation of momentum scales already occurs for tree-level surface field propagators. In Eq.(3.23) they naturally decompose into (f)ast and (s)oft components.

A local vertex $v_{N\tilde{N}}$ of the effective low-energy theory corresponds to the sum of all connected diagrams that contain only (f)ast internal propagators and have $2N$ (s)oft external ψ- and $2\tilde{N}$ (s)oft external $\tilde{\psi}$-fields and no external h-fields. Because $g_{01}^{(f)} = 0$, the effective local vertices do not mix dynamical surface fields and conserve the number of ψ- and $\tilde{\psi}$- fields individually. They vanish unless the number of external ψ and $\tilde{\psi}$ fields are *both* even. Since the range of the roughness correlation $D_2(\mathbf{x} - \mathbf{y})$ vanishes, these vertices are local in the limit $\ell \to 0$ and by construction do not depend on the presence of another plate at separation a and coupling $\bar{\lambda}$. Closed loops of fast surface fields correspond to separation-independent corrections to roughness-correlations that are precisely canceled by the corresponding counter terms at $T = 0$. At low temperatures it therefore suffices to consider connected vertex diagrams with only fast internal propagators and no closed internal loops of dynamical surface field propagators. The effective local vertices are finite since all loop momenta are restricted to $|\mathbf{k}|\ell \lesssim 1$ by the roughness-correlations, but some tend to diverge for $\ell \to 0$. To determine the degree of divergence with ℓ, note that the number, L, of transverse momentum loops of a connected vertex diagram with $2(N + \tilde{N})$ external surface fields is given by,

$$L = \#d + 1 - N - \tilde{N} \tag{3.54}$$

where $\#d$ is the number of roughness-propagators $d(\mathbf{k})$ the diagram contains. To determine the dimension of the $N\tilde{N}$-vertex, $v_{N\tilde{N}}$, we first consider the effective action for the roughness interaction,

$$\begin{aligned} \Gamma^{(int)}[\psi, \tilde{\psi}] &= \int \frac{d\mathbf{k}_1 ... d\mathbf{k}_{2N}\ d\tilde{\mathbf{k}}_1 ... d\tilde{\mathbf{k}}_{2\tilde{N}}}{(2\pi)^{4(N+\tilde{N})}} \delta^2(\mathbf{k}_1 - ... - \mathbf{k}_{2N} - \tilde{\mathbf{k}}_1 - ... - \tilde{\mathbf{k}}_{2\tilde{N}}) \\ &\times \quad \psi(\mathbf{k}_1) ... \psi(\mathbf{k}_{2N}) \cdot v_{N\tilde{N}} \cdot \tilde{\psi}(\mathbf{k}_1) ... \tilde{\psi}(\mathbf{k}_{2N}) \end{aligned} \tag{3.55}$$

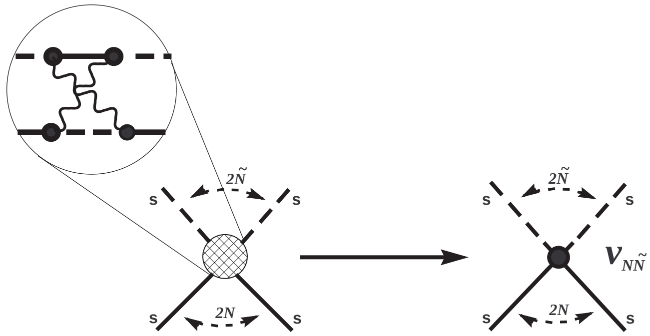

Figure 3.6: Localization of connected vertices in the $\ell \to 0$ limit. Only (f)ast components of internal dynamical surface propagators contribute. External momenta are limited to $|\mathbf{k}| < 1/a \ll 1/\ell$.

The restriction that $\Gamma^{(int)}[\psi, \tilde{\psi}]$ has *zero* canonical mass-dimension leads to the relation,

$$[\Gamma^{(int)}] = 0 = 4N + 4\tilde{N} - 2 + 2N[\psi] + [v_{N\tilde{N}}] + 2\tilde{N}[\tilde{\psi}] \tag{3.56}$$

Where [...] represents the mass-dimension. From the defination of Eq.(3.22) and the Green's function Eq.(3.20), we determine $[\psi] = -\frac{3}{2}, [\tilde{\psi}] = -\frac{1}{2}$. Therefore the mass-dimension $[v_{N\tilde{N}}]$ of a $N\tilde{N}$-vertex in transverse momentum space, follow Eq.(3.56), is,

$$[\lambda^{-2N} v_{N\tilde{N}}] = 2 - 3N - 3\tilde{N} \ . \tag{3.57}$$

In Eq.(3.57) a factor of λ^{-1} provided by $g_{00}^{(s)}$ and $g_{01}^{(s)}$ propagators in vacuum diagrams was included for each external ψ-field. We distinguish two extreme limits:

3.5.1 A rough Dirichlet plate: $1/\lambda \ll \ell \ll a$

For $1/\lambda \ll \ell$ the internal $g_{00}^{(f)}$ propagators, given in Eq.(3.23a), of an effective local vertex may be approximated by $1/\lambda$. $\lambda\ell \gg 1$ includes the case of Dirichlet boundary conditions on the rough plate and we for simplicity consider only this extreme limit. The leading contribution to an $N\tilde{N}$-vertex is proportional to λ^{2N} due to the cancellations observed in Sec. 3.3. Note that internal d-propagators of a diagram are proportional to σ^2. For vanishing external momenta (large internal momentum) Eqs. (3.54) and (3.57) then imply that the sum of L-loop contributions to the effective local vertex behaves as,

$$\lambda^{-2N} v^{(L)}_{N\tilde{N}} \propto \frac{\sigma^2}{\ell} \left(\sigma^2 \ell\right)^{N+\tilde{N}-1} \left(\frac{\sigma^2}{\ell^2}\right)^{L-1} \left(1 + \mathcal{O}\left((\lambda\ell)^{-1}\right)\right) \ , \tag{3.58}$$

in the strong coupling limit. Upon summing the all loop contributions, the local effective vertex at vanishing external momentum in the Dirichlet limit thus is of the form,

$$v^{D}_{N\tilde{N}} = \sum_{L=1}^{\infty} v^{(L)}_{N\tilde{N}} = \lambda^{2N} \frac{\sigma^2}{\ell} \left(\sigma^2 \ell\right)^{N+\tilde{N}-1} Q^{D}_{N\tilde{N}} \left(\frac{\sigma^2}{\ell^2}\right) \ , \tag{3.59}$$

where the dimensionless functions $Q^D_{N\tilde{N}}(s)$ are analytic at $s = 0$. We emphasize that the effective vertices reflect properties of the rough plate only. They do not depend on characteristics of the other parallel plate and we have the desired separation of scales. $\sigma^2/\ell^2 < 0.1$ for typical surfaces used in Casimir studies [45, 77, 50, 51, 75]. Low orders in the loop expansion therefore should provide fairly accurate local vertices $v^D_{N\tilde{N}}$ in the strong coupling limit.

Before proceeding to evaluate local effective vertices to leading order in the (hard) loop expansion, observe that the function $Q^D_{N\tilde{N}}$ in Eq.(3.59) depends on the two-point correlation function $d(\mathbf{k})$ and, in principle, also depends on higher correlation functions of the roughness profile. It therefore largely is a matter of perspective whether the vertices $v^D_{N\tilde{N}}$ of Eq.(3.59) or the correlation functions D_n of Eq.(2.42) are used to describe a rough plate in the low energy effective field theory. Of course, not every set of local vertices $v^D_{N\tilde{N}}$ corresponds to a physically realizable profile. A model of the correlations provides a basis for appropriate values and relations among the effective vertices $v^D_{N\tilde{N}}$ of the low-energy description. Nevertheless, within a certain domain, the phenomenological parameters of the low-energy effective theory in effect are the local vertices themselves. Assuming an analytic continuation of the functions $Q^D_{N\tilde{N}}(s)$ to $s > 1$ to exist, this effective low-energy description can be extended to a region of the parameter space where a loop-expansion is no longer feasible [73, 74].

Observe that the dependence of effective local vertices on external momenta of (s)oft fields gives rise to contributions to the free energy that are suppressed by powers of ℓ/a. To leading order in the loop expansion in σ^2/ℓ^2, Eq.(3.59) implies that effective local vertices with more than four (s)oft external fields can be ignored in the limit $\ell/a \to 0$. As in chiral perturbation theory [78] one arrives at an expansion in the canonical dimension of local vertices, those with more external fields becoming relevant at higher orders of the (soft) loop expansion only. Allowing for at most one hard internal loop, the low-energy effective model in the present limit (with the correlation function $d(\mathbf{k})$ of Eq.(3.23d)) is described by the following local effective vertices,

$$v_{01}^D = \ell^2\sigma^2 \int_0^\infty kdk \left[\frac{\lambda^2}{2k+\lambda} - \lambda\right] e^{-k^2\ell^2/2} \xrightarrow[\lambda\ell\gg 1]{} -\frac{\sigma^2}{\ell}\sqrt{2\pi}\delta_{\bar{n}\bar{n}'} \tag{3.60a}$$

$$v_{10}^D = -\lambda^2\ell^2\sigma^2 \int_0^\infty kdk \frac{k}{2} e^{-k^2\ell^2/2} \xrightarrow[\lambda\ell\gg 1]{} -\frac{\lambda^2\sigma^2}{4\ell}\sqrt{2\pi}\delta_{nn'} \tag{3.60b}$$

$$v_{02}^D = 2\pi\ell^4\sigma^4 \int_0^\infty kdk \left[\frac{2\lambda^4}{(2k+\lambda)^2} - \frac{4\lambda^3}{2k+\lambda} + 2\lambda^2\right] e^{-k^2\ell^2}$$

$$\xrightarrow[\lambda\ell\gg 1]{} 8\pi\sigma^4(\delta_{\bar{n}\bar{n}'}\delta_{\bar{m}\bar{m}'} + \delta_{\bar{n}\bar{m}'}\delta_{\bar{m}\bar{n}'} + \delta_{\bar{n}'\bar{m}'}\delta_{\bar{n}\bar{m}}) \tag{3.60c}$$

$$v_{11}^D = 2\pi\lambda^2\ell^2\sigma^2 + 2\pi\ell^4\sigma^4 \int_0^\infty kdk \left[\lambda^3 k - \frac{\lambda^4 k}{2k+\lambda}\right] e^{-k^2\ell^2}$$

$$\xrightarrow[\lambda\ell\gg 1]{} 2\pi\lambda^2\sigma^2(\ell^2(\delta_{n\bar{n}}\delta_{m\bar{m}} + \delta_{n\bar{m}}\delta_{m\bar{n}}) + \sigma^2\delta_{nm}\delta_{\bar{n}\bar{m}}) \tag{3.60d}$$

$$v_{20}^D = 2\pi\ell^4\sigma^4 \int_0^\infty kdk \frac{\lambda^4 k^2}{2} e^{-k^2\ell^2}$$

$$\xrightarrow[\lambda\ell\gg 1]{} \frac{\pi\lambda^4\sigma^4}{2}(\delta_{nn'}\delta_{mm'} + \delta_{nm'}\delta_{mn'} + \delta_{n'm'}\delta_{nm}) \tag{3.60e}$$

etc.

Only the final expressions of Eq.(3.60) include Kronecker symbols for the Matsubara modes [indices with a bar designate $\tilde{\psi}$ modes]. Note that the tree-level ("one-roughness-exchange") and one-loop contributions to v_{11} differ in the flow of mode indices. The individual terms of the intermediate expressions correspond to contributions to the vertex from topologically different diagrams.

The free energy of the effective low-energy theory with the (s)oft propagators of Eq.(3.23) and local vertices of Eq.(3.60) describes separation-dependent corrections due to the profile of a Dirichlet plate at separations $a \gg \ell$ from a smooth parallel plate. The free energy of the low-energy effective theory in powers of σ/a is obtained in the (s)oft loop expansion. The effective 2-point vertices v^D_{01} and v^D_{10} play a crucial rôle: they correct the low-energy behavior of propagators and thus affect all higher orders of the expansion as well.

The ratio $v^D_{10} : v^D_{01} = \lambda^2/4$ precisely compensates for the ratios of soft propagators $g^{(s)}_{11} : g^{(s)}_{10} : g^{(s)}_{00} = -\lambda/(2t)$ in the Dirichlet ($t \to t^D = 1$) limit. The roughness and separation-dependent correction, $\Delta f^{(2)}$, to the free energy per unit area of the effective low energy model thus is obtained by evaluating the 1-loop diagrams of Fig. 3.7 with an effective self-interaction $-2\rho^D = 2v^D_{01}$ for a soft scalar with propagator $g^{(s)}_{11}$,

$$\begin{aligned}
\Delta f^{(2)}_{\text{1-loop}}(\rho^D, a \gg \ell \gg 1/\lambda) &= -T \sum_n \int \frac{d\mathbf{k}}{(2\pi)^2} \sum_{k=1}^{\infty} \frac{1}{2k} \left(2\rho^D \frac{\kappa_n \bar{t}_n e^{-2\kappa_n a}}{2\Delta_n} \right)^k \\
&= \frac{T}{2} \sum_n \int \frac{d\mathbf{k}}{(2\pi)^2} \left[\ln[\Delta_n - \rho^D \kappa_n \bar{t}_n e^{-2\kappa_n a}) - \ln(\Delta_n) \right] \\
&= \frac{T}{2} \sum_n \int \frac{d\mathbf{k}}{(2\pi)^2} \left[\ln(1 - (1 + \rho^D \kappa_n) \bar{t}_n e^{-2\kappa_n a}) - \ln(\Delta_n) \right] \\
&= \frac{T}{2} \sum_n \int \frac{d\mathbf{k}}{(2\pi)^2} \left[\ln(1 - t^D_{\text{rough}}(\kappa_n) \bar{t}_n e^{-2\kappa_n a^D_{\text{eff}}}) - \ln(\Delta_n) \right]
\end{aligned} \tag{3.61}$$

The one-loop free energy depends on the mean plate separation a and on the length $\rho^D = -v_{01} \sim \sqrt{2\pi}\sigma^2/\ell$ that characterizes the profile. The effective separation of the two plates, $a^D_{\text{eff}} = a - \rho^D/2$, in one-hard-loop approximation coincides with the one found perturbatively in Eq.(3.53). We in addition obtain the reduced

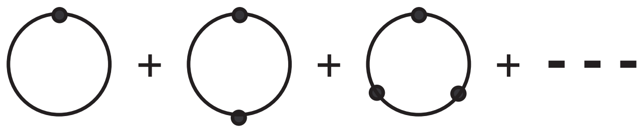

Figure 3.7: One (s)low loop contributions to the free energy in the effective model for a rough plate. Lines correspond to (s)low propagators and dots represent effective local 2-point vertices.

scattering matrix t^D_{rough} for low-energy scattering off a rough Dirichlet plate,

$$t^D_{\mathrm{rough}}(\kappa) = (1 + \rho^D \kappa) e^{-\rho^D \kappa} \ . \tag{3.62}$$

$t^D_{\mathrm{rough}}(\kappa)$ is positive and never exceeds unity. It satisfies all the requirements of a reduced scattering matrix and is consistent with phenomenology for scattering off a rough plate in that only short wavelengths with $\kappa\rho^D \gg 1$ are strongly affected. $t^D_{\mathrm{rough}}(\kappa) < 1$ is due to diffuse scattering of part of the incident wave with (transverse) wave vector $\mathbf{k}$. The intensity of the outgoing wave with (transverse) wave-vector $\mathbf{k}$ is thereby reduced. Diffuse scattering by a rough surface is more effective at shorter wavelengths and negligible for wavelengths that are long compared to $\rho^D \sim \sigma^2/\ell$. Note that the scattering matrix found in this approximation does not depend on the separation a of the two plates (as the $GTGT$-formula[22] indeed requires). However, the approximations in deriving the low energy effective theory are justified only for $a \gg \ell$.

3.5.2 A rough semitransparent plate: $a \gg \ell \ll 1/\lambda$

This limit includes that of weak coupling. We proceed similarly as for the Dirichlet case but ℓ now is the smallest correlation length. The leading behavior of a local vertex thus is determined by its degree of divergence as the 'cutoff' ℓ on hard loop momenta is removed. In the limit of large transverse momenta we have that $g_{00}^{(f)} \sim 1/k, g_{11}^{(f)} \sim -k/2$. Neither depends on λ and a local vertex in this case is proportional to λ^{N_V}, where N_V is the total number of primitive vertices it is composed of. Eqs. (3.57) and (3.54) then imply that for vanishing external momenta,

$$v_{N\tilde{N}}^{(\#L)} \propto \frac{\lambda^{2N}}{\ell^2}(\ell\sigma^2)^{\tilde{N}+N}(\lambda\ell)^{N_V-2N}\left(\frac{\sigma^2}{\ell^2}\right)^{\#L-1}(1+\mathcal{O}(\lambda\ell)) \ . \tag{3.63}$$

The implication of Eq.(3.63) becomes clear upon noting that for any connected diagram $N_V - 2N \geq \tilde{N} - N + 1$. At any given order in the loop expansion, the largest contribution to an effective local vertex in the present limit therefore is from diagrams with the minimal number $N_V = \tilde{N} + N + 1$ of internal vertices. Local vertices that include external $\tilde{\psi}$-fields thus are suppressed by powers of $\lambda\ell \ll 1$ compared to n-point vertices with ψ-legs only. The low energy effective model for $a \gg \ell \ll 1/\lambda$ thus is described by a scalar with propagator $g_{00}^{(s)}$ and local v_{N0} vertices only. To first order in the loop expansion one again obtains the vertices of Eqs. (3.60b) and (3.60e),

$$v_{10} = -\lambda^2\ell^2\sigma^2\int_0^\infty kdk\frac{k}{2}e^{-k^2\ell^2/2} \quad \xrightarrow[\lambda\ell\ll 1]{} \quad -\frac{\lambda^2\sigma^2}{4\ell}\sqrt{2\pi}\delta_{nn'} \tag{3.64a}$$

$$\begin{aligned} v_{20} &= 2\pi\ell^4\sigma^4\int_0^\infty kdk2\left(\frac{\lambda^2 k}{2}\right)^2 e^{-k^2\ell^2} \\ &\xrightarrow[\lambda\ell\ll 1]{} \quad \frac{\pi\lambda^4\sigma^4}{2}(\delta_{nn'}\delta_{mm'}+\delta_{nm'}\delta_{mn'}+\delta_{n'm'}\delta_{nm}) \end{aligned} \tag{3.64b}$$

but the local effective interactions v_{01}, v_{11} and v_{02} become negligible. To one (s)oft loop, the roughness and separation-dependent correction $\Delta f^{(2)}$ to the free energy per unit area in the limit $a \gg \ell \ll 1/\lambda$ is,

$$\begin{aligned}\Delta f^{(2)}_{\text{1-loop}}(\rho; a \gg \ell \ll 1/\lambda) = -T\sum_n \int \frac{d\mathbf{k}}{(2\pi)^2}\sum_{k=1}^{\infty}\frac{1}{2k}\left(\rho\frac{\kappa_n t_n \bar{t}_n e^{-2\kappa_n a}}{\Delta_n}\right)^k \\ =\frac{T}{2}\sum_n \int \frac{d\mathbf{k}}{(2\pi)^2}\left[\ln(\Delta_n - \rho\kappa_n t_n \bar{t}_n e^{-2\kappa_n a}) - \ln(\Delta_n)\right] \\ =\frac{T}{2}\sum_n \int \frac{d\mathbf{k}}{(2\pi)^2}\left[\ln(1-(1+\rho\kappa_n)t_n \bar{t}_n e^{-2\kappa_n a}) - \ln(\Delta_n)\right] \\ =\frac{T}{2}\sum_n \int \frac{d\mathbf{k}}{(2\pi)^2}\left[\ln(1-t_{\text{rough}}(\kappa_n)\bar{t}_n e^{-2\kappa_n a_{\text{eff}}}) - \ln(\Delta_n)\right]\end{aligned} \tag{3.65}$$

with

$$t_{\text{rough}}(\kappa) = (1+\kappa\rho)t(\kappa)e^{-\kappa\rho} \le t(\kappa) \text{ and } a_{\text{eff}} = a - \rho/2\ . \tag{3.66}$$

One reproduces the Dirichlet boundary condition result of Eq.(3.62) by simply letting $t \to t^D = 1$ and $\rho \to \rho^D$ in Eq.(3.66). However, for a similar profile the parameter ρ is only half that found in the Dirichlet limit,

$$\rho = \frac{\sigma^2}{\ell}\sqrt{\frac{\pi}{2}} = \rho^D/2\ . \tag{3.67}$$

The displacement of the equivalent surface of the rough plate from the mean of the profile by ρ evidently also depends on the transparency of the plate. Considering the effective shift $\rho(\lambda)$ as a phenomenological parameter of the rough plate, the main effect due to roughness in the limit $a \gg \ell$ is to define the position of the effective planar scattering surface and simultaneously modify the scattering matrix of a flat plate as in Eq.(3.66). It is interesting that the two effects are not independent. The two extreme limits we have considered provide a range for the parameter $\rho(\lambda)$ in terms of the variance and correlation length of a profile described by Eq.(3.23d),

$$\sqrt{\frac{\pi}{2}}\frac{\sigma^2}{\ell} \le \rho(\lambda) \le \sqrt{2\pi}\frac{\sigma^2}{\ell}\ . \tag{3.68}$$

The upper bound of Eq.(4.74) corresponds to a rough surface with Dirichlet boundary conditions and the lower to weak coupling. Note that the effective scattering plane does not coincide with the mean of the profile even for weak coupling $\lambda \sim 0$ [although the scattering matrix is arbitrary small].

Chapter 4

Perturbative electromagnetic roughness corrections

4.1 The Model

In this chapter, we extend our scalar model of semitransparent plates to the electromagnetic case with real materials. We start by considering the QED action without any net charge and current,

$$S = \int \Big(-\frac{1}{4} F_{\mu\nu} F^{\mu\nu} \Big) d^4x \tag{4.1}$$

where $F_{\mu\nu} = \partial_\mu A_\nu - \partial_\nu A_\mu$ is the electromagnetic field tensor described by the covariant four-potential A_μ. The homogenous Maxwell's equations are obtained using the least action principle for the action of Eq.(4.1),

$$\partial_\mu F^{\mu\nu} = 0 \tag{4.2}$$

We now defind the **E** and **B** fields as,

$$E^i = -F^{0i}, \qquad \varepsilon^{ijk} B_k = -F^{ij} \tag{4.3}$$

The gauge-invariance of the local action of Eq.(4.1) implies the **E** and **B** fields can be expressed in terms of a scalar potential ϕ and **A** through the relation:

$$\mathbf{E} = -\nabla\phi - \frac{\partial \mathbf{A}}{\partial t}, \quad \mathbf{B} = \nabla \times \mathbf{A} \tag{4.4}$$

For simplication we here choose the Weyl's gauge, $\phi = 0$ for the following analysis and express the **E** and **B** fields in terms of the vector potential only,

$$\mathbf{E} = -\frac{\partial \mathbf{A}}{\partial t}, \quad \mathbf{B} = \nabla \times \mathbf{A} \tag{4.5}$$

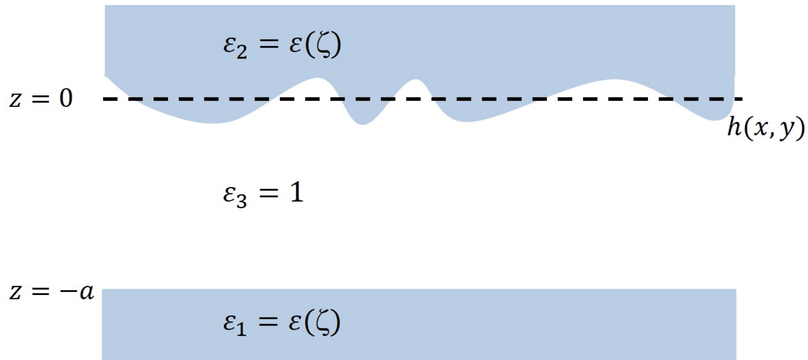

Figure 4.1: Two semi-infinite slabs of the same material separated by vacuum. The low-energy electromagnetic properties of the material are described by a bulk-permittivity $\varepsilon(\omega)$ that only depends on the frequency of the electric field. In Cartesian coordinates the planar interface is at $z = -a$ and the mean separation of the two interfaces is a. The surface of the rough slab is at $z = h(\mathbf{x})$ where $h(\mathbf{x})$ is a profile function that generally depends on both transverse coordinates $\mathbf{x} = (x, y)$. We develop a perturbative expansion valid for $|h(\mathbf{x})| \ll a$ with no restrictions on the profile other than that it be single-valued. $h(\mathbf{x})$ in particular need not be as smooth as shown here.

The QED action of Eq.(4.1) describes the electromagnetic field's propagation in the vaccum. However, when the electromagnetic field interacts with real materials, different low-energy effective models are often used to describe the systems at low energies. We here consider the configuration shown in Fig. 4.1 of two dielectric (metallic) slabs of the same material at an average separation a that is much less than their transverse dimension and only one of which is rough with permittivities,

$$\varepsilon_3 = 1 \; , \quad \varepsilon_2 = \varepsilon = \varepsilon_1 \; . \tag{4.6}$$

and use the Schwinger's low-energy effective field theory [25] for electromagnetism. The action in this model is a functional of of the local electric permittivity tensor ε_i of the medium and of an external polarization source $\mathbf{P}$,

$$S = \int d^4x \Big[(-\nabla\phi - \frac{\partial \mathbf{A}}{\partial t})\cdot\varepsilon\mathbf{E}\cdot - \mathbf{H}\cdot(\nabla\times\mathbf{A}) - \frac{1}{2}E^2 + \frac{1}{2}H^2 + (-\nabla\phi - \frac{\partial \mathbf{A}}{\partial t})\cdot\mathbf{P}\Big] \tag{4.7}$$

Substituting Eq.(4.5) into Eq.(4.7) and using the Weyl's gauge, the action can be simplified to,

$$\begin{aligned} S &= \int dt \int d^3x \Big(\frac{1}{2}(\mathbf{E} \cdot \mathbf{D} - \mathbf{B} \cdot \mathbf{H}) + \mathbf{E} \cdot \mathbf{P} \Big) \\ &= S_E + S_B + \int dt \int d^3x \mathbf{E} \cdot \mathbf{P} \end{aligned} \tag{4.8}$$

In this thesis, I focus on homogeneous and non-magnetic materials whose permittivity tensor ε is diagonal and $\mu = 1$. The electric displacement field $\mathbf{D}$ depends on the response of dielectric medium to the external $\mathbf{E}$ field.

$$\mathbf{D}(\mathbf{x}, z; t) = \int_{-\infty}^{\infty} \frac{d\omega}{2\pi} \varepsilon(\mathbf{x}, z; \omega) \mathbf{E}(\mathbf{x}, z; \omega) e^{-i\omega t} \tag{4.9}$$

We proceed by mapping the electromagnetic fields in Eq.(4.8) to the frequency domain. The electric and magnetic part of Eq.(4.8) then can be written as,

$$\begin{aligned} S_E &= \frac{1}{2} \int dt \int d^3x \mathbf{E} \cdot \mathbf{D} \\ &= \frac{1}{2} \int dt \int d^3x \int \frac{d\omega'}{2\pi} e^{-i\omega' t} \mathbf{E} \cdot \int \frac{d\omega}{2\pi} e^{-i\omega t} \varepsilon(\mathbf{x}, z; \omega) \mathbf{E}(\mathbf{x}, z; \omega) \\ &= \frac{1}{2} \int d^3x \int \frac{dw}{2\pi} \mathbf{E}(-\omega) \cdot \varepsilon(\mathbf{x}, z; \omega) \mathbf{E}(\omega) \end{aligned} \tag{4.10}$$

For the non-magnetic, $\mu = 1$, medium,

$$\begin{aligned} S_B &= -\frac{1}{2} \int dt \int d^3x \mathbf{B} \cdot \mathbf{H} \\ &= -\frac{1}{2} \int d^3x \int dt \int \frac{d\omega}{2\pi} (\nabla \times \mathbf{A}(\omega)) e^{-i\omega t} \cdot \int \frac{d\omega'}{2\pi} (\nabla \times \mathbf{A}(\omega')) e^{-i\omega' t} \\ &= -\frac{1}{2} \int d^3x \int \frac{d\omega}{2\pi} \mathbf{A}(\omega) \cdot \nabla \times \nabla \times \mathbf{A}(-\omega) \end{aligned} \tag{4.11}$$

We combine Eq.(4.10) and Eq.(4.11) and perform Wick rotation on the frequency $\omega \to i\zeta$. In Weyl gauge the partition function of the system then is given by the functional integral,

$$Z[\mathbf{P}] = \int D[\mathbf{E}_\zeta] exp\Big\{ -\frac{1}{2} \int \frac{d\zeta}{2\pi} \int d^3x \mathbf{E}^\dagger_\zeta(\vec{x}) [\varepsilon_\zeta(\vec{x}) + \frac{1}{\zeta^2} \nabla \times \nabla \times] \mathbf{E}_\zeta(\vec{x}) + \mathbf{E}_\zeta \cdot \mathbf{P}_\zeta \Big\} \tag{4.12}$$

The dielectric function $\varepsilon_\zeta(\vec{x})$ depends on position because two plates separated by vacuum is not a homogeneous medium. The rough interface is assumed to be without enclosures and the deviation from a flat one at $z = 0$ is described by a single-valued function $h(\mathbf{x})$ that satisfies[1],

$$\langle h \rangle := \frac{1}{A} \int_A d\mathbf{x}\, h(\mathbf{x}) = 0. \tag{4.13}$$

When the cross-sectional area A of the slab is taken large, finite size effects can be ignored and the n-point correlation function,

$$D_n(\mathbf{x} - \mathbf{y}) = \langle h(\mathbf{x}_1) h(\mathbf{x}_2) \ldots h(\mathbf{x}_n) \rangle := A^{-1} \int_A d\mathbf{r}\, h(\mathbf{r} + \mathbf{x}_1) \ldots h(\mathbf{r} + \mathbf{x}_n) \tag{4.14}$$

is invariant under transverse translations.

4.2 Counter terms

The dielectric permittivity function $\varepsilon(\zeta, x_i)$ in this effective low-energy field theory is of the form,

$$\begin{aligned} \varepsilon(\zeta, \vec{x}) &= \mathbb{1}[\varepsilon_3(\zeta) + (\varepsilon_2(\zeta) - \varepsilon_3(\zeta))\theta(z - h(\mathbf{x})) + (\varepsilon_1(\zeta) - \varepsilon_3(\zeta))\theta(-z - a)] + \delta \mathbf{V}^h \\ &= \mathbf{V}^{\parallel}(\zeta, z) + \mathbf{V}^h(\zeta, \mathbf{x}, z) \ , \end{aligned} \tag{4.15}$$

where

$$\mathbf{V}^h(\zeta, \mathbf{x}, z) = \mathbb{1}[(\varepsilon_2(\zeta) - \varepsilon_3(\zeta))(\theta(z - h(\mathbf{x})) - \theta(z))] \tag{4.16}$$

is the deviation due to the roughness profile $h(\mathbf{x})$ from the dielectric permittivity of a transversely homogeneous medium given by,

$$\mathbf{V}^{\parallel}(\zeta, z) = \mathbb{1}[\varepsilon_3(\zeta) + (\varepsilon_2(\zeta) - \varepsilon_3(\zeta))\theta(z) + (\varepsilon_1(\zeta) - \varepsilon_3(\zeta))\theta(-z - a)] + \delta \mathbf{V}^h(\zeta, z) \tag{4.17}$$

[1] A Cartesian coordinate system with z-axis normal to the plates is used to describe this system. We use bold type $\mathbf{x} = (x, y)$ for 2-dimensional vectors perpendicular to the z-axis, whereas $\vec{v}$ denotes an ordinary 3-dimensional vector.

We shall argue that the counter term $\delta\mathbf{V}^h(\zeta, z)$ to the dielectric permittivity of three flat slabs is necessary for a consistent perturbative expansion in the framework of this low-energy theory. It incorporates all the high energy contributions which are not correctly described by the effective low-energy action Eq.(4.12). This counter term in general would have to be determined phenomenologically. $\delta\mathbf{V}^h(\zeta, z)$ may depend on gross properties of the profile $h(\mathbf{x})$ but not on the transverse position $\mathbf{x}$ nor on the separation of the two interfaces. This counter term ensures that the single-interface scattering matrix is reproduced by the low-energy effective theory. To leading order $\delta\mathbf{V}^h(\zeta, z)$ is proportional to the variance σ^2 of the rough interface. We are thus calculating the perturbative expansion for the rough interface at $z = 0$ about an effective $\mathbf{x}$-independent (bare) permittivity,

$$\varepsilon_{\text{eff}}(\zeta, z) = \mathbb{1}\varepsilon_2(\zeta)\theta(z) + \mathbb{1}\varepsilon_3(\zeta)\theta(-z) + \delta\mathbf{V}^h(\zeta, z)\ . \tag{4.18}$$

$\delta\mathbf{V}^h(\zeta, z)$ has support near the surface at $z \sim 0$ only[2]. To approximate scattering off a rough interface by an effective $\varepsilon_{\text{eff}}(\zeta, z)$ is conceptually appealing and not a new idea [79, 80]. We here develop a consistent low-energy approach in which this approach is realized perturbatively. Contrary to commonly used ansätze for the effective ε_{eff}, $\delta\mathbf{V}^h(\zeta, z)$ will be found to be not isotropic.

The inherent limitations of the effective low-energy description are not restricted to a perturbative analysis and derive from the fact that electromagnetic interaction with matter is encoded in the permittivity function. The dimensionless permittivity function $\varepsilon(\zeta) = \varepsilon(\zeta/\omega_P)$ implicitly depends on an energy scale that can be identified with the plasma frequency ω_P of the material. At momentum- or energy-transfers (or temperatures) much larger than ω_P the effective low-energy theory of Eq.(4.12) fails to incorporate non-linear effects and

[2]To first order in the variance we find in Eq.(4.57) of that $\delta\mathbf{V}^h(\zeta, z) \propto \delta(z)$, that is $\varepsilon_{\text{eff}}(\zeta, z)$ differs from that of an interface by the insertion of an arbitrary thin plate.

to account for the creation of free charges. The assumption that the permittivity does not depend on the profile furthermore become incorrect for surface structures with wavelengths comparable to the plasma wavelength $l_p = 2\pi/\omega_P$: the description in terms of the bulk permittivity of the homogeneous material is not warranted within the plasma skin depth of order l_p. For gold surfaces $\omega_P \sim 0.046\text{nm}^{-1} \sim 9\text{eV}$ and $l_p \sim 140\text{nm}$. The low-energy description of electromagnetic interactions with such materials by Eq.(4.15) therefore becomes questionable at wave numbers $q \gg \omega_P \sim 0.046\text{nm}^{-1}$ that resolve less than 140nm or about 200 gold atoms. We will see that roughness corrections to the Casimir force with correlations lengths $l_c \lesssim 1/\omega_P$ depend on momentum transfers $q \gg \omega_P$ which the low-energy theory describes inadequately. The conservative approach is to use the effective low-energy theory to only compute roughness corrections with $l_c \gg 1/\omega_P \sim 20\text{nm}$, a regime where the proximity force approximation generally is quite accurate. We improve on this restriction by introducing phenomenological input.

4.3 The Green's function approach

Schwinger [25] obtained the Casimir free energy and the response to an external polarization source $\vec{P}(\mathbf{x}, z) = \vec{P}(\mathbf{x}, z; \zeta)$ for three parallel slabs in the framework of the low energy effective field theory. To includes the temperature effect, one replaces the ζ integral by a sum over Matsubara frequencies,

$$\begin{aligned} Z_T[\vec{P}; \varepsilon] &= \prod_n \int D[\mathbf{E}_n] \exp\Big\{ -\frac{1}{2T} \int d^3x \mathbf{E}_n^\dagger(\vec{x})[\varepsilon(\zeta_n, \vec{x}) + \frac{1}{\zeta_n^2} \nabla \times \nabla \times] \mathbf{E}_n(\vec{x}) \\ &+ 2T \mathbf{E}_n(\vec{x}) \cdot \mathbf{P}_n(\vec{x}) \Big\} \end{aligned} \tag{4.19}$$

The free energy in this case is [25],

$$\mathcal{F}_T^{\|}(a, \vec{P}) = F_T^{\|}(a) - \frac{T^2}{2} \sum_n \{ \vec{P}_n | \mathbf{G}^{\|(n)} | \vec{P}_n \} \ . \tag{4.20}$$

Here $F_T^{\|}$ is the well-known Lifshitz's formula Eq.(1.15) for three parallel slabs at finite temperature,

$$F_T^{\|}(a) = \frac{AT}{2}\sum_n \int \frac{d\mathbf{k}}{(2\pi)^2}[\ln(1 - r_1 r_2 e^{-2\kappa_3 a}) + \ln(1 - \bar{r}_1\bar{r}_2 e^{-2\kappa_3 a})] \ , \tag{4.21}$$

where the reflection coefficients at the i-th interface of area A for the TE- and TM-modes are,

$$\begin{aligned} r_i = r_i^{TE} = \frac{\kappa_3 - \kappa_i}{\kappa_3 + \kappa_i} \ \text{ and } \ \bar{r}_i = r_i^{TM} = \frac{\bar{\kappa}_3 - \bar{\kappa}_i}{\bar{\kappa}_3 + \bar{\kappa}_i} \\ \text{with } \ \kappa_i = \sqrt{\mathbf{k}^2 + \zeta_n^2 \varepsilon_i(\zeta_n)} \ \text{ and } \ \bar{\kappa}_i = \frac{\kappa_i}{\varepsilon_i(\zeta_n)} \ . \end{aligned} \tag{4.22}$$

The response due to the n-th Matsubara mode to an external source of polarization is,

$$\{\vec{P}_n|\mathbf{G}^{\|(n)}|\vec{P}_n\} = \int dz dz' d\mathbf{x} d\mathbf{y} \vec{P}_n^\dagger(\mathbf{x}, z)\cdot \mathbf{G}^{\|}(\mathbf{x}, z, \mathbf{y}, z'; \zeta_n, a)\cdot \vec{P}_n(\mathbf{y}, z) \tag{4.23a}$$

$$= \int \frac{d\mathbf{k}}{(2\pi)^2} dz dz' \vec{P}_n^\dagger(\mathbf{k}, z)\cdot \mathbf{G}^{\|}(\mathbf{k}, z, z'; \zeta_n, a)\cdot \vec{P}_n(\mathbf{k}, z) \ . \tag{4.23b}$$

$\mathbf{G}^{\|}$ in Eq.(4.23a) is the Green's dyadic solving[3],

$$\left[\mathbf{V}^{\|}(\zeta_n, z) - \delta\mathbf{V}^h(\zeta_n, z) + \frac{1}{\zeta_n^2}\nabla\times\nabla\times\right]\mathbf{G}^{\|}(\mathbf{x}, z, \mathbf{y}, z'; \zeta_n, a) = \mathbb{1}\delta(z - z')\delta(\mathbf{x} - \mathbf{y}) \ . \tag{4.24}$$

Due to translational invariance in transverse directions, $\mathbf{G}^{\|}(\mathbf{x}, z, \mathbf{y}, z'; \zeta_n, a)$ is a function of $\mathbf{x} - \mathbf{y}$ and the Fourier-representations in Eq.(4.23b) are,

$$\begin{aligned} \mathbf{G}^{\|}(\mathbf{x}, z, \mathbf{y}, z'; \zeta_n, a) &= \int \frac{d\mathbf{k}}{(2\pi)^2} e^{i\mathbf{k}(\mathbf{x}-\mathbf{y})}\mathbf{G}^{\|}(\mathbf{k}, z, z'; \zeta_n, a) \\ \vec{P}_n(\mathbf{k}, z) &= \int d\mathbf{x}\, e^{-i\mathbf{k}\mathbf{x}}\vec{P}_n(\mathbf{x}, z) \ . \end{aligned} \tag{4.25}$$

$\mathbf{G}^{\|}$ can be decomposed into a single-interface Green's dyadic $\mathbf{G}^{|}(\mathbf{x}-\mathbf{y}, z, z'; \zeta_n) = \mathbf{G}^{\|}(\mathbf{x}, z, \mathbf{y}, z'; \zeta_n, a \to \infty)$ where the second interface has been removed and the correction $\mathbf{G}^{|a|}(\mathbf{x} - \mathbf{y}, z, z'; \zeta_n, a)$ due to the presence of a second flat interface

[3] $\mathbf{G}^{\|}(\zeta)$ is related to Schwinger's[25] dyadic $\mathbf{\Gamma}(\omega)$ at angular frequency ω by $\mathbf{G}^{\|}(\zeta) = -\mathbf{\Gamma}(i\omega)$.

at mean separation a. In momentum space the latter vanishes exponentially for $a \to \infty$,

$$\mathbf{G}^{||}(\mathbf{k}, z, z'; \zeta_n, a) = \mathbf{G}^{|}(\mathbf{k}, z, z'; \zeta_n) + \mathbf{G}^{|a|}(\mathbf{k}, z, z'; \zeta_n) \ . \tag{4.26}$$

Explicit expressions for components of $\mathbf{G}^{|}(\mathbf{k}, z, z'; \zeta_n)$ and $\mathbf{G}^{|a|}(\mathbf{k}, z, z'; \zeta_n)$ when z and z' are in slab #2 or slab #3 are collected in B.1.

4.3.1 Perturbation in the roughness profile

We now construct the perturbation theory in the surface roughness based on the Green's function formalism. A straightforward perturbative expansion in the roughness potential $\mathbf{V}^h$ is possible only for media with $\varepsilon_2 - \varepsilon_3 \ll 1$. Since the Casimir free energy itself is rather small, roughness corrections would be all but negligible in this weak coupling scenario. However, the support of $\mathbf{V}^h$ is restricted to $|z| \leq \max_{\mathbf{x}} |h(\mathbf{x})| \sim \sigma \ll a$ and a perturbative expansion in σ/a exists even for media whose permittivity is rather large. This expansion in fact is possible even for ideal metals.

Let us consider the Casimir free energy for two interfaces separated by an average distance a. In terms of the Greens-dyadic $\mathbf{G}^{||}$ of parallel flat slabs satisfying Eq.(4.24), the full Greens function $\mathbf{G}$ when one of the surfaces is rough is given by (see Eq.(2.11)),

$$\left[\mathbb{1} + \mathbf{V}\mathbf{G}^{||}\right]\mathbf{G}^{||-1}\mathbf{G} = \mathbb{1} \ , \tag{4.27}$$

with,

$$\mathbf{V} = \mathbf{V}^h + \delta\mathbf{V}^h = \mathbb{1}(\varepsilon(\zeta) - 1)(\theta(z - h(\mathbf{x})) - \theta(z)) + \delta\mathbf{V}^h(\zeta, z) \ . \tag{4.28}$$

As was shown in Eq.(2.10), the change in the free energy due to roughness of one interface then is [81, 20],

$$\Delta F_T[h, a] = -\tfrac{1}{2}\mathrm{Tr}\ln(\mathbf{G}^{||-1}\mathbf{G}) = \tfrac{1}{2}\mathrm{Tr}\ln(\mathbb{1} + \mathbf{V}\mathbf{G}^{||}) \ , \tag{4.29}$$

where the trace includes a summation over Matsubara frequencies and over a complete set of scattering states. The expression in Eq.(4.29) still is rather formal because it includes the change in free energy due to roughness in the absence of the second (flat) interface. This infinite single-body contribution to the free energy does not depend on the mean separation a. Subtracting from $\Delta F_T[h,a]$ its value when the two interfaces are infinitely far apart gives the correction to the Casimir free (interaction) energy due to roughness of an interface as,

$$\begin{aligned}\Delta F_T^{\mathrm{Cas}}[h,a] &:= \Delta F_T[h,a] - \Delta F_T[h,\infty] = \frac{1}{2}\mathrm{Tr}\ln(\mathbb{1}+\mathbf{V}\mathbf{G}^{\|}) - \frac{1}{2}\mathrm{Tr}\ln(\mathbb{1}+\mathbf{V}\mathbf{G}^{|}) \\ &= \frac{1}{2}\mathrm{Tr}\ln(\mathbb{1}+\mathbf{T}^h\mathbf{G}^{|a|})\ , \end{aligned} \tag{4.30}$$

where

$$\mathbf{T}^h = \mathbf{V} - \mathbf{V}\mathbf{G}^{|}\mathbf{T}^h \tag{4.31}$$

is the single-plate scattering matrix due to the roughness potential $\mathbf{V}$. $\mathbf{T}^h$ does not depend on the separation a and describes scattering due to roughness in the *absence* of the second (flat) interface. Since high momenta are exponentially suppressed in $\mathbf{G}^{|a|}$, the Volterra series of $\Delta F_T^{\mathrm{Cas}}[h,a]$ in powers of $\mathbf{T}^h$,

$$\begin{aligned}\Delta F_T^{\mathrm{Cas}}[h,a] &= \tfrac{1}{2}\mathrm{Tr}\ln(\mathbb{1}+\mathbf{T}^h\mathbf{G}^{|a|}) \\ &\sim \tfrac{1}{2}\mathrm{Tr}\Big[\mathbf{T}^h\mathbf{G}^{|a|} - \tfrac{1}{2}\mathbf{T}^h\mathbf{G}^{|a|}\mathbf{T}^h\mathbf{G}^{|a|} + \ldots \end{aligned} \tag{4.32}$$

converges when the norm of $\mathbf{T}^h$ is finite.

4.3.2 The Roughness scattering matrix $\mathbf{T}^h$

The well known solution of the Green's function Eq.(4.24) for three parallel slabs was obtained by Schwinger [25],

$$\mathbf{G}^{\|}(k,z,z';\zeta,a) = \begin{bmatrix} -\frac{1}{\varepsilon_z}\frac{\partial}{\partial z}\frac{1}{\varepsilon_{z'}}\frac{\partial}{\partial z'}g_H & 0 & -\frac{ik}{\varepsilon_z\varepsilon_{z'}}\frac{\partial}{\partial z}g_H \\ 0 & \zeta^2 g_E & 0 \\ \frac{ik}{\varepsilon_z\varepsilon_{z'}}\frac{\partial}{\partial z'}g_H & 0 & \frac{1}{\varepsilon_z}\delta(z-z') - \frac{k^2}{\varepsilon_z\varepsilon_{z'}}g_H \end{bmatrix} \tag{4.33}$$

where the reduced Green's function g_E and g_H solve the differential equations,

$$\Big[-\frac{\partial^2}{\partial z^2}+k^2+\zeta^2\varepsilon_z\Big]g_E(k,z,z';\zeta)=\delta(z-z') \tag{4.34}$$
$$\Big[-\frac{\partial}{\partial z}\frac{1}{\varepsilon_z}\frac{\partial}{\partial z}+\frac{k^2}{\varepsilon_z}+\zeta^2\Big]g_H(k,z,z';\zeta)=\delta(z-z')$$

and are explicitly given in Eq.(B.5). Noting that the component $G^{|}_{zz}(\mathbf{k},z,\mathbf{y},z';\zeta)$ in Eq.(4.33) includes a δ-function contribution, Eq.(4.31) can be rewritten,

$$\mathbf{T}^h=\tilde{\mathbf{V}}-\tilde{\mathbf{V}}\tilde{\mathbf{G}}^{|}\mathbf{T}^h\ , \tag{4.35}$$

in terms of the Green's dyadic $\tilde{\mathbf{G}}^{|}$ with Fourier components,

$$\tilde{\mathbf{G}}^{|}(\mathbf{k},z,z';\zeta)=\mathbf{G}^{|}(\mathbf{k},z,z';\zeta)-\mathrm{diag}(0,0,\frac{1}{\varepsilon_z}\delta(z-z'))\ , \tag{4.36}$$

and a new potential $\tilde{\mathbf{V}}$. $\tilde{\mathbf{G}}$ is devoid of δ-function singularities (but not continuous at $z=0$) with components given in Eq.(B.6). To order σ^2 the potential $\tilde{\mathbf{V}}$ is,

$$\begin{aligned}\tilde{\mathbf{V}}(\mathbf{x},z;\zeta) &= \tilde{\mathbf{V}}^h(\zeta,\mathbf{x},z)+\delta\tilde{\mathbf{V}}^h(\zeta,z) \\ &= (\varepsilon-1)[\theta(z-h(\mathbf{x}))-\theta(z)]\,\mathrm{diag}[1,1,\varepsilon\,\theta(z)+\theta(-z)/\varepsilon]+\delta\tilde{\mathbf{V}}^h(\zeta,z)\end{aligned} \tag{4.37}$$

The reformulation of Eq.(4.31) in the form of Eq.(4.35) resums local contributions of the same order in h. It allows the formulations of a consistent perturbative expansion in σ even in the ideal metal limit $\varepsilon(\zeta)\to\infty$. Just as for $\mathbf{V}$, the support of $\tilde{\mathbf{V}}$ is restricted to the interval $|z|<\max_{\mathbf{x}}|h(\mathbf{x})|\sim\sigma$ only. Since $\tilde{\mathbf{G}}^{|}$ is free of ultra-local δ-function singularities, contributions to $\mathbf{T}^h$ of n-th order in $\tilde{\mathbf{V}}$ are at least of n-th order in the standard deviation σ of the profile $h(\mathbf{x})$.

To second order in σ we need only consider the first two terms of the Volterra series,

$$\mathbf{T}^h\approx\tilde{\mathbf{V}}-\tilde{\mathbf{V}}\tilde{\mathbf{G}}^{|}\tilde{\mathbf{V}}\approx\tilde{\mathbf{V}}-\tilde{\mathbf{V}}^h\tilde{\mathbf{G}}^{|}\tilde{\mathbf{V}}^h=\mathbf{T}^{(1)}+\mathbf{T}^{(2)}\ , \tag{4.38}$$

since the counterterm potential $\delta\tilde{\mathbf{V}}^h$ is itself of order σ^2 (as will be seen). The second-order contribution $\mathbf{T}^{(2)}$ of Eq.(4.38) is at least of order σ^2 and its integrated expectation to this order is,

$$\begin{aligned}\mathbf{t}^{(2)}(\mathbf{x}-\mathbf{y},\zeta) &:= \langle\int dz\,dz'\,\mathbf{T}^{(2)}(\mathbf{x},z,\mathbf{y},z';\zeta)\rangle \\ &= -\langle\int dz\,dz'\,\tilde{\mathbf{V}}^h(\mathbf{x},z;\zeta)\tilde{\mathbf{G}}^{|}(\mathbf{x}-\mathbf{y},z,z';\zeta)\tilde{\mathbf{V}}^h(\mathbf{y},z';\zeta)\rangle + \mathcal{O}(\sigma^3)\end{aligned} \tag{4.39}$$

Because $\int dz\tilde{\mathbf{V}}^h(\mathbf{x},z,\zeta)$ already is of order σ, the Fourier components of $\mathbf{t}^{(2)}$ are[4],

$$\begin{aligned}
t^{(2)}_{xx}(k,\zeta) &= -(\varepsilon-1)^2\int\frac{d\mathbf{k}'}{(2\pi)^2}\left(\frac{\kappa'\kappa'_\varepsilon\cos^2\theta}{\kappa'_\varepsilon+\varepsilon\kappa'}+\frac{\zeta^2\sin^2\theta}{\kappa'_\varepsilon+\kappa'}\right)D(q)+\mathcal{O}(\sigma^3)\\
t^{(2)}_{yy}(k,\zeta) &= -(\varepsilon-1)^2\int\frac{d\mathbf{k}'}{(2\pi)^2}\left(\frac{\kappa'\kappa'_\varepsilon\sin^2\theta}{\kappa'_\varepsilon+\varepsilon\kappa'}+\frac{\zeta^2\cos^2\theta}{\kappa'_\varepsilon+\kappa'}\right)D(q)+\mathcal{O}(\sigma^3)\\
t^{(2)}_{zz}(k,\zeta) &= -(\varepsilon-1)^2\int\frac{d\mathbf{k}'}{(2\pi)^2}\frac{-k'^2}{\varepsilon\kappa'+\kappa'_\varepsilon}\\
&\times\ (\varepsilon D_{++}(q)+D_{-+}(q)+D_{+-}(q)+\frac{1}{\varepsilon}D_{--}(q))+\mathcal{O}(\sigma^3)\\
t^{(2)}_{xz}(k,\zeta) &= -(\varepsilon-1)^2\int\frac{d\mathbf{k}'}{(2\pi)^2}\frac{ik'\cos\theta}{\kappa'_\varepsilon+\varepsilon\kappa'}\\
&\times\ (\kappa'_\varepsilon D_{++}(q)+\bar{\kappa}'_\varepsilon D_{+-}(q)-\varepsilon\kappa' D_{-+}(q)-\kappa' D_{--}(q))+\mathcal{O}(\sigma^3)\\
t^{(2)}_{zx}(k,\zeta) &= -(\varepsilon-1)^2\int\frac{d\mathbf{k}'}{(2\pi)^2}\frac{-ik'\cos\theta}{\kappa'_\varepsilon+\varepsilon\kappa'}\\
&\times\ (\kappa'_\varepsilon D_{++}(q)-\varepsilon\kappa' D_{+-}(q)+\bar{\kappa}'_\varepsilon D_{-+}(q)-\kappa' D_{--}(q))+\mathcal{O}(\sigma^3)\ ,
\end{aligned} \tag{4.40}$$

with $q^2=(\mathbf{k}-\mathbf{k}')^2=k^2+k'^2-2kk'\cos\theta$. The $\tilde{G}^{|}_{zx}$ and $\tilde{G}^{|}_{zz}$ components of the dyadic (see App B.) are discontinuous at $z=0$. One therefore has to separately consider correlators of positive and negative components of the roughness profile in Eq.(4.40). With $h_\pm(\mathbf{x})=h(\mathbf{x})\theta(\pm h(\mathbf{x}))$, these signed correlators are,

$$D_{\pm+}(q)=D_{\mp-}(q):=\int d\mathbf{x}e^{i\mathbf{q}(\mathbf{x}-\mathbf{y})}\langle h_\pm(\mathbf{x})h_+(\mathbf{y})\rangle\ , \tag{4.41}$$

$$D(q)=2D_{++}(q)+2D_{+-}(q)=\int d\mathbf{x}e^{i\mathbf{q}(\mathbf{x}-\mathbf{y})}\langle h(\mathbf{x})h(\mathbf{y})\rangle\ . \tag{4.42}$$

$D(q)$ is the Fourier transform of the two-point correlation function $D_2(\mathbf{x}-\mathbf{y})$ of Eq.(2.42). As shown in App B. the signed correlators for a Gaussian generating

[4] $\mathbf{k}=(k,0,0)$ here defines the positive x-axis and (k',θ) are polar coordinates of $\mathbf{k}'$. Note that a (randomly) rough profile preserves translational (and rotational) invariance on average. The *average* scattering matrix of Eq.(4.39) therefore is diagonal in transverse momentum space.

functional of roughness correlations are related to the two-point correlator D_2 as,

$$\begin{aligned}\langle h_+(\mathbf{x})h_+(\mathbf{y})\rangle &= \langle h_-(\mathbf{x})h_-(\mathbf{y})\rangle = \frac{\sigma^2}{2\pi}(\sin\phi + (\pi-\phi)\cos\phi) \\ \langle h_+(\mathbf{x})h_-(\mathbf{y})\rangle &= \langle h_-(\mathbf{x})h_+(\mathbf{y})\rangle \\ &= \frac{\sigma^2}{2\pi}(\phi\cos\phi - \sin\phi), \quad \text{with } 0 \le \cos\phi = D_2(\mathbf{x}-\mathbf{y})/D_2(0) \le 1\end{aligned} \tag{4.43}$$

for a roughness correlation function $D_2(r)$ that is positive and monotonically decreasing with $r = |\mathbf{x}-\mathbf{y}|$. The signed correlators do not vanish and approach $\pm\sigma^2/(2\pi)$ for $r \to \infty$ if $D_2(r\sim\infty)\sim 0$. At small separations $r = |\mathbf{x}-\mathbf{y}| \ll l_c$, $\cos\phi = D_2(r)/D_2(0) \sim 1-\beta r^\alpha$. Thus $\phi \propto r^{\alpha/2}$ for $r\sim 0$ with an exponent $\alpha > 0$. The expressions of Eq.(4.43) for small ϕ then imply the behavior,

$$\begin{aligned}\langle h_+(\mathbf{x})h_+(\mathbf{y})\rangle &= \langle h_-(\mathbf{x})h_-(\mathbf{y})\rangle \sim \tfrac{1}{2}D_2(r)\ ; \\ \langle h_+(\mathbf{x})h_-(\mathbf{y})\rangle &= \langle h_-(\mathbf{x})h_+(\mathbf{y})\rangle \sim -\frac{\sigma^2}{6\pi}(2\beta r^\alpha)^{3/2} \quad \text{for } r \ll l_c\end{aligned} \tag{4.44}$$

After Fourier transformation the asymptotic behavior at large momenta $ql_c \gg 1$ of $D_{++}(q) = D_{--}(q)$ is the same as that of $\frac{1}{2}D(q \gg 1/l_c)$, whereas the mixed correlators $D_{+-}(q) = D_{-+}(q)$ fall off more rapidly.

4.3.3 The Ultraviolet (UV) Problem

For $l_c \ll 1/\omega_p$ high momentum contributions are appreciable and may even dominate the 1-loop corrections to the diagonal components of the scattering matrix in Eq.(4.40). For example,

$$\begin{aligned}t^{(2)}_{xx}(0,\zeta) &= -(\varepsilon-1)^2\int_0^\infty \frac{qdq}{4\pi}\left(\frac{\kappa\kappa_\varepsilon}{\kappa_\varepsilon+\varepsilon\kappa} + \frac{\zeta^2}{\kappa_\varepsilon+\kappa}\right)D(q) \\ &\xrightarrow{l_c\sim 0} -\frac{(\varepsilon-1)^2}{1+\varepsilon}\int_0^\infty \frac{qdq}{4\pi}qD(q)\end{aligned} \tag{4.45}$$

Whether or not loop integrals like Eq.(4.45) diverge depends on the roughness correlation function. For Gaussian roughness,

$$\langle h(\mathbf{x})h(\mathbf{y})\rangle = \sigma^2 e^{-\frac{1}{2}(\mathbf{x}-\mathbf{y})^2/l_c^2} \Rightarrow D_{\text{Gauss}}(q) = 2\pi\sigma^2 l_c^2 e^{-\frac{1}{2}q^2 l_c^2}$$
$$\text{with} \int_0^\infty \frac{qdq}{4\pi} q D_{\text{Gauss}}(q) = \frac{\sigma^2}{2l_c}\sqrt{\frac{\pi}{2}}\ , \tag{4.46}$$

or one-dimensional sinusoidal corrugation,

$$\langle h(\mathbf{x})h(\mathbf{y})\rangle = \frac{\sigma^2}{2}\cos[\frac{2\pi}{l_c}(x-y)] \Rightarrow D_{\text{Sin}}(\mathbf{q}) = 2\pi^2\sigma^2\delta(q_x - \frac{2\pi}{l_c})\delta(q_y)$$
$$\text{with}\ \frac{1}{2}\int_{-\infty}^\infty \frac{d^2q}{(2\pi)^2} q D_{\text{Sin}}(\mathbf{q}) = \frac{\sigma^2}{2l_c}\pi\ , \tag{4.47}$$

the integral converges, but the roughness "correction" becomes (arbitrary) large for $l_c \sim 0$. This invalidates the perturbative expansion in σ/a and, for sufficiently small l_c, violates unitarity. It furthermore is not physical that roughness corrections to the scattering matrix for profiles with a fixed small variance become arbitrary large as $l_c \to 0$.

For a scalar field and Gaussian roughness correlation, higher orders in the loop expansion are of the same order in σ/l_c in this limit [82]. Assuming the scalar model is valid at all energy scales, we resummed the leading σ/l_c contributions to the scalar Casimir energy in Chapter 3 and found that they amount to a change in the effective separation $\Delta a \sim \sigma^2/l_c$ of the two interfaces. However, the effective low-energy electromagnetic theory of Eq.(4.19) evidently is not valid at momenta that far exceed the plasma frequency ω_p. One therefore cannot be certain that summing incorrect higher loop contributions in this effective low energy theory would improve the situation. In the electromagnetic case we therefore will not approximately resum high-momentum contributions as in the scalar case and proceed differently.

Although the loop integrals in Eq.(4.46) and Eq.(4.47) converge with Gaussian and sinusoidal correlation functions, the finiteness of Eq.(4.45) is precarious and not guaranteed. The integral of Eq.(4.45) for instance diverges for correlation functions that correspond to machined profiles such as square-shaped corrugation of wavelength $2\pi/l_c$ and correlation function,

$$D_{\mathrm{Squ}}(\mathbf{q}) = (2\pi\sigma)^2\Big[4f^2\delta(q_x)+\sum_{n=1}^{\infty}\Big(\frac{2\sin[nf\pi]}{n\pi}\Big)^2\Big[\delta(q_x+\frac{2\pi n}{l_c})+\delta(q_x-\frac{2\pi n}{l_c})\Big]\Big]\delta(q_y) \tag{4.48}$$

Here f is the filling factor. The integral of Eq.(4.45) in fact diverges for any correlation function with non-vanishing slope at $r = |\mathbf{x}-\mathbf{y}| = 0$, that is if $D_2'(r=0) \neq 0$. An important class are exponential roughness correlations,

$$\langle h(\mathbf{x})h(\mathbf{y})\rangle = \sigma^2 e^{-|(\mathbf{x}-\mathbf{y})|/l_c} \Rightarrow D_{\mathrm{Exp}}(q) = \frac{2\pi\sigma^2 l_c^2}{(1+q^2l_c^2)^{3/2}} \tag{4.49}$$

Their 2-dimensional Fourier-transform decay as a power law proportional to q^{-3} at large momenta. The integral in Eq.(4.45) and other (diagonal) components of the roughness correction $\mathbf{t}^{(2)}$ Eq.(4.40) in this case are logarithmic UV-divergent for *any* correlation length $l_c > 0$.

Experiment [63] does not distinguish Gaussian roughness correlations[5], and roughness profiles with correlation lengths $l_c\omega_p \ll 1$ are readily manufactured. Restricting the model to a particular form for the roughness correlation would not address the fact that the effective low-energy theory does not describe high-momentum contributions to loop integrals correctly. From a practical point of view, roughness corrections to the Casimir free energy and other low-energy observables in this model are exceptionally *sensitive* to high-frequency components of the profile because $\mathbf{G}^{|}(k\sim\infty,0,0;\zeta)\sim k$ at large momenta. Fig. 4.2 depicts typical roughness profiles to three different correlation functions with the same correlation length and variance: a) exponential as in Eq.(4.49), b) Gaussian as

[5] $D_{\mathrm{Gauss}}(q) = D_\infty(q)$ and $D_{\mathrm{Exp}}(q) = D_{1/2}(q)$ in the class of L_1 correlations $\{D_s(q) := 2\pi\sigma^2 l_c^2(1+\frac{q^2lc^2}{2s})^{-s-1}$, with $s>0\}$. The corresponding coordinate space correlation functions are $D_s(r) = \sigma^2\frac{2(r\sqrt{2s}/l_c)^s}{2^s\Gamma[s]}K_s(r\sqrt{2s}/l_c)$. Ref. [4] uses a correlation in this affine class with $s = 0.9$ for which the loop integral converges but is sensitive to contributions from high-momenta.

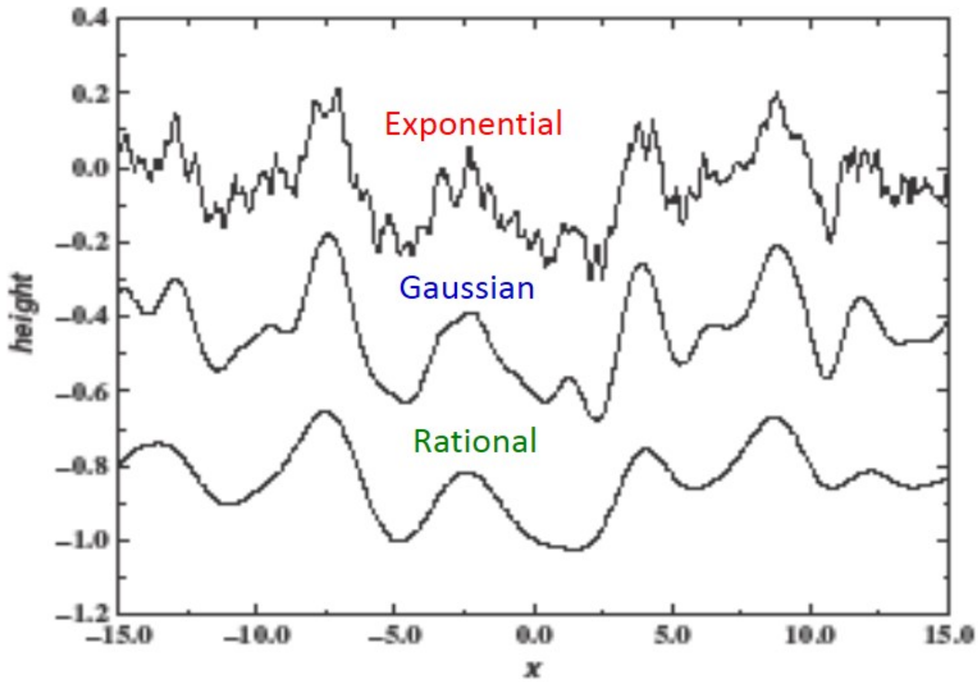

Figure 4.2: Typical cross-sections of 2-dimensional profiles with different correlations (reproduced from Ref. [2]). From the top: profile with the exponential correlation $D_{\text{Exp}}(q)$ of Eq.(4.49)); profile with the Gaussian correlation $D_{\text{Gauss}}(q)$ of Eq.(4.46); profile with a rational correlation (see text). The correlation length and variance are the same for all three profiles. For clarity the average height of the profiles differs by -0.4. Units are arbitrary. Note that only high-frequency components of the profiles differ significantly.

in Eq.(4.46) and c) Rational as $D_{\mathrm{Rational}}(r) = \sigma^2/(1+(r/l_c)^2)^2$. It is evident from Fig. 4.2 that the three profiles differ only in their high-frequency components. However, to leading order in the variance, corrections to the low-energy scattering matrix apparently are very different for the three types of profiles. The roughness correction diverges in the exponential case a) but is finite for profiles b) and c). This sensitivity can be traced to the UV behavior of the 1-loop integrands like that of Eq.(4.45). It is unphysical and an artifact of taking the low-energy effective theory beyond its limits.

Analogous problems arise in any non-renormalizable low-energy effective field theory [83, 76] and we here prescribe a common cure: whereas high momenta may dominate loop corrections to the scattering matrix, they generally are sufficiently suppressed in differences thereof. Differences of elements of the scattering matrix thus often can be reliably estimated within the framework of the low-energy effective field theory. However, phenomenological input is required to determine the high-momentum contributions to loop integrals that are beyond the reach of the low-energy model.

One for instance can rewrite $t^{(2)}_{xx}(\mathbf{k},\zeta)$ of Eq.(4.40) in the form,

$$
\begin{aligned}
t^{(2)}_{xx}(\mathbf{k},\zeta) &= t^{(2)}_{xx}(0,\zeta) + (t^{(2)}_{xx}(\mathbf{k},\zeta) - t^{(2)}_{xx}(0,\zeta)) \\
&= t^{(2)}_{xx}(0,\zeta) \\
&- (\varepsilon-1)^2 \int \frac{d\mathbf{k}'}{(2\pi)^2}\left(\frac{\kappa'\kappa'_\varepsilon\cos^2\theta}{\kappa'_\varepsilon+\varepsilon\kappa'} + \frac{\zeta^2\sin^2\theta}{\kappa'_\varepsilon+\kappa'}\right)(D(|\mathbf{k}'-\mathbf{k}|) - D(k')) \\
&= t^{(2)}_{xx}(0,\zeta) \\
&- (\varepsilon-1)^2 \int \frac{d\mathbf{q}}{(2\pi)^2}\Big(\frac{\kappa'\kappa'_\varepsilon(\hat{\mathbf{k}}\cdot\hat{\mathbf{k}}')^2}{\kappa'_\varepsilon+\varepsilon\kappa'} + \frac{\zeta^2(1-(\hat{\mathbf{k}}\cdot\hat{\mathbf{k}}')^2)}{\kappa'_\varepsilon+\kappa'} - \frac{\kappa\kappa_\varepsilon(\hat{\mathbf{k}}\cdot\hat{\mathbf{q}})^2}{\kappa_\varepsilon+\varepsilon\kappa} \\
&- \frac{\zeta^2(1-(\hat{\mathbf{k}}\cdot\hat{\mathbf{q}})^2)}{\kappa_\varepsilon+\kappa}\Big)D(q)
\end{aligned}
\tag{4.50}
$$

where $\mathbf{q} = \mathbf{k}'-\mathbf{k}$, $\kappa'_\varepsilon = \sqrt{(\mathbf{k}+\mathbf{q})^2+\zeta^2\varepsilon(\zeta)}$ and $\kappa_\varepsilon = \sqrt{\mathbf{q}^2+\zeta^2\varepsilon(\zeta)}$ in the last expression. The one-loop correction to $t^{(2)}_{xx}(0,\zeta)$ in Eq.(4.50) converges for any

$D(q)$ for which

$$\langle h^2(\mathbf{x})\rangle = \int_0^\infty \frac{qdq}{2\pi} D(q) = \sigma^2 < \infty \ . \tag{4.51}$$

More importantly, the correction to $t^{(2)}_{xx}(0,\zeta)$ in Eq.(4.50) is of order $(k\sigma)^2$ and thus small at low transverse momenta for *any* correlation length l_c of the profile. The correction to $t^{(2)}_{xx}(0,\zeta)$ therefore is reliably computed in the framework of the low-energy theory.

It remains to determine $\mathbf{t}^{(2)}(0,\zeta)$. This is the correction due to roughness to the (analytically continued) scattering matrix of an electromagnetic wave of frequency $\omega = i\zeta$ that is incident perpendicular to the rough plate. $\mathbf{t}^{(2)}(0,\zeta)$ is a single-interface low-energy characteristic that, at least in principle, can be derived from ellipsometric measurements of the rough interface. Instead of directly incorporating such experimental data, we here model the corrections of order σ^2 to the low-energy scattering matrix by the coupling to surface plasmons induced by roughness. We determine the coupling by demanding that this phenomenological description of $\mathbf{t}^{(2)}(0,\zeta)$ be consistent with the low-energy field theory in the limit of large correlation length l_c and that the ideal metal limit exist for any correlation length.

Roughness couples electromagnetic radiation to surface plasmons [84]. At low transverse wave numbers this coupling is of the order of the rms-roughness σ. To order σ^2 the corresponding tree-level correction to the scattering matrix is schematically shown in Fig. 4.3. The diagram depicts the creation, propagation and subsequent annihilation of a surface plasmon by an incident electromagnetic wave.

For $\mathbf{k} \to 0$ a surface plasmon on the interface of a flat plate at $z = 0$ propagates with the dyadic,

$$\mathbf{G}_{\text{plasmon}}(\mathbf{k} \sim 0;\zeta) = \tilde{\mathbf{G}}^{|}(k=0, z=z'=0;\zeta) \sim \frac{\zeta}{1+\sqrt{\varepsilon(\zeta)}} \text{diag}(1,1,0) \ . \tag{4.52}$$

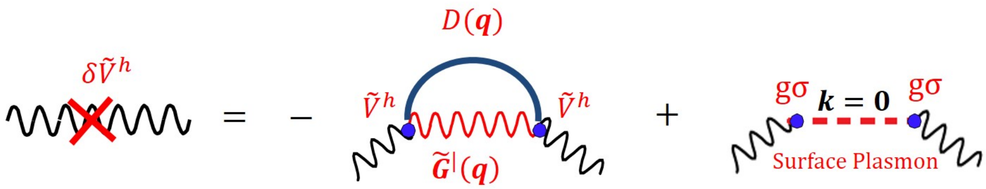

Figure 4.3: The counter potential $\tilde{\mathbf{V}}^h$ includes two contributions of order σ^2. It subtracts the one-loop contribution to the average scattering matrix at vanishing (transverse) momentum and replaces it by the phenomenological one. The latter is modeled by the tree-level plasmon contribution at vanishing transverse momentum. The plasmon couples to radiation due to the roughness of the surface only and its coupling $g^2\sigma^2$ to this order is proportional to the variance of the roughness profile. The plasmon propagator (dashed) is the one-interface Green's function $\tilde{\mathbf{G}}(z = z' = k = 0)$. We show in the text that $g^2(\zeta/\omega_p, l_c\omega_p) = 1$ at low frequencies.

To second order in σ, the correction $\mathbf{t}^{(2)}(0,\zeta)$ to the scattering matrix at vanishing momentum transfer from surface plasmons thus is,

$$\mathbf{t}^{(2)}(0,\zeta) \approx \mathbf{t}^{(2)}_{\text{Plasmon}}(\mathbf{k}=0,\zeta) = -\sigma^2 g^2 \frac{\zeta(\varepsilon(\zeta)-1)^2}{1+\sqrt{\varepsilon(\zeta)}} \text{diag}(1,1,0) \ , \tag{4.53}$$

where $g(\zeta/\omega_p; l_c\omega_p)$ is a dimensionless coupling that depends only on the frequency of the plane wave incident perpendicular to the rough plate. The coupling $g(\zeta/\omega_p; l_c\omega_p)$ in general is not calculable within this low-energy effective model and has to be determined phenomenologically. We argue below that $g^2 \sim 1$ at low energies.

Since $g(\zeta/\omega_p; l_c\omega_p)$ is a phenomenological *function* rather than just a constant, one could have directly modeled $\mathbf{t}^{(2)}(0,\zeta)$. However, the ansatz of Eq.(4.53) is consistent with the low-energy scattering theory in the sense that roughness correlation functions for large correlation length $l_c\omega_p \gg 1$ approach representations of the δ-distribution[6],

$$\lim_{l_c\to\infty} D(\mathbf{q}; l_c) = (2\pi)^2\sigma^2\delta(\mathbf{q}) \tag{4.54}$$

[6]on the space of measurable L^0 test-functions. The *subtracted* loop integrand is in this class.

Loop integrals in the limit $l_c \to \infty$ become trivial and furthermore involve only momenta $q \ll \omega_p$. Predictions of the low energy theory therefore should be reliable in the limit $l_c \to \infty$. Evaluating the loop integrals of Eq.(4.40) for $k \to 0$ using Eq.(4.54) and comparing with the plasmon contribution of Eq.(4.53) this requires that ,

$$g(\zeta/\omega_p, l_c\omega_p \sim \infty) = 1 \ . \tag{4.55}$$

We will find that Eq.(4.55) not only ensures consistency, but also the existence of an ideal metal limit. It in addition ensures that the proximity force approximation (PFA) to the Casimir free energy is recovered in the limit $l_c\omega_p \to \infty$.

At finite $l_c\omega_p \lesssim 1$ the coupling $g(\zeta/\omega_p, l_c\omega_p \lesssim 1)$ in principle has to be determined phenomenologically. However, the coupling is severely constrained if we impose some theoretical requirements. Since the range of frequencies ζ that contribute to the Casimir energy satisfy $\zeta a \lesssim 1 \ll \omega_p a$ and the plasmon coupling does not diverge at low frequencies, we in the following ignore the ζ-dependence of $g(\zeta/\omega_p, l_c\omega_p)$ and for low frequencies approximate,

$$0 < g(\zeta/\omega_p, l_c\omega_p) \sim g(l_c\omega_p) \lesssim 1 \tag{4.56}$$

in Eq.(4.53). Eq.(4.56) assumes that the plasmon coupling is strongest for an ideal metal $l_c\omega_p \gg 1$. Note that the fact that g is dimensionless links the ideal metal to the large l_c limits.

To order σ^2 the subtraction of the one-loop contribution $\mathbf{t}^{(2)}(\mathbf{k} = 0, \zeta)$ and its replacement by phenomenological plasmon scattering is implemented by a (local in transverse coordinates) counter term potential $\delta\tilde{\mathbf{V}}(\zeta, z)$ of the form,

$$\begin{aligned}
\delta\tilde{\mathbf{V}}^h &= \mathrm{diag}(\delta V^h_{xx}(\zeta,z), \delta V^h_{yy}(\zeta,z), (\varepsilon\theta(z)+\frac{1}{\varepsilon}\theta(-z))\delta V^h_{zz}(\zeta,z)), \text{ with} \\
\delta V^h_{xx}(\zeta,z) &= \delta V^h_{yy}(\zeta,z) \\
&= \delta(z)(\varepsilon-1)^2\left[\frac{-g^2\sigma^2\zeta}{1+\sqrt{\varepsilon}} + \int_0^\infty \frac{kdk}{4\pi} D(k)\left(\frac{\kappa\kappa_\varepsilon}{\varepsilon\kappa+\kappa_\varepsilon} + \frac{\zeta^2}{\kappa+\kappa_\varepsilon}\right)\right] \\
\delta V^h_{zz}(\zeta,z) &= -\delta(z)(\varepsilon-1)^2\int_0^\infty \frac{kdk}{2\pi} D(k)\frac{k^2}{(\varepsilon\kappa+\kappa_\varepsilon)}\ . \qquad (4.57)
\end{aligned}$$

Note that the support of $\delta V^h(\zeta, z)$ is in the immediate vicinity of $z = 0$ only. Due to rotational and translational symmetry of the rough plate, this "counter potential" is local and diagonal but anisotropic[7].

As mentioned in Sec.4.2, the counter potential may be interpreted as the modification of the dielectric permittivity (to order σ^2) in the vicinity of the flat interface necessary to describe the rough interface with permittivity ε and roughness correlation $D_2(\mathbf{x}-\mathbf{y})$. There is no compelling reason for perturbing about a flat interface with the *same* permittivity as the rough one. We have seen that the expansion about a flat plate with the same permittivity is not consistent with the low-energy description, since it implies unacceptably high momenta in the loop integrals. Expanding instead about the bare permittivity function of Eq.(4.17) yields a better controlled approximation and Eq.(4.57) strongly suppresses high-momentum contributions to 1-loop.

4.3.4 Roughness Correction to the Casimir free energy of order σ^2

We finally are in a position to evaluate the roughness correction to the Casimir free energy within the framework of the improved low-energy effective field theory.

[7]The product of distributions in $\delta\tilde{\mathbf{V}}^h(\zeta,z) \propto \delta(z)(\varepsilon(\zeta)\theta(z)+\varepsilon^{-1}(\zeta)\theta(-z))$ here means that integration with a test function $f(z) \in L^0$ gives $\int dz(\varepsilon\theta(z)+\varepsilon^{-1}\theta(-z))\delta(z)f(z) := \frac{1}{2}(\varepsilon\lim_{z\to 0_+} + \varepsilon^{-1}\lim_{z\to 0_-})f(z)$.

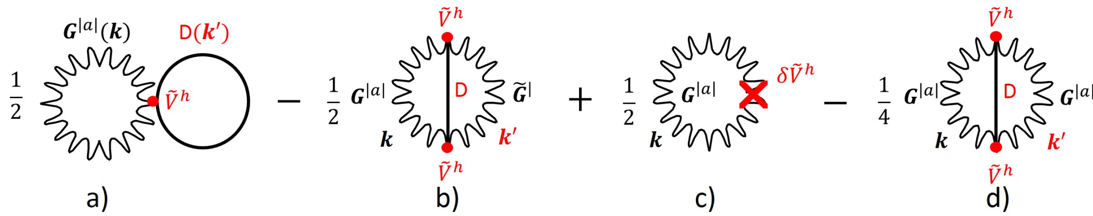

Figure 4.4: Feynman diagrams for the contributions of order σ^2 to the roughness correction of the Casimir free energy of a rough and a flat interface. a) and b) give corrections from a single scattering off the rough surface and include only one factor of $\mathbf{G}^{|a|}$. c) gives the contribution from the counter potential defined in Eq.(4.57) whose two terms are shown in Fig. 4.3. This contribution eliminates the uncontrolled high-momentum contributions to the loop integral of b) in favor of a phenomenological (plasmon) description. d) is the 2-scattering contribution of order σ^2 and includes two factors of $\mathbf{G}^{|a|}$. The momenta in either loop of this term are exponentially restricted to $k, k' \lesssim 1/(2a) \ll \omega_p$ and no subtraction is required. Wavy lines denote photon propagators for a single flat interface, $\tilde{\mathbf{G}}^{|}(\mathbf{k}')$, or their correction, $\mathbf{G}^{|}a|(\mathbf{k})$, due to the presence of a second flat interface at a mean distance a. Solid lines represent the Fourier transform $D(\mathbf{k}-\mathbf{k}')$ of the roughness correlation function. A (red) dot indicates the effective anisotropic interaction potential $\tilde{V}^h$ due to the roughness profile defined in Eq.(4.37). Combinatorical factors are shown but traces and momentum integrals have been suppressed.

From Eq.(4.32) and Eq.(4.38) we have altogether four contributions to order σ^2,

$$\begin{aligned}\Delta F_T^{\text{Cas}}[a] &= \tfrac{1}{2}\langle \text{Tr}\tilde{\mathbf{V}}^h\mathbf{G}^{|a|}\rangle - \tfrac{1}{2}\langle \text{Tr}\tilde{\mathbf{V}}^h\tilde{\mathbf{G}}^{|}\tilde{\mathbf{V}}^h\mathbf{G}^{|a|}\rangle + \tfrac{1}{2}\text{Tr}\delta\tilde{\mathbf{V}}^h\mathbf{G}^{|a|} \\ &- \tfrac{1}{4}\langle \text{Tr}\tilde{\mathbf{V}}^h\mathbf{G}^{|a|}\tilde{\mathbf{V}}^h\mathbf{G}^{|a|}\rangle + \mathcal{O}(\sigma^3)\ . \end{aligned} \tag{4.58}$$

The corresponding Feynman diagrams are shown in Fig. 4.4 and we consider them in turn.

The first is the seagull contribution of Fig. 4.4a given by,

$$\begin{aligned}\tfrac{1}{2}\langle \text{Tr}\tilde{\mathbf{V}}^h\mathbf{G}^{|a|}\rangle &= -\frac{AT}{2}\sum_n(\varepsilon-1)\langle\int_0^\infty \frac{kdk}{2\pi}\int_0^{h(\mathbf{x})}dz(G_{xx}^{|a|}(k,z,z;\zeta)+G_{yy}^{|a|}(k,z,z;\zeta) \\ &+ (\varepsilon\theta(z)+\frac{\theta(-z)}{\varepsilon})G_{zz}^{|a|}(k,z,z;\zeta))\rangle \qquad (4.59)\\ &= -AT\sum_n\int_0^\infty\frac{kdk}{\pi}\kappa\kappa_\varepsilon(\frac{\bar{r}^2}{e^{2a\kappa}-\bar{r}^2}+\frac{r^2}{e^{2a\kappa}-r^2})\langle\int_0^{h(\mathbf{x})}zdz\rangle+\mathcal{O}(\sigma^3) \\ &= -AT\sigma^2\sum_{\zeta\in\{\zeta_n\}}\int_0^\infty\frac{kdk}{2\pi}\kappa\kappa_\varepsilon(\frac{\bar{r}^2}{e^{2a\kappa}-\bar{r}^2}+\frac{r^2}{e^{2a\kappa}-r^2})+\mathcal{O}(\sigma^3)\ .\end{aligned}$$

The expressions of Eq.(B.7) in App B. here have been expanded for small z. There are (as expected) no corrections of order σ and the final line exhibits equally weighted contributions from both polarizations. Note that this remarkable simplification occurs only upon summation of all δ-function contributions to $\mathbf{G}^{\|}_{zz}$ - which leads to an expansion in $\tilde{\mathbf{V}}^h$, defined in Eq.(4.37), rather than in the original $\mathbf{V}^h$.

This roughness contribution to the free energy is entirely local and does not depend on the correlation length l_c. The loop-integral over transverse momenta and the sum over Matsubara frequencies are exponentially restricted to momenta $2a\kappa \lesssim 1$ and the evaluation of the seagull diagram using the low-energy propagators should be accurate for all $a\omega_p \gg 0.5$, that is for $a \gtrsim 12$nm in the case of gold plates.

Due to the κ_ε factor of the integrand, the contribution of Eq.(4.59) is proportional to $\omega_p\sigma^2/a^4$ for $a\omega_p \gg 1 \gg Ta$ and diverges in the ideal metal limit. Fortunately the seagull is not the whole story to order σ^2.

The other contribution to the Casimir free energy of order σ^2 from a single scattering off the rough interface corresponds to the diagram of Fig. 4.4b. This unsubtracted 2-loop contribution is formally given by,

$$\begin{aligned}
&-\tfrac{1}{2}\langle \mathrm{Tr}\tilde{\mathbf{V}}^h\tilde{\mathbf{G}}^{|}\tilde{\mathbf{V}}^h\mathbf{G}^{|a|}\rangle \\
&= -\frac{AT}{2}\sum_n\int\frac{d\mathbf{k}d\mathbf{k}'}{(2\pi)^4}\mathrm{Tr}\Big[D_{++}(q)\tilde{\mathbf{G}}^{|(n)}_{++}(\mathbf{k}')\mathbf{V}^{(n)}_{+}\mathbf{G}^{|a|(n)}_{++}(\mathbf{k})\mathbf{V}^{(n)}_{+} \\
&+D_{--}(q)\tilde{\mathbf{G}}^{|(n)}_{--}(\mathbf{k}')\mathbf{V}^{(n)}_{-}\mathbf{G}^{|a|(n)}_{--}(\mathbf{k})\mathbf{V}^{(n)}_{-} + D_{-+}(q)\tilde{\mathbf{G}}^{|(n)}_{-+}(\mathbf{k}')\mathbf{V}^{(n)}_{+}\mathbf{G}^{|a|(n)}_{+-}(\mathbf{k})\mathbf{V}^{(n)}_{-} \\
&+D_{+-}(q)\tilde{\mathbf{G}}^{|(n)}_{+-}(\mathbf{k}')\mathbf{V}^{(n)}_{-}\mathbf{G}^{|a|(n)}_{-+}(\mathbf{k})\mathbf{V}^{(n)}_{+}\Big],
\end{aligned} \tag{4.60}$$

with $q = |\mathbf{k}-\mathbf{k}'|$ and interaction vertices,

$$\mathbf{V}^{(n)}_{+} = (\varepsilon(\zeta_n)-1)\mathrm{diag}(1,1,\varepsilon(\zeta_n)),\quad \mathbf{V}^{(n)}_{-} = (\varepsilon(\zeta_n)-1)\mathrm{diag}(1,1,1/\varepsilon(\zeta_n))\ . \tag{4.61}$$

$\mathbf{G}^{(n)}_{\pm\mp}(\mathbf{k}) := \mathbf{G}(\mathbf{k}, z\to 0^{\pm}, z'\to 0^{\mp};\zeta_n)$ denote one-sided limits of propagators. Explicit expressions are given in Eq.(B.8). The correlation functions $D_{\pm\mp}(q)$ of positive and negative components of the roughness profile are defined in Eq.(4.41) and computed in App. B.2.

A lengthy but otherwise straightforward evaluation of Eq.(4.60) using the expressions of Eq.(B.8) and Eq.(B.3) yields,

$$
\begin{aligned}
&-\tfrac{1}{2}\langle \mathrm{Tr}\tilde{\mathbf{V}}^h\tilde{\mathbf{G}}^{|}\tilde{\mathbf{V}}^h\mathbf{G}^{|a|}\rangle \\
&= -\frac{AT}{2}\sum_n(\varepsilon-1)^2\int_0^\infty\frac{kdk}{2\pi}\int_0^\infty\frac{k'dk'}{(2\pi)^2}\int_{-\pi}^{\pi}d\theta D(\sqrt{k^2+k'^2-2kk'\cos\theta}) \\
&\times\Big[\frac{r(1-r^2)\zeta^2}{2(e^{2a\kappa}-r^2)\kappa_\varepsilon}\left(\frac{\kappa'\kappa'_\varepsilon\sin^2\theta}{\varepsilon\kappa'+\kappa'_\varepsilon}+\frac{\zeta^2\cos^2\theta}{\kappa'+\kappa'_\varepsilon}\right) \\
&+\frac{\bar{r}(1-\bar{r}^2)}{2(e^{2a\kappa}-\bar{r}^2)\varepsilon}\left(\frac{\varepsilon k^2k'^2-\kappa_\varepsilon^2\kappa'\kappa'_\varepsilon\cos^2\theta}{\kappa_\varepsilon(\varepsilon\kappa'+\kappa'_\varepsilon)}-kk'\bar{r}'\cos\theta-\frac{\kappa_\varepsilon\zeta^2\sin^2\theta}{(\kappa'+\kappa'_\varepsilon)}\right)\Big]\ . \qquad (4.62)
\end{aligned}
$$

The signed correlation functions in Eq.(4.60) combine and Eq.(4.62) depends on the roughness correlation $D(|\mathbf{k}-\mathbf{k}'|)$ only. In App. B.3 the integral over θ in Eq.(4.62) is performed analytically for the class of correlations $D_s(q)$, but this angular integral in general has to be evaluated numerically. More importantly, the leading term of order ω_p in the limit $\omega_p\to\infty$ of Eq.(4.62) cancels the leading asymptotic behavior $\propto\omega_p$ of the seagull term in Eq.(4.59).

The limit of Eq.(4.62) for large correlation length $l_c\gg 1/\omega_p$ is found using Eq.(4.54) to trivially evaluate the $\mathbf{k}'$-integrals. Some algebraic manipulations simplify the expression in this limit to,

$$
\begin{aligned}
&-\tfrac{1}{2}\langle \mathrm{Tr}\tilde{\mathbf{V}}^h\tilde{\mathbf{G}}^{|}\tilde{\mathbf{V}}^h\mathbf{G}^{|a|}\rangle \\
&\xrightarrow{l_c\to\infty} AT\sigma^2\sum_n\int_0^\infty\frac{kdk}{2\pi}\kappa(\kappa_\varepsilon-\kappa)\left(\frac{r^2}{e^{2a\kappa}-r^2}+\frac{\bar{r}^2}{e^{2a\kappa}-\bar{r}^2}\right)\ . \qquad (4.63)
\end{aligned}
$$

Both loop integrals of this contribution (shown in Fig. 4.4d) to the Casimir free energy are exponentially constrained to low momenta $k,k'\lesssim 1/(2a)\ll\omega_p$ –

a regime in which the low-energy description is expected to hold. We find that,

$$
\begin{aligned}
&-\tfrac{1}{4}\langle \mathrm{Tr}\tilde{\mathbf{V}}^h\tilde{\mathbf{G}}^{|a|}\tilde{\mathbf{V}}^h\mathbf{G}^{|a|}\rangle \\
&= -\frac{AT}{16}\sum_n(\varepsilon-1)^2\int_0^\infty\frac{kdk}{2\pi}\int_0^\infty\frac{k'dk'}{(2\pi)^2}\int_{-\pi}^{\pi}d\theta D(\sqrt{k^2+k'^2-2kk'\cos\theta}) \\
&\times\Big[\frac{r(1-r^2)\zeta^2}{(e^{2a\kappa}-r^2)\kappa_\varepsilon}\left(\frac{r'(1-r'^2)\zeta^2\cos^2\theta}{(e^{2a\kappa'}-r'^2)\kappa'_\varepsilon}-\frac{2\bar{r}'(1-\bar{r}'^2)\kappa'_\varepsilon\sin^2\theta}{(e^{2a\kappa'}-\bar{r}'^2)\varepsilon}\right) \\
&+\frac{\bar{r}\bar{r}'(1-\bar{r}^2)(1-\bar{r}'^2)}{(e^{2a\kappa}-\bar{r}^2)(e^{2a\kappa'}-\bar{r}'^2)}\left(\frac{k^2k'^2}{\kappa_\varepsilon\kappa'_\varepsilon}+\frac{2kk'\cos\theta}{\varepsilon}+\frac{\kappa_\varepsilon\kappa'_\varepsilon\cos^2\theta}{\varepsilon^2}\right)\Big]\,. \qquad (4.64)
\end{aligned}
$$

For profiles with large correlation length $l_c \gg 2a \gtrsim 1/\omega_p$ Eq.(4.64) simplifies to

$$
\begin{aligned}
&-\tfrac{1}{4}\langle \mathrm{Tr}\tilde{\mathbf{V}}^h\tilde{\mathbf{G}}^{|a|}\tilde{\mathbf{V}}^h\mathbf{G}^{|a|}\rangle \\
&\xrightarrow{l_c\to\infty} -AT\sigma^2\sum_n\int_0^\infty\frac{kdk}{2\pi}\kappa^2\left(\frac{r^4}{(e^{2a\kappa}-r^2)^2}+\frac{\bar{r}'^4}{(e^{2a\kappa'}-\bar{r}'^2)^2}\right) \qquad (4.65)
\end{aligned}
$$

due to Eq.(4.54) (shown in Fig. 4.4d).

As for $\mathbf{t}^{(2)}$ in Eq.(4.40), the loop-integral of Eq.(4.62) generally includes high momentum contributions $k' \gg \omega_p$ for which the low-energy description is not justified. The same 1-loop counter potential of Eq.(4.57) that corrects roughness corrections to the scattering matrix to 1-loop also removes the uncontrolled high-momentum contributions to the Casimir free energy and replaces them by the phenomenological plasmon contribution.

The correction of the Casimir free energy by this counter potential is shown diagrammatically in Fig. 4.4c and the two Feynman diagrams of this counter term are depicted in Fig. 4.3. To order σ^2 the contribution to the Casimir free energy from the counter potential $\delta\tilde{\mathbf{V}}$ of Eq.(4.57) is,

$$
\begin{aligned}
&\tfrac{1}{2}\mathrm{Tr}\delta\tilde{\mathbf{V}}\mathbf{G}^{|a|} \qquad (4.66)\\
&= \frac{AT}{2}\sum_n(\varepsilon-1)^2\int_0^\infty\frac{kdk}{2\pi}\int_0^\infty\frac{k'dk'}{2\pi}D(k')\Big[\frac{\bar{r}(1-\bar{r}^2)k^2}{2(e^{2a\kappa}-\bar{r}^2)\kappa_\varepsilon}\frac{k'^2}{(\varepsilon\kappa'+\kappa'_\varepsilon)} \\
&+\left(\frac{r(1-r^2)\zeta^2}{2(e^{2a\kappa}-r^2)\kappa_\varepsilon}-\frac{\bar{r}(1-\bar{r}^2)\kappa_\varepsilon}{2(e^{2a\kappa}-\bar{r}^2)\varepsilon}\right)\left(\frac{\kappa'\kappa'_\varepsilon/2}{\varepsilon\kappa'+\kappa'_\varepsilon}+\frac{\zeta^2/2}{\kappa'+\kappa'_\varepsilon}-\frac{g^2\zeta}{1+\sqrt{\varepsilon}}\right)\Big]
\end{aligned}
$$

This correction to the Casimir free energy remains finite in the ideal metal limit when Eq.(4.55) is satisfied. The existence of this limit is assured by the consistency of the low-energy theory in the limit $l_c \gg 1/\omega_p$. Using Eq.(4.54), the counterterm correction of Eq.(4.66) for $l_c \gg 1/\omega_p$ becomes,

$$
\begin{aligned}
&\tfrac{1}{2}\mathrm{Tr}\delta\tilde{\mathbf{V}}\mathbf{G}^{|a|}|_{l_c\to\infty} \qquad (4.67)\\
&= AT\sigma^2 \sum_n (g^2-1)\zeta(\sqrt{\varepsilon}-1)\int_0^\infty \frac{kdk}{2\pi}\kappa\left(\frac{r^2}{e^{2a\kappa}-r^2}+\frac{\bar{r}^2\kappa_\varepsilon^2}{(e^{2a\kappa}-\bar{r}^2)(\varepsilon k^2+\kappa_\varepsilon^2)}\right)\\
&\xrightarrow{g^2\to 1} 0\ ,
\end{aligned}
$$

and vanishes when Eq.(4.55) is enforced. This should be expected of a model that is valid at low energies. Note that magnetic and electric modes do not enter the counter term correction symmetrically even at large correlation length because we subtracted at $\mathbf{k}=0$: the factor $\kappa_\varepsilon^2/(\varepsilon k^2+\kappa_\varepsilon^2)$ in Eq.(4.67) differs from unity in order $k^2/{\omega_p}^2$ only.

4.4 Discussion

4.4.1 The Limit $l_c \gg \max(1/\omega_p, a)$: the Proximity Force Approximation

Although $l_c \gg a$ is a necessary condition for the PFA, the limiting expressions of Eqs. (4.63) and (4.67) evidently hold only when l_c is large compared to a *and* $1/\omega_p$. The latter restriction arises because the scattering matrix locally can be approximated by a flat surface only if the plasma length is shorter than the typical length scale of the surface structure.

For a rough profile with $l_c \gg \max(1/\omega_p, a)$ Eqs. (4.63), (4.67) and (4.65) should all be reasonable approximations. Including the seagull term of Eq.(4.59), the roughness correction to the Casimir free energy of Eq.(4.58) in the limit of large correlation length $l_c \gg \max(1/\omega_p, a)$ is,

$$\begin{aligned}
\Delta F_T^{Cas}[a]|_{l_c\to\infty} &= -AT\sigma^2 \\
&\times \sum_n \int_0^\infty \frac{\kappa^2 k dk}{2\pi} \left(\frac{r^4}{(e^{2a\kappa}-r^2)^2} + \frac{r^2}{e^{2a\kappa}-r^2} + \frac{\bar{r}^4}{(e^{2a\kappa}-\bar{r}^2)^2} + \frac{\bar{r}^2}{e^{2a\kappa}-\bar{r}^2} \right) \\
&= \tfrac{1}{2}\sigma^2 \frac{\partial^2}{\partial a^2} \frac{AT}{2} \sum_n \int_0^\infty \frac{kdk}{2\pi} \ln\left(1-r^2 e^{-2a\kappa}\right) + \ln\left(1-\bar{r}^2 e^{-2a\kappa}\right) \\
&= \tfrac{1}{2}\sigma^2 \frac{\partial^2}{\partial a^2} F_T^{\|}(a) \ ,
\end{aligned} \tag{4.68}$$

where $F_T^{\|}(a)$ is the Casimir free energy for two flat parallel semi-infinite slabs at a separation a given by Eq.(4.21). This is precisely the roughness correction in PFA for a rough surface with $\langle h(\mathbf{x})\rangle = 0$ and $\langle h^2(\mathbf{x})\rangle = \sigma^2$. Although trivial, one should note that the PFA here emerges in the limit of large l_c from requiring consistency of the low-energy effective field theory. It is due to the absence of high-momentum contributions in this limit and does not require any phenomenological correction.

4.4.2 Ideal Metal Limit $\varepsilon \to \infty$

It perhaps is remarkable that the requirement of Eq.(4.55) not only guarantees that the PFA is recovered in the $l_c \to \infty$ limit but also ensures the existence of an ideal metal limit. If g^2 is analytic at $\zeta = 0$ one can argue that ζ/ω_p and $1/(l_c\omega_p)$ (see Eq.(4.74)) corrections are absent and g^2 for large ω_p has the expansion

$g^2 = 1 + \mathcal{O}(\zeta^2/\omega_P^2)$. The ideal metal limit in this case is uniquely given by,

$$
\begin{aligned}
&\tfrac{1}{2}\langle \mathrm{Tr}\tilde{\mathbf{V}}^h \mathbf{G}^{|a|}\rangle - \tfrac{1}{2}\langle \mathrm{Tr}\tilde{\mathbf{V}}^h \tilde{\mathbf{G}}^{|}\tilde{\mathbf{V}}^h \mathbf{G}^{|a|}\rangle \\
&\quad = -AT\sum_n \int_0^\infty \frac{kdk}{2\pi}\int_0^\infty \frac{k'dk'}{(2\pi)^2}\int_{-\pi}^{\pi} d\theta D(\sqrt{k^2+k'^2-2kk'\cos\theta}) \\
&\quad \times \Big[\frac{(\zeta^2+kk'\cos\theta)^2+\kappa^2\kappa'^2}{\kappa\kappa'(e^{2a\kappa}-1)} - \frac{4k\zeta^2(k-k'\cos\theta)e^{2\kappa a}}{\kappa^2(e^{2a\kappa}-1)^2}\Big] \qquad (4.69) \\
&-\tfrac{1}{4}\langle \mathrm{Tr}\tilde{\mathbf{V}}^h \tilde{\mathbf{G}}^{|a|}\tilde{\mathbf{V}}^h \mathbf{G}^{|a|}\rangle \\
&\quad = -AT\sum_n \int_0^\infty \frac{kdk}{2\pi}\int_0^\infty \frac{k'dk'}{(2\pi)^2}\int_{-\pi}^{\pi} d\theta D(\sqrt{k^2+k'^2-2kk'\cos\theta}) \\
&\quad \times \frac{(\zeta^2+kk'\cos\theta)^2+\kappa^2\kappa'^2}{(e^{2a\kappa}-1)(e^{2a\kappa'}-1)\kappa\kappa'} \qquad (4.70) \\
&\tfrac{1}{2}\mathrm{Tr}\delta\tilde{\mathbf{V}}\mathbf{G}^{|a|} \\
&\quad = AT\sum_n \int_0^\infty \frac{kdk}{2\pi}\int_0^\infty \frac{k'dk'}{2\pi} D(k')\Big[\frac{2k^2k'^2+(\kappa^2+\zeta^2)(\kappa'-\zeta)^2}{2(e^{2a\kappa}-1)\kappa\kappa'}\Big] \qquad (4.71)
\end{aligned}
$$

Note that the counter term contribution of Eq.(4.71) does not vanish and cancels the contribution from high k'-momenta in Eq.(4.69) also for an ideal metal. High-momentum contributions to the roughness correction thus persist in the ideal metal limit in the unrenormalized theory. Without counter term this perturbative correction would diverge for $l_c \to 0$ (and for some correlations would diverge for *all* l_c). This apparently is at odds with exact calculations for square-wave profiles [85] and demands an explanation. The reason for convergence of these "exact" calculations in the limit $l_c \to 0$ (and divergence of the unsubtracted perturbation theory) for such profiles is subtle and related to the fact that for $l_c \ll \sigma$ the leading term in the exact calculation is $\mathcal{O}(\sigma)$ and not $\mathcal{O}(\sigma^2)$ as perturbation theory suggests [85]. The non-analytic dependence on σ for $l_c \to 0$ arises due to an effective UV-cutoff in the exact calculation of $\mathcal{O}(\sigma)$ – there is no other scale to compare with in this limit. Ignoring this effective cutoff (as a perturbative expansion in σ does) leads to an UV-divergent expression in the limit $l_c \to 0$. The non-analyticity of the exact result for $\sigma/a \ll 1$ in the limit $l_c \to 0$ is only possible if wave-numbers of order $1/\sigma$ of the profile contribute significantly. The non-analyticity in σ in this sense implies that high-momenta $1/a < k' < 1/\sigma$ must dominate the exact Casimir energy calculation for an ideal metal in the limit $0 \leq l_c < \sigma \sim 0$.

A simple model that qualitatively reproduces this explanation of the non-analytic dependence on σ is obtained by replacing $l_c \to l_c + \gamma\sigma$ in the Gaussian correlation function of Eq.(4.46) where the constant γ is of $\mathcal{O}(1)$. For $l_c \gg \sigma$ one recovers the quadratic perturbative dependence on σ in leading order, but for $0 \leq l_c \ll \sigma \to 0$ the k' integral of Eq.(4.69) is of order $\sigma^2/(l_c + \gamma\sigma) \xrightarrow{l_c \ll \sigma} \sigma/\gamma$ as in the "exact" calculation. The UV-divergence $\propto 1/\sigma^3$ of the k'-integral that leads to this (non-analytic) behavior is due to momenta $k' \sim 1/\sigma \gg 1/a$. Although the exact evaluation of such high-momentum contributions is of itself correct, the low-energy description used to compute them is not justified. The fact that the plasmon contributes and the counter term of Eq.(4.71) removes high momentum contributions even for an ideal metal indirectly supports the assertion that roughness corrections of real materials in fact remain analytic in the variance σ^2 also in the limit of uncorrelated roughness.

4.4.3 The Limit of Uncorrelated Roughness and the Plasmon Coupling g^2

The high-roughness limit $l_c \ll 1/\omega_p$ is obtained by examining the loop integrals in Eqs. (4.59), (4.62), and (4.66) at large momentum transfers $q = |\mathbf{k'} - \mathbf{k}|$. In the limit of uncorrelated roughness $l_c \to 0$ the correction is,

$$\begin{aligned}
&\Delta F_T^{\mathrm{Cas}}[a]|_{l_c \to 0} \\
&\quad = -AT\sigma^2 \sum_n \int_0^\infty \frac{kdk}{2\pi} \Big[\frac{\bar{r}^2 \kappa\kappa_\varepsilon (2\frac{\varepsilon-1}{\varepsilon+1}k^2 + \kappa_\varepsilon^2 - g^2(\sqrt{\varepsilon}-1)\zeta\kappa_\varepsilon)}{(e^{2a\kappa} - \bar{r}^2)(k^2\varepsilon + \kappa_\varepsilon^2)} \\
&\quad + \frac{r^2\kappa(\kappa_\varepsilon - g^2(\sqrt{\varepsilon}-1)\zeta)}{e^{2a\kappa} - r^2} \Big]
\end{aligned} \tag{4.72}$$

Note that the correction to the Casimir free energy for $l_c = 0$ is strictly negative when $g^2 \leq 1$. The Casimir free energy of a rough interface thus is always larger in magnitude than of a flat one at the same average separation. We believe this is due to two opposing effects. The specular reflection off a rough surface with vanishing l_c but finite σ never is quite the same as that off a flat interface with the *same* bulk permittivity: the situation is analogous to the change in bulk permittivity due to the inclusion of sub-wavelength spheres of a different material. Since the included "material" in this case is vacuum with $\varepsilon = 1$, the effective reflection coefficient decreases compared to that for the flat plate. This effect by itself would tend to decrease the Casimir free energy in magnitude for $l_c \to 0$. However, this decrease is more than compensated by the reduced separation to this effective interface.

The ideal metal limit of Eq.(4.72) exists only for $g^2 \to 1$ and is analytically given by,

$$\begin{aligned}
&\Delta F_T^{\rm Cas}[a, l_c \ll 1/\omega_p \to 0] \qquad (4.73)\\
&= -AT\sigma^2 \sum_n \int_0^\infty \frac{kdk}{2\pi} \frac{\zeta(\kappa^2+\zeta^2)}{\kappa(e^{2a\kappa}-1)} \xrightarrow{T\to 0} -\frac{9A\sigma^2}{32\pi^2 a^5}\zeta(5) \approx -0.02955\frac{A\sigma^2}{a^5} \ .
\end{aligned}$$

The ideal metal and $l_c \to 0$ limits in fact commute and $g^2 \to 1$ is required for the ideal metal limit to exist. Assuming that $g^2(\zeta l_c, l_c\omega_p)$ is analytic in both arguments, the existence of an ideal metal limit implies,

$$1 = \lim_{\substack{\omega_p\to\infty \\ l_c\omega_p=\beta}} g^2(\zeta l_c, l_c\omega_p) = g^2(0,\beta) \ . \qquad (4.74)$$

We therefore have that $g^2 = 1$ at low frequencies for any value of l_c and ω_p. In the following we consider only the (plasmon) coupling,

$$g^2 = 1 \ . \qquad (4.75)$$

4.5 The Effective Low-Energy Field Theory approach

Although we obtained a roughness correction that is compatible with the low-energy theory of Schwinger by the Green's function approach, it is instructive to construct the effective low energy field theory from which these corrections derive. The effective field theory allows one to in principle explore other approximations and corrections. It also provides a general framework for systematically taking into account higher orders and for including other interactions. In this formulation the necessity of the counter terms furthermore is readily apparent.

4.5.1 Partition Function

In the presence of external sources of polarization $\mathbf{P}(\mathbf{x}, z; \zeta_n)$, Schwinger's free energy for two parallel interfaces is given by Eq.(4.20). The partition function for a flat and a rough interface described by the profile $h(\mathbf{x})$ corresponding to the potential $\mathbf{V}(\zeta, h(\mathbf{x}), z)$ of Eq.(4.28) therefore formally is,

$$
\begin{aligned}
Z_T[\mathbf{P}, h] &= \exp\Big[-\frac{1}{T}(F_T^{\|}(a) + \delta F[h])\Big] \prod_n \exp\Big[-\frac{1}{T}(\mathcal{V}_n[h] + \delta\mathcal{V}_n^h)\Big] \\
&\times \exp\Big[\frac{T}{2}\{\mathbf{P}_n|\mathbf{G}^{\|(n)}|\mathbf{P}_n\}\Big] \qquad (4.76)
\end{aligned}
$$

where $\mathcal{V}_n[h]$ is the functional derivative operator,

$$
\mathcal{V}_n[h] = -\frac{1}{2}\int d\mathbf{x} \int_0^{h(\mathbf{x})} dz \, \frac{\delta}{\delta \mathbf{P}_n(\mathbf{x}, z)} \cdot (\varepsilon(\zeta_n) - \mathbb{1}) \cdot \frac{\delta}{\delta \mathbf{P}_n^{\dagger}(\mathbf{x}, z)} \qquad (4.77)
$$

representing the interaction of the n-th Matsubara mode with the roughness profile $h(\mathbf{x})$.

4.5.2 Counter terms

The counter potential of Eq.(4.57) corresponds to a functional derivative operator of the form,

$$\delta\mathcal{V}_n^h = \frac{1}{2}\int dz \int d\mathbf{x}\frac{\delta}{\delta\mathbf{P}_n(\mathbf{x},z)}\cdot\delta\mathbf{V}^h(\zeta_n,z)\cdot\int d\mathbf{y}\frac{\delta}{\delta\mathbf{P}_n^\dagger(\mathbf{y},z)}\;. \tag{4.78}$$

It corrects for polarization effects due to surface roughness. Note that the counter potential of Eq.(4.57) in Eq.(4.78) has support in the immediate vicinity of the plane at $z = 0$ only and does not depend on the transverse position $\mathbf{x}$ nor on the mean separation a of the two interfaces. The counter potential $\delta\mathbf{V}^h(\zeta)$ ensures that the scattering of electromagnetic waves incident perpendicular to the rough surface is reproduced.

We in addition have to include a counterterm $\delta F[h]$ to the free energy that is a functional of the profile $h(\mathbf{x})$. It is analytic at $h(\mathbf{x}) = 0$ and has the expansion,

$$\begin{aligned}\delta F[h] &= c_0 + \int d\mathbf{x}\; h(\mathbf{x})c_1(a,T) + \frac{1}{2}\iint d\mathbf{x}d\mathbf{y}\; c_2(\mathbf{x}-\mathbf{y})h(\mathbf{x})h(\mathbf{y}) \\ &+ \frac{1}{6}\iiint d\mathbf{x}d\mathbf{y}d\mathbf{z}\; c_3(\mathbf{x}-\mathbf{z},\mathbf{y}-\mathbf{z})h(\mathbf{x})h(\mathbf{y})h(\mathbf{z}) + \ldots\end{aligned} \tag{4.79}$$

with translation-invariant n-point coefficient functions c_n that depend only on transverse coordinate differences. These coefficient functions are used to systematically remove corrections to the correlation functions of the profile $h(x)$ in the presence of electromagnetic interactions. The constant 1-point counter term $c_1(a,T)$ ensures that $\langle h(x)\rangle = 0$ at any separation a and temperature T. $c_1(a,T)$ is the only coefficient that may depend on a and T because its contribution to the free energy in fact vanishes for profiles that satisfy Eq.(4.13). The higher order terms of $\delta F[h]$ are constructed so that connected correlation functions of the profile at $T = 0$ are the prescribed ones when the second flat interface is removed. They do not depend on the temperature T nor on the separation a.

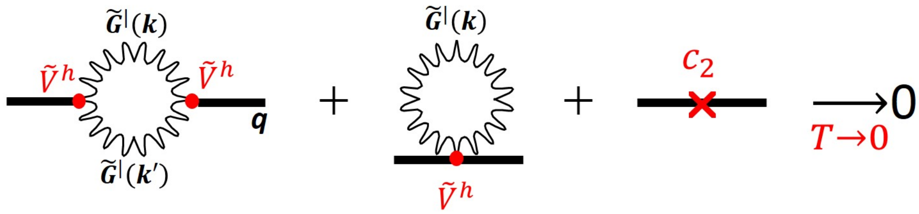

Figure 4.5: One-loop Feynman diagrams for the counter term $c_2(q)$. $c_2(q)$ is determined by demanding that the (prescribed) 2-point roughness correlation of a single plate at $T = 0$ is not corrected. We here consider 1-loop contributions only.

This ensures that,

$$\frac{\partial}{\partial T}\delta F[h] = \frac{\partial}{\partial a}\delta F[h] = 0 \text{ for any profile for which } \int_A d\mathbf{x}h(\mathbf{x}) = 0 \ . \tag{4.80}$$

This counter-term to the free energy therefore does not affect thermodynamic state functions like the enthropy or pressure. It cancels loop contributions to the energy (at $T \to 0$) when the flat interface is removed ($a \to \infty$). The Casimir free energy remains (its finite, a-dependent value at $T = 0$ is the Casimir energy).

In obtaining the Casimir free energy by the Green's function method the contribution to the free energy from the counter term coefficient $c_2(\mathbf{x} - \mathbf{y})$ was implicitly taken into account by subtracting $\Delta F_T[h, \infty]$ in Eq.(4.30). Requiring the absence of one-loop corrections to the 2-point roughness correlation at large separation a and temperature $T = 0$ determines $c_2(\mathbf{q})$. The Feynman diagrams involved in this condition are shown in Fig. 4.5. The counter term c_2 also ensures that there is no single-interface correction to the Casimir energy at $T = 0$. For $T > 0$ a finite a-independent contribution to the single-interface free energy remains that we have not calculated here.

The Green's function approach implicitly also accounted for contributions of $c_1(a, T)$ by simply assuming that Eq.(4.13) holds to order σ^2. $c_1(a, T)$ cancels tadpole contributions to the scattering matrix (see Fig. 4.6) and 1-particle reducible contributions to the Casimir free energy like those of Fig. 4.8 vanish in

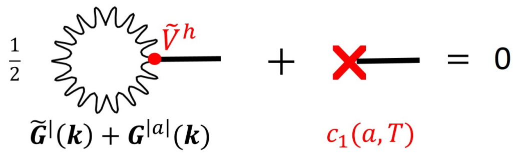

Figure 4.6: Cancellation of tadpoles by the counter term $c_1(a,T)$ at one loop. Summation to all orders of the δ-function contribution to $G^{\|}_{zz}$ replaces $\mathbf{G}^{\|}$ by $\tilde{\mathbf{G}}^{|} + \mathbf{G}^{|a|}$ and $\mathbf{V}^h$ by $\tilde{\mathbf{V}}^h$.

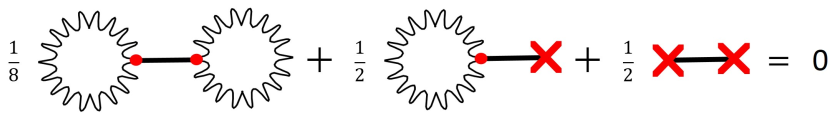

Figure 4.7: 1-particle reducible dumbbell contributions to the free energy that are cancelled by the c_1 counter term given in Eq.(4.81). 1-particle reducible contributions to the free energy are of order $1/T$ at low temperatures and would violate Nernst's theorem.

this case.

We defined the mean separation a by Eq.(4.13) and demanding that corrections to $\langle h_\pm(\mathbf{x})\rangle$ vanish determines $c_1(a,T)$ to one loop. The diagrammatic form of this condition is shown in Fig. 4.6 and evaluates to,

$$
\begin{aligned}
c_1(a,T) = \frac{T}{D(0)} \sum_n \int \frac{d\mathbf{k}}{(2\pi)^2} [& D_{\pm +}(0) \mathrm{Tr} \mathbf{V}_+^{(n)} (\tilde{\mathbf{G}}^{|(n)}_{++}(\mathbf{k}) + \mathbf{G}^{|a|(n)}_{++}(\mathbf{k})) \\
&+ D_{\pm -}(0) \mathrm{Tr} \mathbf{V}_-^{(n)} (\tilde{\mathbf{G}}^{|(n)}_{--} + \mathbf{G}^{|a|(n)}_{--}(\mathbf{k}))] \\
&= c_1(\infty,T) - T \sum_n \int_0^\infty \frac{kdk}{2\pi} \kappa \left(\frac{\bar{r}^2}{e^{2\kappa a} - \bar{r}^2} + \frac{\bar{r}^2}{e^{2\kappa a} - \bar{r}^2} \right) \\
&= c_1(\infty,T) - \frac{\partial}{A\partial a} F_T^{\|}(a) \ ,
\end{aligned} \tag{4.81}
$$

where $c_1(\infty,T)$ is the (infinite) one-interface contribution that does not depend

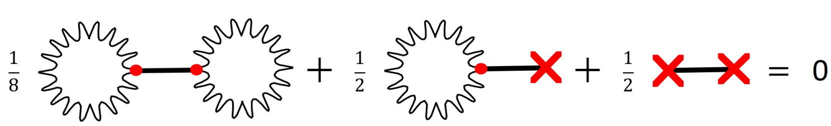

Figure 4.8: 1-particle reducible dumbbell contributions to the free energy that are cancelled by the c_1 counter term given in Eq.(4.81). 1-particle reducible contributions to the free energy are of order $1/T$ at low temperatures and would violate Nernst's theorem.

on the separation a. The interpretation of Eq.(4.81) is straightforward and could have been anticipated: for $\langle h\rangle \neq 0$, the separation a is redefined at one loop. Since

$$F_T^{\|}(a) - \int_A d\mathbf{x} h(\mathbf{x}) \frac{\partial}{A\partial a} F_T^{\|}(a) \approx F_T^{\|}(a - \langle h\rangle) \ . \tag{4.82}$$

To leading order in $\langle h\rangle$, the c_1-counterterm arises from the free energy of two parallel flat interfaces at separation a_B, where $a = a_B + \langle h\rangle$, is the separation at which Eq.(4.13) holds.

The a-independent but temperature-dependent contribution from $c_1(\infty, T)$ similarly is the difference in free energy due to a shift of a flat interface by $-\langle h\rangle$. The bulk contribution to the free energy density thereby increases by,

$$\begin{aligned} c_1(\infty, T) &= -\frac{T}{4} \sum_n \int_0^\infty \frac{kdk}{2\pi} \mathrm{Tr}(V_+^{(n)} \tilde{\mathbf{G}}_{++}^{|(n)}(k) + V_-^{(n)} \tilde{\mathbf{G}}_{--}^{|(n)}(k)) \\ &= -\frac{T}{2} \sum_n (\varepsilon(\zeta_n) - 1) \int_0^\infty \frac{kdk}{2\pi} \left(\frac{\kappa_\varepsilon \kappa - k^2}{\varepsilon\kappa + \kappa_\varepsilon} + \frac{\zeta^2}{\kappa_\varepsilon + \kappa} \right) \\ &= T \sum_n \int_0^\infty \frac{kdk}{2\pi} (\kappa - \kappa_\varepsilon) = \frac{1}{V} (F_T^\gamma[1] - F_T^\gamma[\varepsilon]) \end{aligned} \tag{4.83}$$

where $F_T^\gamma[\varepsilon]/V$ is the free energy density of a photon gas in a homogeneous medium with permittivity $\varepsilon(\zeta)$. The difference in free energy density in the dielectric and in vacuum depends on the permittivity $\varepsilon(\zeta)$. For the plasma model with $\varepsilon(\zeta) = 1 + (\omega_p/\zeta)^2$, this separation-independent contribution to the free energy is,

$$(F_T^\gamma[1] - F_T^\gamma[\varepsilon]) \frac{A\langle h\rangle}{V} = A\langle h\rangle \big[c_1(\infty, 0) - \frac{T^4\pi^2}{45} + \frac{T^2{\omega_p}^2}{\pi^2} \sum_{n=1}^\infty \frac{K_2(n\omega_p/T)}{n^2}\big] \ , \tag{4.84}$$

where the modified Bessel function $K_2(x)$ is normalized to $K_2(x \sim 0) \sim 2/x^2$. The generally infinite constant $c_1(\infty, 0)$ does not depend on temperature nor on the separation a. It is sensitive to the behavior of $\varepsilon(\zeta)$ at energies $\zeta \gg \omega_p$. Estimating this contribution to the free energy in the framework of the low-energy effective theory is meaningless since the loop integral is dominated by momenta and energies $k, \zeta \gg \omega_p$. For the sake of completeness, this formal contribution with a proper time cutoff β is,

$$c_1(a \sim \infty, T=0) = -\frac{1}{16\pi^2}\int_\beta^\infty \frac{d\lambda}{\lambda^3}(1-e^{-\lambda\omega_p{}^2}) \; . \tag{4.85}$$

It is a quadratically and logarithmically UV-divergent constant contribution to the total energy of the system. It is canceled by the counter term c_0 and has no physical implications.

4.5.3 The Complete Low-Energy Effective Field Theory

Since the Greens-function $\mathbf{G}^{\|}$ of parallel interfaces as well as the counter terms are invariant under transverse translations, the partition function $Z_T(\mathbf{P}=0,h)$ defined in Eq.(4.76) for vanishing polarization sources is a functional of the roughness profile $h(\mathbf{x})$ with translation-invariant coefficients. We thus can use Eq.(2.50) to evaluate it in terms of correlation functions of the profile $h(\mathbf{x})$ rather than the profile itself. We have that,

$$Z_T[\vec{P}=0,h] = Z_T[\vec{P}=0,\frac{\delta}{\delta\alpha}]\; Z_h[\alpha]|_{\alpha=0} \, , \tag{4.86}$$

with $Z_\alpha[h]$ defined by Eq.(2.44). The complete generating functional of the Gaussian model we are considering thus is,

$$\begin{aligned} \mathcal{Z}_T[\vec{P},\alpha] \;&:=\; \exp\Big[-\frac{1}{T}(F_T^{\|}(a)+\delta F[\delta/\delta\alpha])\Big]\prod_n \exp\Big[-\frac{1}{T}(\mathcal{V}_n[\delta/\delta\alpha]+\delta\mathcal{V}_n^h)\Big] \\ &\times\; \exp\Big[\frac{T}{2}\{\mathbf{P}_n|\mathbf{G}^{\|(n)}|\mathbf{P}_n\}+\frac{1}{2}(\alpha|D_2|\alpha)\Big] \, , \end{aligned} \tag{4.87}$$

with $(\alpha|D_2|\alpha)$ given by Eq.(2.46). The partition function of Eq.(4.86) is just $\mathcal{Z}_T[\vec{P}=0,\alpha=0]$. From the point of view of Euclidean field theory, Eq.(4.87) promotes the roughness profile $h(\mathbf{x})$ to a field on a two-dimensional (planar) subspace that is coupled to a vector field in $\mathbb{R}^3\times S_1$. Correlation functions of $h(\mathbf{x})$ are obtained by functional differentiation of Eq.(4.87) with respect to the scalar source α and $\mathcal{Z}$ defines the loop-expansion in the usual manner. The main difference to ordinary field theory is that all correlation functions of $h(\mathbf{x})$ are prescribed and counter-functions enforce the absence of any corrections to them at $T = 0$ and $a \sim \infty$. The low energy effective field theory encoded by Eq.(4.87) evidently is not renormalizable – new counter terms (functions) are required at each order of the loop expansion. The three counterterms c_1, c_2 of $\delta F[h]$ and $\delta \mathbf{V}^h$ suffice at the 1-loop level since only the connected two-point functions and $\langle h \rangle$ are superficially UV-dominated if $D_2(0) = \sigma^2$ is finite.

Instead of employing the Green's function approach, one can derive the loop corrections to the free energy from Eq.(4.87). The Casimir free energy to one loop is the same in both approaches. However, the generating functional Eq.(4.87) of the low-energy effective theory has conceptual and methodical advantages: once the set of counter-terms is determined, the field theory yields consistent low-energy results not just for the Casimir energy, but for the scattering matrix as well. No ad-hoc arguments and procedures are required to cancel uncontrolled high-energy loop corrections and the necessity of the counter terms and their interpretation is readily apparent.

4.6 Numerical Investigations

We numerically investigated the correction $\Delta F_T^{\mathrm{Cas}}(a)$ to the Casimir free energy due to the roughness of one of the interfaces. To order σ^2 the correction in Eq.(4.58) is linear in the roughness correlation function and one may define [3] a response function $R_T(q, a)$,

$$\Delta F_T^{\mathrm{Cas}}(a) = \int_0^\infty \frac{q dq}{2\pi} R_T(q, a) D(q) \ , \tag{4.88}$$

that does not depend on the roughness correlation function $D(q)$. Analytical expressions for $R_T(q, a)$ are obtained by changing the integration variable from

$\mathbf{k}'$ to $\mathbf{q} = \mathbf{k}' - \mathbf{k}$ in Eq.(4.59), Eq.(4.62), Eq.(4.66) and Eq.(4.64). The corresponding expressions are given in App. **??**. For clarity and to compare with earlier investigations, we in the following present numerical results at $T = 0$ only. Temperature corrections are sizable only when $2\pi aT \gtrsim 1$. For gold surfaces at 300^oK, temperature corrections become important at separations of the order of microns - a distance at which perturbative roughness is irrelevant.

4.6.1 The Response with and without Counter Term

Fig. 4.9 gives the normalized response as a funnction of the dimensionless variable q/ω_p when the counterterm of Eq.(4.66) is omitted. The low-energy theory is justified in the shaded momentum region $q/\omega_p < 1$. Note the linear rise of the low-energy response function for all separations a in the uncontrolled region $q/\omega_p \gg 1$. The integration weight $qD(q)$ for Gaussian and exponential roughness correlation with a typical correlation length $l_c \sim 1/\omega_p$ is superimposed. A sizable contribution to the roughness correction in Eq.(4.88) evidently is due to loop momenta $q > \omega_p$ for which the low-energy expressions are unreliable.

Inclusion of the counter potential gives a constant high-momentum response. Fig. 4.10 shows the response functions with and without the counterterm contribution of Eq.(4.66). With the same model for the bulk permittivity of gold, the response function shown in Fig. 3 of Ref. [3] is reproduced when the counter-potential is omitted. Inclusion of the counter potential gives a constant high-momentum response and the correction to the Casimir (free) energy is of order σ^2. Note that with $g^2 = 1$ the response at $q = 0$ does not change.

The correction to the Casimir energy at $T = 0$ for Gaussian roughness with and without inclusion of the counter term of Eq.(4.66) is shown in Fig. 4.11. Whereas the PFA-limit $l_c \to \infty$ coincides for both cases, the behavior is remarkably different at finite l_c. Including the counter term of Eq.(4.66) the roughness

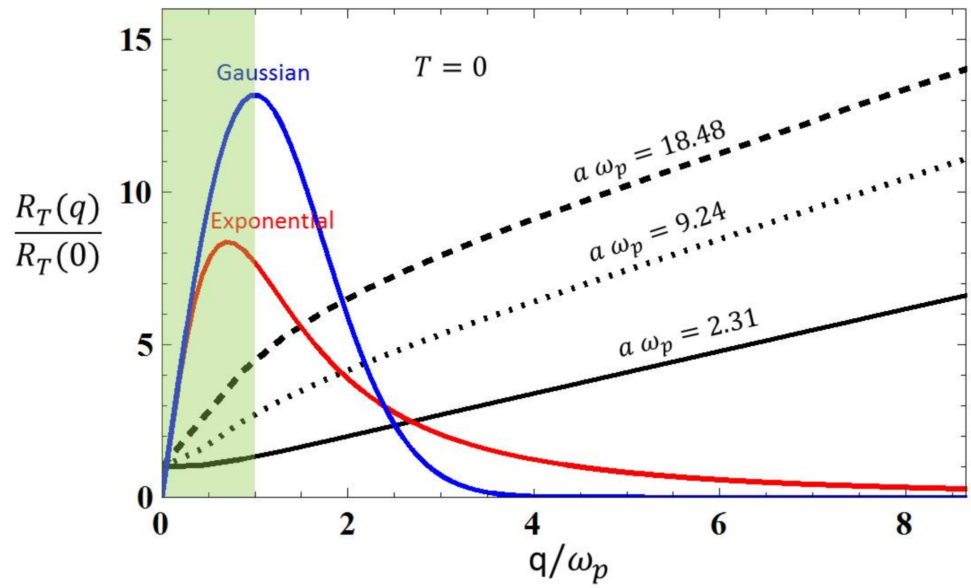

Figure 4.9: The dimensionless normalized response $\rho(q,a) = R_T(q,a)/R_T(0,a)$ without counter potential $\delta\mathbf{V}^h = 0$ for the permittivity $\varepsilon(\zeta) = 1 + (\omega_p/\zeta)^2$ to leading order in σ^2 at $T = 0$. The dependence on q/ω_p of this ratio of the roughness response function $R_T(q,a)$ (defined by Eq.(4.88)) is shown for $a\omega_p = 18.48(--), 9.24(\cdots\cdots)$ and $2.31(\text{——})$. For the plasma frequency $\omega_p = \omega_p(\text{Au}) \sim 0.046\text{nm}^{-1}$, this normalized response without counter potential is identical with that obtained by Ref. [3]. [For $\omega_p = 0.046\text{nm}^{-1}$ the curves here corresponds to those of Fig. 4 in Ref. [3] at separations $a = 200, 100,$ and 50nm.] Note the change in behavior and subsequent linear rise in the region $q\omega_p \gtrsim 1$. The region $q\omega_p \lesssim 1$ where the effective low-energy theory is valid is shaded light green. We superimpose typical integration densities for the response function in Eq.(4.88): the momentum space function $qD(q)$ for Gaussian and exponential 2-point roughness correlation with $l_c = 1/\omega_p$. The roughness correction to the Casimir energy with exponential correlation diverges logarithmically and even for Gaussian roughness correlation the (unshaded) region $q/\omega_p > 1$ contributes significantly in this uncorrected case. Note that for a gold surface the correlation length here is $l_c = 1/\omega_p(\text{Au}) \sim 21\text{nm}$.

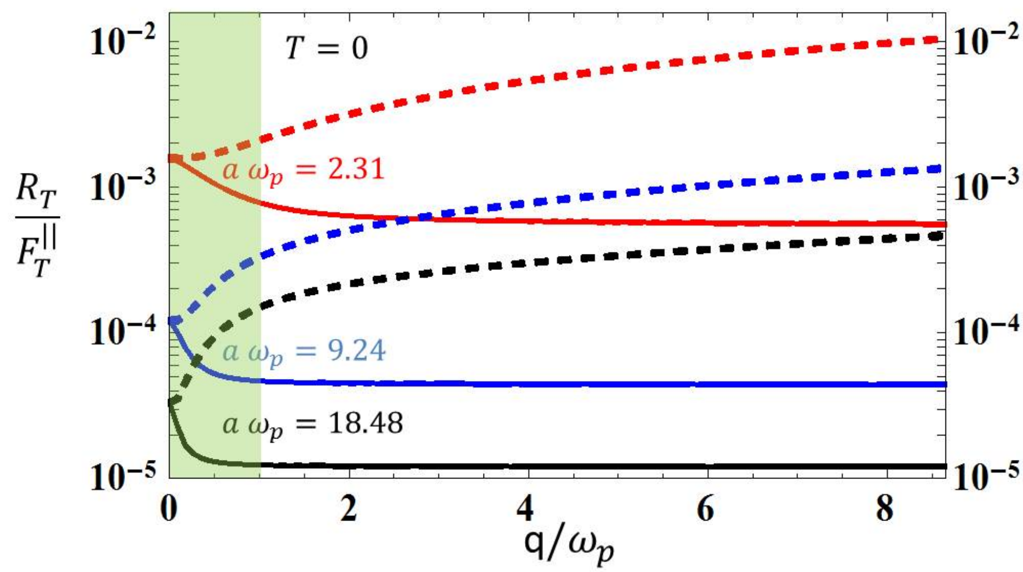

Figure 4.10: (Color online) The ratio $R_T(q,a)/F_T^{\|}(a)$ of the roughness response function to the Casimir energy of flat parallel plates at $T = 0$ with (solid) and without (dashed) counter potential $\delta\mathbf{V}^h$ with $g^2 = 1$. The permittivity $\varepsilon(\zeta) = 1 + (\omega_p/\zeta)^2$ is characterized by the plasma frequency ω_p. The dependence on q/ω_p of the ratio is shown for $a\omega_p = 2.31$(top,red), 9.24(middle,blue) and 18.48(bottom,black). For $\omega_p = 0.046\text{nm}^{-1} \sim \omega_p(\text{Au})$ the normalized response without counter potential (dashed) is identical with that of Fig. 3 in Ref. [3] at separations of $a = 50, 100$, and 200nm. Note that the renormalized roughness response is monotonically decreasing and approaches a constant at large momenta that is a factor of 2-3 smaller than the response at $q = 0$. Most of the correction to the Casimir energy in this case arises from the shaded integration region $q/\omega_p < 1$ where the low-energy description is valid.

correction to the Casimir energy *decreases* in magnitude for decreasing correlation length and approaches a finite (uncorrelated) limit for $l_c \to 0$. Roughness increases the Casimir force but the PFA is an upper bound in this case. The ratio of the roughness correction to the PFA furthermore approaches a constant, l_c-dependent, value with increasing separation rather than increasing indefinitely as in the unsubtracted case (for exponential roughness, the roughness correction without the counter term of Eq.(4.66) would diverge at any separation and for all l_c). Let us also note that for $l_c \lesssim 1/\omega_p$ the roughness correction at large separations is less than 50% of the PFA prediction. Although we here are considering only perturbative roughness corrections, the suppression at large separations for $l_c \lesssim 1/\omega_p$ is of a similar magnitude as that observed [86] for machined profiles with correlation length $l_c \sim 1/\omega_p$.

4.6.2 (In)sensitivity on High Momentum Components of the Roughness Correlation

The counter potential $\delta\mathbf{V}^h$ was introduced to correct for uncontrolled high momentum contributions to loop integrals with the help of phenomenological input. We therefore investigated the sensitivity of the roughness correction to the correlation function $D(q)$ numerically. Fig. 4.12 shows the ratio of the correction for Gaussian- and for exponential- roughness of the same correlation length l_c. The two are identical for $l_c = 0$ and $l_c \sim \infty$ (PFA) at any $a\omega_p$. The (dimensionless) ratio of these corrections never drops below 85% for any separation $a\omega_p$ and correlation length $l_c\omega_p$. Without counter potential this ratio is infinite. Exponential roughness always gives a smaller correction than Gaussian roughness of the same correlation length and variance. The two correlation functions provide rather similar descriptions of low energy scattering and the low-energy effective theory

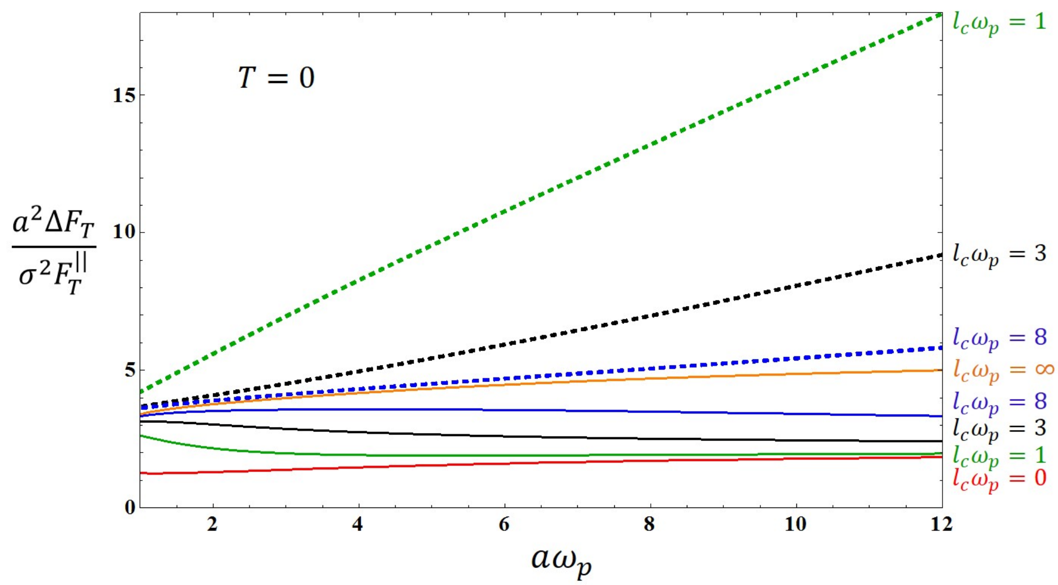

Figure 4.11: (Color online) The dimensionless ratio $(a^2/\sigma^2)\Delta F_T^{\mathrm{Cas}}(a)/F_T^{\|}(a)$ of the roughness correction to the Casimir energy of two parallel flat interfaces at $T = 0$. The calculation is to leading order in σ^2/a^2 for a plasma-model permittivity with plasma frequency ω_p for Gaussian roughness with correlation length l_c. Dashed curves give the ratio as a function of $a\omega_p$ without the counter term contribution of Eq.(4.66) whereas solid curves give the ratio when this counter term with $g^2 = 1$ is included. Curves of the same color correspond to the same value of $l_c\omega_p$. From the top: $l_c\omega_p = 1$ (green, dashed), 3 (black,dashed), 8 (blue,dashed), ∞ (orange), 8 (blue,solid), 3 (black,solid), 1(green,solid) and 0 (red,solid). Note that the $l_c \to 0$ curve (red) is a lower bound that exists only in the renormalized case. The counter term vanishes in the PFA limit $l_c \to \infty$ (orange), and this limit is the same for both. Whereas the PFA is an upper bound for the magnitude of the roughness correction when the counter potential is included, it is a lower bound without. The ratio of the roughness correction to the PFA at finite l_c approaches a finite value at large separations when the counter term is included whereas it otherwise increases indefinitely. The roughness correction in the subtracted case at large separations is less than 50% of the PFA-prediction when $l_c \lesssim 1/\omega_p$. Except for $l_c = 0$, the roughness correction approaches the PFA estimate at sufficiently small separation, but it quickly decreases and approaches the lower bound for $l_c\omega_p < 1$.

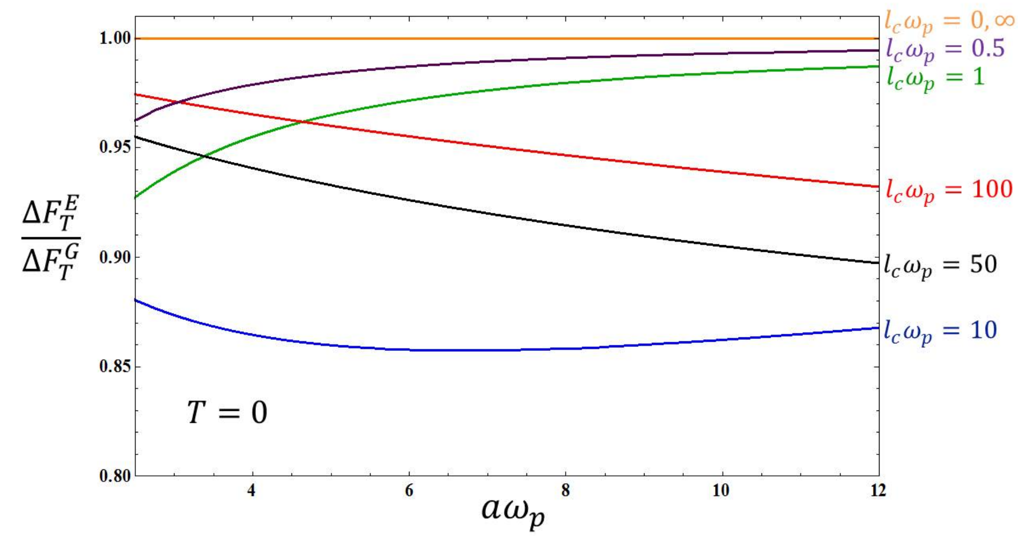

Figure 4.12: (Color online) The dimensionless ratio $\Delta F_T^E(a)/\Delta F_T^G(a)$ of the roughness correction to the Casimir energy for exponential(E) and Gaussian(G) roughness with the same correlation length $l_c\omega_p$ as a function of the dimensionless separation $a\omega_p$. $g^2 = 1$ and a plasma-model permittivity characterized by the single plasma frequency ω_p was assumed. The roughness correlation functions are those of Eq.(4.49)(E) and Eq.(4.46)(G). In the PFA ($l_c \to \infty$) and uncorrelated ($l_c \to 0$) limits the corrections coincide but differ by up to 15% at some separations. For the same variance σ^2 and correlation length l_c, the roughness correction with exponential correlation is always smaller than with Gaussian correlation. Note that the two types of roughness correlation approach the PFA quite differently: at large separations the corrections still differ by over 5% even for $l_c\omega_p \sim 100$.

with counter potential depends only weakly on their (very different) behavior at high momenta.

4.6.3 Comparison with Experiment

The low energy theory for electromagnetic interactions with rough surfaces ultimately must be compared to experiment. Unfortunately only very few studies are dedicated to the systematic investigation of Casimir forces between rough surfaces. Many employ non-isotropic machined surfaces with rather large σ/a-ratios[73, 86] that are not accessible perturbatively. Nevertheless, these experiments qualitatively contradict the predictions of exact calculations, that essentially any kind of roughness tends to increase the Casimir force above the PFA estimate. A notable exception is a series of investigations of isotropically rough surfaces by Palasantzas et al.[50, 51, 4]. For sufficiently rough surfaces, this group does observe (see Fig. 3 of Ref. [4]) an increase of the Casimir force by 200-400% at small separations. This sharp increase in the force was attributed to particularly high islands of the surface profile that can also be seen in some of the AFM scans of the gold surfaces. The pronounced effect of such islands is beyond the scope of a perturbative analysis and was explained by a semi-empirical approach [52] based on the PFA.

However, gold films with 100nm and 200nm thickness of relatively low roughness appear to be almost free of such buildup effects. At small separations the force in these cases is smaller than the PFA prediction. In Fig. 4.13 we compare the low-energy theory to the measurements of Ref. [4] on these thin films. The experiments measure the force between a gold-coated sphere and a gold-coated plate. Both surfaces are rough, but their profiles are uncorrelated. For two parallel rough gold-coated plates the correction to the Casimir energy to leading order in σ/a is that for a single rough plate with a roughness correlation that is the sum of the roughness correlations functions of the sphere and the flat plate,

$$D(q) = D^{\text{plate}}(q) + D^{\text{sphere}}(q) \ . \tag{4.89}$$

We use Derjaguin's PFA approximation[87] to correct for the curvature of the sphere of radius $R = 100\mu\text{m} \gg a$. The force $f_T(a)$ at temperature T between the sphere and a plate with (closest) separation a in this approximation is,

$$f_T(a) = 2\pi R F_T^{\text{Cas}}[a]/A \ , \tag{4.90}$$

where $F_T^{\text{Cas}}[a]/A$ is the Casimir free energy per unit area (not the pressure) of two parallel rough plates. Due to the large radius of the sphere, this is an excellent approximation for separations $a < 200\text{nm} \sim R/500$. Fig. 4.13a gives the ratio $\rho(a)$ of this force to the Casimir energy per unit area $F_T^{\|}[a]/A$ of two *flat* parallel gold plates with separation a,

$$\rho(a) := \frac{f_T(a)A}{2\pi R F_T^{\|}[a]} = \frac{F_T^{\text{Cas}}[a]}{F_T^{\|}[a]} = 1 + \frac{\Delta F_T^{\text{Cas}}[a]}{F_T^{\|}[a]} \;, \tag{4.91}$$

at $T = 0$. The experimental Casimir force for the rough sphere and plate at separations $\sigma \ll a < l_c$ is up to 30% greater than the Casimir energy for flat plates.

Since we do not differentiate between contributions from high and low peaks of the roughness profile and only use a single correlation function, all standard deviations of Ref. [4] were multiplied by a factor of 1.7. We used $\sigma^{\text{Sph}} = 8\text{nm}$, $\sigma^{100} = 2.6\text{nm}$ and $\sigma^{200} = 4.3\text{nm}$ for the coatings of the sphere, 100nm and 200nm thick films respectively. These standard deviations also approximately correspond to those estimated from the AFM-scans of these surfaces (see Fig. 1 in Ref. [4]). The correlation lengths $l_c^{\text{Sph}} = 33\text{nm}$, $l_c^{100} = 21\text{nm}$ and $l_c^{200} = 25\text{nm}$ are those of Ref. [4]. The ratio $\rho(a)$ for the 200nm thick film is well reproduced by the low-energy theory with exponential as well as with Gaussian correlations. We only show the result for exponential roughness in Fig. 4.13, but the fit for Gaussian roughness is of similar quality. For comparison we show the roughness correction in PFA for the same standard deviations.

The ratio $\rho(a)$ is close to unity at larger separations $100\text{nm} < a < 150\text{nm}$ where roughness corrections are relatively small. While this on average is approximately observed for the 200nm film, the ratio for the 100nm film is systematically about 6% above unity at larger distances. To correct for this (unexplained) discrepancy we multiplied the force observed on the 100nm thick film by 0.94 before[8] comparing with theory.

From a practical point of view the comparison in Fig. 4.13b with the Casimir energy of two parallel flat plates at a slightly smaller separation $a_{\text{eff}} = a - \delta a$ perhaps is more useful. The Drude-model permittivity describing reflection off these effective flat plates in Ref. [4] was obtained from ellipsometric measurements on the rough surfaces. We merely adjusted δa for the best fit. Fig. 4.13b shows that effective flat surfaces at a reduced separation $a - \delta a$ reproduce the low-roughness data remarkably well. (The force data of the 100nm film was multiplied by the same correction factor of 0.94 as in the graph of Fig. 4.13a.) Since ellipsometric measurements on thin films are quite standard, this observation essentially reduces low-roughness corrections to Casimir energies to a determination of the optimal shift δa. Instead of measuring the absolute average distance between the profiles of two rough surfaces (in itself a delicate procedure that involves a number of corrections), we suggest that precision Casimir studies with low-roughness surfaces simply determine an *effective* separation for flat plates with the measured (perpendicular) reflection coefficients. Fig. 4.13b is evidence that the data at small separations robustly determines this distance to better than 1nm, at the same time all but eliminating the need for roughness corrections.

[8]While this correction factor is *ad hoc*, we would like to point out that the ratios of Fig. 4.13 are less forgiving than logarithmic depictions of the data. The experimental error probably increases sharply at larger separations simply because the force is rapidly decreasing in magnitude.

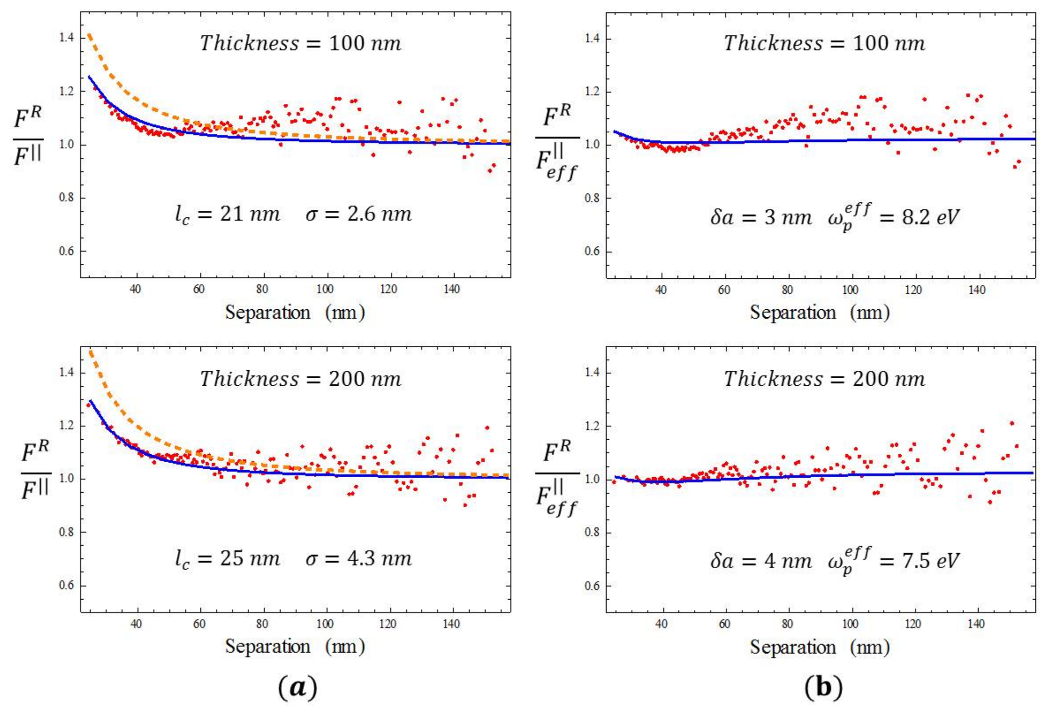

Figure 4.13: The dimensionless ratio $\rho(a)$ defined in Eq.(4.91) of the Casimir force between a rough gold-coated sphere and a rough gold-coated plate to the Casimir energy between dielectric flat plates. The experimental data is from Ref. [4]. The thickness of the gold coating on the flat plate is 100nm (upper graphs) and 200nm (lower graphs). An exponential roughness correlation and a Drude parametrization of the permittivity is assumed. The standard deviation and correlation length for the sphere's profile is $\sigma^{\mathrm{Sph}} \sim 8$nm and $l_c^{Sph} \sim 33$nm. a) The ratio of the force on the rough plate to the Casimir force between a gold-coated flat plate and a smooth sphere at the same mean separation. A Drude parametrization of the permittivity with $\omega_p = 9$eV, $\gamma = 0.045$eV was used. (Red) dots is the ratio for experimental data of Ref. [4]. The measured force on the 100nm thick plate was multiplied by a correction factor of 0.94 (see text for details). The solid (blue) line is our best theoretical fit to this ratio with the indicated parameters for the roughness correlation function of the plate in Eq.(4.89). Note that the $\sim 30\%$ enhancement at separations $a \sim 20$nm is well reproduced for both films. The dashed line is the PFA result for the same total variance. b) The ratio of the force on the rough plate to that between a smooth sphere and a flat plate at the separation $a - \delta a$. The indicated $\omega_{p_{\mathrm{eff}}}$ for the effective permittivity of the flat plate was obtained from ellipsometric measurements [4] on the rough ones. We assumed the same effective plasma frequency $\omega_{p_{\mathrm{eff}}}^{\mathrm{Sph}} = 7.5$eV for the sphere as for the (similarly rough) 200nm film. The solid (blue) line gives the ratio to the force on the effective flat plate and sphere for the same force including the roughness corrections shown in a).

Chapter 5
Summary and Conclusions

5.1 Roughness Corrections to the Casimir energy in the Scalar Model

In chapter 3., we developed a field theoretical description of the Casimir free energy for a massless scalar field in the presence of a rough and a smooth parallel semi-transparent δ-function plate. Changes in the free energy due to the interaction of the scalar with the rough surface were found to be described by an effective $2+1$-dimensional field theory on an equivalent plane involving two dynamical surface fields, ψ and $\tilde{\psi}$ as well as the static profile h. The model on this planar boundary of the original space is holographic in that the existence of another dimension and of a second parallel plate at a separation a are encoded in its non-local propagators. The theory in this sense is a low-dimensional analog of brane models in string theory [67, 68, 69].

Two-loop contributions to the free energy of this model give the leading roughness correction. For a massless scalar field this correction is qualitatively similar to that for electromagnetic fields obtained by perturbative analysis [88, 89, 90, 91, 92, 50], but the field theoretic origin allows for a consistent inclusion of finite temperature effects and for a more transparent interpretation. In the strong coupling (Dirichlet) limit, the leading 2-loop correction is given by Eq.(3.50) and is shown in fig. 3.5. As for the electrodynamic corrections considered in [90, 91, 92, 50, 51, 75], the PFA result [72, 16] is reproduced for $a \ll \ell$ and the

Casimir force appears to strengthen with decreasing ℓ/a. From the point of view of the multiple-scattering expansion of the Casimir energy, this strengthening of the force is not intuitive and in fact violates unitarity when $a \gg \ell$.

In the scalar model, we found that the problem could be traced to an inappropriate choice of the equivalent planar surface for a rough plate. This plane does not coincide with the mean of the profile but is displaced a distance $\rho \propto \sigma^2/\ell$ from it. For this improved definition of the effective surface, roughness corrections are much smaller and the Casimir force *weakens* with increasing roughness σ^2/ℓ. Roughness strengthens the Casimir force only for $\sigma/\ell \lesssim 0.5$ and only for $a \lesssim 4\ell$. In this regime our unitarity argument based on transverse translational symmetry does not hold. In terms of the effective absolute separation, the PFA to the roughness correction is approached from below with increasing correlation length. As pointed out at the end of Sect. 3.4 it should be possible to intrinsically calibrate experimental results to the effective absolute separation and take advantage of the smaller roughness corrections.

We further derived an effective low energy field theory in the limit $a \gg \ell$ that depends on a single length parameter $\rho \sim \sigma^2/\ell$ characterizing the roughness of a plate. The correction in this limit is described by an effective scattering matrix t_{rough}, given in Eq.(3.66), for a scattering plane displaced a distance $\rho/2$ from the mean of the profile. As illustrated by fig. 5.1, roughness weakens the force at all separations in the effective low energy theory and the reflection coefficient is always less than for a flat plate of the same material, approaching that of a flat plate at long wavelengths $1/\kappa \gg \rho$. It is also evident from fig. 5.1 that the 2-loop estimate in terms of the effective absolute separation interpolates between the low energy effective model and the PFA, approaching the former for small and the latter for large correlation length ℓ. At common correlation lengths and variances of the profile, the roughness correction at separations of $a_{\text{eff}} \sim 100$nm

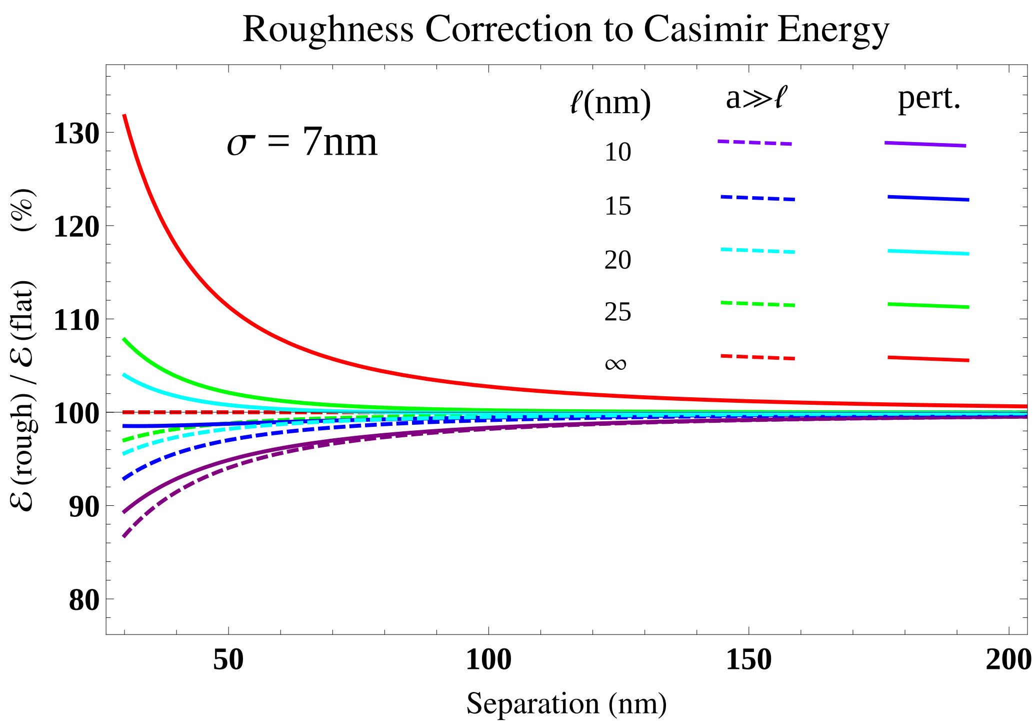

Figure 5.1: (color online) Relative roughness corrections to the Casimir energy in % due to a scalar satisfying Dirichlet boundary conditions on two plates, one of which is flat. The profile of the other is characterized by its variance $\sigma^2 = 49\text{nm}^2$ and correlation length ℓ. The separation is between equivalent planes representing the plates (see the text and Eq.(3.53) for its relation to the mean separation.) The leading two-loop approximation for different correlation lengths ℓ is given by solid curves that correspond to those of fig. 3.5. Dashed curves represent the correction in the effective low energy theory derived in the limit $a \gg \ell$. Pairs of dashed and solid curves of the same color correspond to the same correlation length $\ell = 10\text{nm}$ (violet), 15nm (blue), 20nm (cyan), 25nm (green) and $\ell = \infty$ (red). The leading two-loop approximation interpolates between the low-energy model for large separations $a \gg \ell$ and the PFA result (solid red) for small separations $a \lesssim \ell$. Note that typical roughness corrections are much smaller than the PFA suggests.

for a scalar field satisfying Dirichlet boundary conditions is just a few percent. It is even less for semitransparent materials.

5.2 Roughness Corrections in Electromagnetic Model

We also obtained roughness corrections to low-energy scattering and the Casimir free energy in the framework of Schwinger's effective field theory for dielectrics. The energy scale in this theory is the plasma frequency $\omega_p \sim 0.046\text{nm}^{-1} \sim 9\text{eV}$ of typical materials like gold. We found that roughness corrections generally include large contributions from high momentum excitations. Evaluating their contribution in the low-energy framework is inconsistent and notoriously unreliable. We emphasize that this is not a limitation of the perturbative description; exact (numerical) calculations in the framework of a model also are only as accurate as the model itself. The Casimir energy of short-wavelength periodic rectangular profiles for instance involves momenta at which a description in terms of the bulk permittivity of the material breaks down and the mathematically exact analysis of such a model leads to physically erroneous and unacceptable conclusions. Using the bulk permittivity to describe scattering off profiles structures on the order of the plasma wavelength or smaller (about 137nm for gold) is not justified. Effects due to roughness on the scale of the plasma frequency generally are grossly overestimated by the uncorrected low-energy theory. This has been experimentally verified for machined profiles with a period $\lambda \lesssim 2\pi/\omega_p$: the exact calculations [93, 94] for such profiles tend to overestimate the observed [86] Casimir force by factors of 2-3.

In the second part of this thesis I presented a perturbative analysis of roughness corrections based on the low-energy effective field theory of Schwinger and includes counter terms to correct for uncontrolled high-momentum contributions.

The counter terms subtracts high-momentum contributions to loop integrals at the cost of phenomenological input. Apart from correlations of the roughness profile itself, we in addition modeled the averaged single-interface scattering matrix at vanishing transverse momentum by the plasmon contribution. To leading order in the roughness variance σ^2 this semi-empirical ansatz depends on a single coupling constant g^2. Consistency of the low-energy theory and the existence of an ideal metal limit at any correlation length constrains this dimensionless coupling to $g^2 = 1$ at low energies (see Sec. 4.4.3). The resulting low-energy theory is free of high-momentum contributions to one-loop integrals, approaches the PFA for $l_c \sim \infty$ and has a finite ideal metal limit for any l_c. It is relatively insensitive to the high-momentum behavior of the roughness correlation function and has a drastically different, but physically acceptable dependence on l_c than the uncorrected model. Instead of large (infinite) differences, roughness correlation functions that differ only at high momenta now give similar low-energy predictions. Decreasing the correlation length of the roughness profile no longer increases the Casimir force (indefinitely). Instead the magnitude of the force decreases with decreasing correlation length and approaches a finite lower bound for uncorrelated roughness.

Although the coupling g^2 of the plasmon contribution to the counter-term potential Eq.(4.57) was constrained to $g^2 = 1$ by selfconsistency and the existence of certain limits of the effective low-energy theory, this nevertheless is only a *model* for the roughness contribution to the average scattering matrix at low transverse momenta. It would be phenomenologically preferable to instead parameterize empirical data for this component of the scattering matrix. However, there is some evidence that surface plasmons describe low-energy scattering due to roughness reasonably well. In this sense the model for the leading roughness correction is phenomenologically reasonable apart from being relatively simple and consistent with the low energy theory.

Interestingly the PFA is accurate at small separations for $l_c \gtrsim 1/\omega_p$ only. At large separations it can overestimate the correction to the force by up to 250% (see Fig. 4.11). For $l_c \lesssim 1/\omega_p$ the roughness correction to the Casimir energy is significantly (a factor $\sim 1/2{-}1/3$) below the PFA prediction at all but the smallest separations. The ratio remains approximately constant for $a \sim \infty$ and does not increase with increasing separation as in the uncorrected model. Although we considered only isotropic roughness profiles in the perturbative regime, it perhaps is interesting that the reduction of the correction compared to the PFA prediction by a factor of 2 for $l_c \sim 1/\omega_p$ is of the same order of magnitude as the experimental reduction in the overall force observed [86] by experiments with corrugated rectangular wave profiles.

The Casimir energy of low-roughness profiles was found to be essentially that of flat plates with the *measured* reflection coefficients of the rough one at separations that are slightly smaller than the mean separation of the interfaces. The change in separation is less than the standard deviation of the rough profile. Although the precise value of this shift depends on properties of the profile, this observation enables one to empirically correct for (low-level) roughness and accurately calibrate the effective separation in the plate-sphere geometry.

For conceptual reasons we here derived all expressions for the Casimir free energy at finite temperature, but only investigated implications of this theory at $T = 0$. We intend to extend the numerical investigations to finite temperature in the future. Although the roughness correction at finite temperature is not expected to change at small separations, the regime $1 < a/l_c < aT$ where temperature and roughness corrections are of similar importance could be of some interest. Here we note only that the summands in all expressions at finite temperature are finite in the limit $\zeta \to 0$ for any reasonable permittivity function of metal (Drude- and plasma-model).

Bibliography

[1] J. A. Ogilvy and J. R. Foster. *J. Phys. D*, Appl. Phys. 22:1243–1251, 1989.

[2] J. Daillant and A. Gibaud. Springer, 1999.

[3] P. A. M. Neto, A. Lambrecht, and S. Reynaud. *Phys. Rev. A*, 72:012115, Jul 2005.

[4] P. J. van Zwol, G. Palasantzas, and J. Th. M. De Hosson. *Phys. Rev. B*, 77:075412, Feb 2008.

[5] H. B. G. Casimir. *Kon. Ned. Akad. Wetensch. Proc.*, 51:793, 1948.

[6] S. K. Lamoreaux. *Phys. Rev. Lett.*, 78:5–8, Jan 1997.

[7] R. Eisenschitz and F. London. *Z. Physik*, 60:491–527, 1930.

[8] F. London. *Z. Physik*, 63:245–279, 1930.

[9] J.D. Van der Waals. *Nobel Lectures in Physics*, 254 - 265., 1910.

[10] E. J. M. Verwey and J. T. G Overbeek. *J Chem Soc, Faraday Trans.*, 42A-B:117–123, 1946.

[11] Martin Schaden and Larry Spruch. *Phys. Rev. A*, 58:935–953, Aug 1998.

[12] H. B. G. Casimir and D. Polder. *Phys. Rev.*, 73:360–372, 1948.

[13] J. Gomis and S. Weinberg. *Nuclear Physics B*, 469(3):473 – 487, 1996.

[14] P. Greiner and Arch. Ration. *Mech. Anal*, 41:163, 1971.

[15] P. B. Gilkey. CRC Press, Boca Raton, 1995.

[16] M. Bordag, G. L. Klimchitskaya, U. Mohideen, and V. M. Mostepanenko. Oxford Univ. Press, New York, 2009.

[17] M. Schaden. *Phys. Rev. Lett.*, 102:060402, 2009.

[18] E. A. Power. Elsevier, New York, 1964.

[19] N. F. Svaiter and B. F. Svaiter. *J. Phys. A*, 25:979, 1992.

[20] K. V. Shajesh and M. Schaden. *Phys. Rev. D*, 83(12):125032, 2011.

[21] M. Schaden. *Europhys. Lett.*, 94:41001, 2011.

[22] O. Kenneth and I. Klich. *Phys. Rev. Lett.*, 97:160401, 2006.

[23] E.M. Lifshitz. Zh. Eksp. Teor. Fiz., 29:94–110, 1956.

[24] E.M. Lifshitz. *Soviet Physics JETP-USSR*, 2(1):73 – 83, 1956.

[25] J. Schwinger, L. L DeRaad, and K. Milton. *Annals of Phys.*, 115(1):1–23, Sep 1978.

[26] H. B. G. Casimir. *Physica*, 19:846, 1953.

[27] T. H. Boyer. *Phys. Rev.*, 174:1764–1774, 1968.

[28] R. Balian and B. Duplantier. *Ann. Phys. (NY)*, 104:300–335, 1977.

[29] L. L. DeRaad and K. A. Milton. *Ann. Phys.*, 136:229–242, 1981.

[30] E. K. Abalo, K. A. Milton, and L. Kaplan. *Phys. Rev. D*, 82:125007, 2010.

[31] W. Lukosz. *Physica*, 56:109–120, 1971.

[32] J. Ambjorn and S. Wolfram. *Ann. Phys. (NY)*, 147:1–56, 1983.

[33] I. Brevik and M. Lygren. *Annals of Physics*, 251:157–179, 1996.

[34] I. Brevik, M. Lygren, and Marachevsky V. N. *Annals of Physics*, 267:134–142, 1998.

[35] I. Brevik and Pettersen K. *Annals of Physics*, 291:267–275, 2001.

[36] K. Kirsten. Chapman & Hall/CRC Press, Boca Raton, 2002.

[37] S. A. Fulling. *J. Phys. A*, 36:6857–6873, 2003.

[38] R. Balian and B. Duplantier. *Ann. Phys. (NY)*, 112(1):165 – 208, 1978.

[39] H. Gies, K. Langfeld, and L. Moyaerts. *JHEP*, 2003(06):018, 2003.

[40] M. Schaden. *Phys. Rev. A*, 73:042102, Apr 2006.

[41] M. Y. Sparnaay. *Physica*, 24:751, 1958.

[42] U. Mohideen and A. Roy. *Phys. Rev. Lett.*, 81(21):4549–4552, Nov 1998.

[43] A. Roy, C. Y. Lin, and U. Mohideen. *Phys. Rev. D*, 60:R111101, 1999.

[44] B. W. Harris, F. Chen, and U. Mohideen. *Phys. Rev. A*, 62:052109, 2000.

[45] R. S. Decca, D. López, E. Fischbach, and D. E. Krause. *Phys. Rev. Lett.*, 91(5):050402, Jul 2003.

[46] R. S. Decca, E. Fischbach, G. L. Klimchitskaya, D. E. Krause, D. López, and V. M. Mostepanenko. *Phys. Rev. D*, 68:116003, 2003.

[47] R. S. Decca, D. López, E. Fischbach, G. L. Klimchitskaya, D. E. Krause, and V. M. Mostepanenko. *Ann. Phys. (NY)*, 318:37, 2005.

[48] R. S. Decca, D. López, E. Fischbach, G. L. Klimchitskaya, D. E. Krause, and V. M. Mostepanenko. *Phys. Rev. D*, 75:077101, 2007.

[49] R. S. Decca, D. López, E. Fischbach, G. L. Klimchitskaya, D. E. Krause, and V. M. Mostepanenko. *Eur. Phys. J.*, C 51:963, 2007.

[50] P. J. van Zwol, G. Palasantzas, and J. Th. M. De Hosson. *Appl. Phys. Lett.*, 91(14):–, 2007.

[51] P. J. van Zwol, G. Palasantzas, M. van de Schootbrugge, and J. Th. M. De Hosson. *Appl. Phys. Lett.*, 92(5):054101, 2008.

[52] W. Broer, G. Palasantzas, and J. Knoester. *Phys. Rev. B*, 85:155410, April 2012.

[53] B. A. Lippmann and J. Schwinger. *Phys. Rev.*, 79:469–480, Aug 1950.

[54] O. Kenneth and I. Klich. *Phys. Rev. B*, 78:014103, Jul 2008.

[55] T. Emig, N. Graham, R. L. Jaffe, and M. Kardar. *Phys. Rev. Lett.*, 99:170403, Oct 2007.

[56] K. A. Milton. *American Journal of Physics*, 79:697–711, 2011.

[57] K. A. Milton. *J. Phys. A: Math. Gen.*, 37:R209, 2004.

[58] F. G. Bass and I. M. Fuks. Pergamon, New York, 1979.

[59] L. Mandel and E. Wolf. Cambridge University Press, Cambridge, USA, 1995.

[60] J. A. Ogilvy. *J. Phys. D*, Appl. Phys. 21:260, 1988.

[61] Prachi Parashar. PhD thesis, The University of Oklahoma, USA, 2011.

[62] Herbert M. Fried. MIT Press, Cambridge,Mass., 1972.

[63] G. Palasantzas and J. Th. M. De Hosson. *Phys. Rev. B*, 72(11):115426, Sep 2005.

[64] Wijnand Broer, George Palasantzas, Jasper Knoester, and Vitaly B. Svetovoy. *Europhys. Lett.*, 95(3):30001, 2011.

[65] P. J. van Zwol, V. B. Svetovoy, and G. Palasantzas. *Phys. Rev. B*, 80(23):235401, Dec 2009.

[66] Lowell S. Brown and G. Jordan Maclay. *Phys. Rev.*, 184(5):1272–1279, Aug 1969.

[67] G. R. Dvali, Gregory Gabadadze, and Massimo Porrati. *Phys. Lett.*, B485:208–214, 2000.

[68] Juan Maldacena. *Scientific American*, 293(5):56–63, Nov 2005.

[69] Alex Hamilton, Daniel N. Kabat, Gilad Lifschytz, and David A. Lowe. *Phys.Rev.*, D74:066009, 2006.

[70] Hua Yao Wu and Martin Schaden. *Phys. Rev. D*, 85:045008, Feb 2012.

[71] J. Blocki, J. Randrup, W. J. Swiatecki, and C. F. Tsang. *Ann. Phys. (NY)*, 105(2):427 – 462, 1977.

[72] G. L. Klimchitskaya, Anushree Roy, U. Mohideen, and V. M. Mostepanenko. *Phys. Rev. A*, 60(5):3487–3495, Nov 1999.

[73] H. B. Chan, Y. Bao, J. Zou, R. A. Cirelli, F. Klemens, W. M. Mansfield, and C. S. Pai. *Phys. Rev. Lett.*, 101(3):030401, Jul 2008.

[74] H.-C. Chiu, G. L. Klimchitskaya, V. N. Marachevsky, V. M. Mostepanenko, and U. Mohideen. *Phys. Rev. B*, 81(11):115417, Mar 2010.

[75] P. J. van Zwol, G. Palasantzas, and J. Th. M. De Hosson. *Phys. Rev. B*, 77(7):075412, Feb 2008.

[76] Steven Weinberg. Cambridge University Press, 2005.

[77] D. E. Krause, R. S. Decca, D. López, and E. Fischbach. *Phys. Rev. Lett.*, 98(5):050403, Jan 2007.

[78] J. Gasser and H. Leutwyler. *Ann. Phys. (NY)*, 158(1):142 – 210, 1984.

[79] F. S. S. Rosa, D. A. R. Dalvit, and P. W. Milonni. *Phys. Rev. A*, 78:032117, Sep 2008.

[80] A. Gusso and U. B. Reis. *EPL*, 99:36003, Aug 2012.

[81] I. Cavero-Pelaez, K. A. Milton, P. Parashar, and K. V. Shajesh. *Phys. Rev. D*, 78:065018, 2008.

[82] H. Y. Wu and M. Schaden. *Phys. Rev. D*, 85:045008, Feb 2012.

[83] H. Leutwyler. *Ann. Phys.*, 235(1):165–203, Oct 1994.

[84] Heinz Raether. Springer-Verlag., 1988.

[85] R. Büscher and T. Emig. *Phys. Rev. A*, 69:062101, Jun 2004.

[86] F. Intravaia, S. Koev, W. Jung, A. A. Talin, P. S. Davids, R. S. Decca, V. A. Aksyuk, D. A. R. Dalvit, and D. Lopez. *Nature Communication*, 4:2515, Sep 2013.

[87] B.V. Derjaguin and I.I. Abrikossova. *J. Phys. and Chem. of Sol.*, 5(1-2):1 – 10, 1958.

[88] Alexei A. Maradudin and Paul Mazur. *Phys. Rev. B*, 22(4):1677–1686, Aug 1980.

[89] M. Yu. Novikov, A. S. Sorin, and V. Ya. Chernyak. *Theor. Math. Phys.*, 82:124–130, 1990.

[90] C. Genet, A. Lambrecht, P. Maia Neto, and S. Reynaud. *Europhys. Lett.*, 62(4):484, 2003.

[91] P. A. Maia Neto, A. Lambrecht, and S. Reynaud. *Europhys. Lett.*, 69(6):924, 2005.

[92] P A Maia Neto, Astrid Lambrecht, and Serge Reynaud. *J. Phys. A*, 39(21):6517, 2006.

[93] A. Lambrecht and V. N. Marachevsky. *Phys. Rev. Lett.*, 101:160403, Oct. 2008.

[94] F. Intravaia, P. S. Davids, R. S. Decca, V. A. Aksyuk, D. A. R. Dalvit, and D. Lopez. *Phys. Rev. A*, 86:042101, Oct. 2012.

[95] Peter Becher, Manfred Böhm, and Hans Joos. Wiley, New York, 1984.

[96] Joseph I. Kapusta and Charles Gale. Cambridge University Press, 2006.

Appendix A

A.1 Free Energy of a Massless Scalar Field for Two Flat Parallel Semitransparent Plates

A.1.1 An isolated flat semi-transparent plate

Although this single-body contribution to the free energy does not depend on the separation a between two flat plates, it is finite and does depend on the temperature. We compute it for the sake of completeness.

Using Matsubara's formalism one [20] readily finds that the irreducible contribution to the Helmholtz free energy per unit area, $f^{(1)}$, of a massless scalar field due to a semi-transparent flat plate of area A described by the potential interaction $V(z) = \lambda\delta(z)$ is given by,

$$f^{(1)}(T,\lambda) = \frac{T}{2}\sum_{n=-\infty}^{\infty}\int \frac{d\mathbf{k}}{(2\pi)^2}\ln(1+\frac{\lambda}{2\kappa_n}) \ , \tag{A.1}$$

where T is the temperature and $\kappa_n^2 = (2\pi nT)^2 + \mathbf{k}^2$. Poisson's resummation formula allows one to rewrite Eq.(A.1) in the form,

$$\begin{aligned} f^{(1)}(T,\lambda) &= \frac{1}{2}\sum_{n=-\infty}^{\infty}\int_{-\infty}^{\infty}\frac{d\zeta}{2\pi}\, e^{in\zeta/T}\int\frac{d\mathbf{k}}{(2\pi)^2}\ln(1+\frac{\lambda}{2\kappa}) \\ &= \sum_{n=1}^{\infty}\frac{T}{2\pi^2 n}\int_0^{\infty} d\kappa\,\kappa\sin(n\kappa/T)\ln(1+\frac{\lambda}{2\kappa}) \\ &= \frac{T^3}{2\pi^2}\sum_{n=1}^{\infty}\frac{1}{n^3}\int_0^{\infty} dx\, x\sin(x)\ln(1+\frac{\lambda n}{2Tx}) \ , \end{aligned} \tag{A.2}$$

where the divergent, but temperature-independent, $n = 0$ summand has been dropped by requiring that the free energy vanishes at $T = 0$. This ignores the divergent change in zero-point energy due to insertion of a semitransparent plate. In deriving the second expression of Eq.(A.2) we introduced spherical coordinates with $\kappa^2 = \zeta^2 + \mathbf{k}^2$ and performed the angular integrations. The final expression in Eq.(A.2) is in fact finite. We may perform the summation and reduce the expression for the free energy per unit area of a flat plate to a single integral,

$$
\begin{aligned}
f^{(1)}(T,\lambda) &= \frac{T^3}{2\pi^2}\int_0^\infty \frac{dy}{y}\left[\sum_{n=1}^{\infty}\frac{1-e^{-ny\lambda/(2T)}}{n^3}\right]\int_0^\infty dx\, x\sin(x)e^{-xy} \\
&= \frac{T^3}{\pi^2}\int_0^\infty \frac{dy}{(1+y^2)^2}\left[\zeta(3)-\mathrm{Li}_3(e^{-y\lambda/(2T)})\right] > 0\ . \qquad \text{(A.3)}
\end{aligned}
$$

The asymptotic behavior of $f^{(1)}$ is readily found,

$$
f^{(1)}(T \ll \lambda) \sim \frac{T^3}{4\pi}\zeta(3) \qquad \text{(A.4)}
$$

$$
f^{(1)}(\lambda \ll T) \sim \frac{T^2\lambda}{24} \qquad \text{(A.5)}
$$

For Dirichlet boundary conditions ($\lambda \to \infty$), the asymptotic expression in Eq.(A.4) holds at any temperature. Eq.(A.5) is accurate to leading order in λ for a weakly interacting plate. Note that the free energy of a single semi-transparent plate is positive and *increases* monotonic with temperature for any value of λ. The corresponding contribution to the entropy therefore *decreases* with increasing temperature. However, this ignores the bulk contribution to the entropy which generally overwhelms this reduction. Including the bulk contribution, the total entropy due to insertion of a Dirichlet plate is negative only for $1/T > \frac{(2\pi)^3}{135}V/A \sim 2V/A$. It is negative only when the boundary of the container (on average) is within a thermal wavelength of the plate. Ignoring the finite size of the container in obtaining the entropy change due to the plate is no longer warranted in this situation. Although we here do not quantify the correction, it very likely is perfectly consistent that the entropy change due to insertion of a single plate is negative and decreases as the temperature increases. The negative contribution to the entropy can be qualitatively understood by the fact that the energy difference for excited cavity states increases upon insertion of the plate and the occupation numbers for excited states therefore decrease.

A.1.2 Irreducible contribution to the free energy of a scalar due to two flat parallel semi-transparent plates

We again use Matsubara's formalism and proceed as for a single plate. The irreducible contribution to the free energy per unit area, $f^{(2)}$, due to two semi-transparent parallel plates at separation a is given by,

$$f^{(2)}(T;\lambda,\bar{\lambda},a) = \frac{T}{2}\sum_{n=-\infty}^{\infty}\int \frac{d\mathbf{k}}{(2\pi)^2}\ln(\Delta(\kappa_n)) = \frac{T}{4\pi}\sum_{n=-\infty}^{\infty}\int_{2\pi|n|T}\kappa d\kappa \ln(\Delta(\kappa))\ , \tag{A.6}$$

where $\kappa_n^2 = (2\pi n T)^2 + \mathbf{k}^2$ as before and $\Delta(\kappa)$ is given by Eq.(A.14). Contrary to the irreducible contribution from a single plate, $f^{(2)}$ is finite for any separation $a > 0$. We again use Poisson's resummation formula to express the free energy in dual variables,

$$\begin{aligned} f^{(2)}(T;\lambda,\bar{\lambda},a) &= \frac{1}{2}\sum_{n=-\infty}^{\infty}\int_{-\infty}^{\infty}\frac{d\zeta}{2\pi}\, e^{in\zeta/T}\int\frac{d\mathbf{k}}{(2\pi)^2}\ln(\Delta(\kappa)) \\ &= \frac{1}{2\pi^2}\int_0^\infty d\kappa\,\kappa\left(\frac{\kappa}{2} + T\sum_{n=1}^{\infty}\frac{\sin(n\kappa/T)}{n}\right)\ln(\Delta(\kappa)) \\ &= \frac{T}{2\pi}\int_0^\infty d\kappa\,\kappa\, N(\frac{\kappa}{2\pi T})\,\ln\left(1 - \frac{\lambda\bar{\lambda}e^{-2a\kappa}}{(\lambda+2\kappa)(\bar{\lambda}+2\kappa)}\right)\ . \end{aligned} \tag{A.7}$$

Here $N(x)$ is the staircase function ($[x]$ denoting the largest integer less than x),

$$N(x) := 1/2 + [x] = x + \frac{1}{\pi}\arctan(\cot(\pi x))\ . \tag{A.8}$$

At low temperatures $f^{(2)}$ behaves as,

$$f^{(2)}(2\pi T\tilde{a} \ll 1;\lambda,\bar{\lambda}) \sim \frac{1}{4\pi^2}\int_0^\infty d\kappa\,\kappa^2\ln(\Delta) + A\tilde{a}\frac{\pi^2 T^4}{90}\ , \tag{A.9}$$

where the effective separation $\tilde{a} = a + \frac{1}{\lambda} + \frac{1}{\bar{\lambda}}$. The first term is just the Casimir energy of two semi-transparent plates [81]. Note that the T^4 behavior of the second term is the same as that of the bulk contribution to the free energy. In the Dirichlet limit $\lambda, \bar{\lambda} \sim \infty$ it simply subtracts the contribution to the free energy from the volume between the two plates. This again is qualitatively caused by the increased energy difference to excited states between the plates. The second term in Eq.(A.9) is not correct in the weak coupling limit when $2\pi T \gg \lambda, \bar{\lambda}$. In the range $\lambda, \bar{\lambda} \ll 2\pi T \ll 1/a$ we have that

$$\begin{aligned} & f^{(2)}(\lambda, \bar{\lambda} \ll 2\pi T \ll 1/a) \\ & \sim \frac{\lambda\bar{\lambda}}{32\pi^2 a}\left(1 + 2\pi T a\left(\frac{\bar{\lambda}\ln(T/\bar{\lambda}) - \lambda\ln(T/\lambda)}{\bar{\lambda} - \lambda} + 1.27036\right) - \frac{19}{12}(2\pi T a)^2 + \dots\right. \end{aligned} \tag{A.10}$$

Note that for weak coupling the entropy apparently diverges like $\ln(T)$ for small T. However, there is no violation of Nernst's theorem in this case, because Eq.(A.10) only holds for $2\pi T \gg \lambda, \bar{\lambda}$. For lower temperatures Eq.(A.9) is valid and the entropy vanishes proportional to T^3. The first term of Eq.(A.10) reproduces the leading term of the Casimir energy for two weakly interacting parallel plates [81, 20].

The total free energy $\mathcal{F}^{\|}$, of a massless scalar field in the presence of two parallel flat plates is the sum of the bulk contribution, the irreducible one-body contributions of the individual plates in Eq.(A.3) and the irreducible two-body contribution of Eq.(A.7),

$$\mathcal{F}^{\|}(T; \lambda, \bar{\lambda}, a) = -V\frac{\pi^2 T^4}{90} + A f^{\|}(T; \lambda, \bar{\lambda}, a) \ , \tag{A.11}$$

with

$$f^{\|}(T; \lambda, \bar{\lambda}, a) = f^{(1)}(T, \lambda) + f^{(1)}(T, \bar{\lambda}) + f^{(2)}(T; \lambda, \bar{\lambda}, a) \ . \tag{A.12}$$

We have absorbed a divergent, but temperature- and separation-independent, factor in the normalization of the generating function so that $\mathcal{F}^{\|}$ vanishes at $T = 0$ for widely separated plates.

A.2 Thermal Green's Function of a Scalar in the Presence of Two Parallel Semitransparent Plates

In Matsubara's formalism [62, 95, 96] thermal Green's functions of a mode at temperature T are given by evaluating Euclidean Green's functions at the corresponding Matsubara frequency $\xi_n = 2\pi n T$. We thus can draw on the literature for the Euclidean Green's function of a massless scalar in the presence of two parallel semitransparent plates [81, 16, 20]. The physical solution to Eq.(3.20) is,

$$
\begin{aligned}
&g^{\|}(z,z';\kappa) \qquad\qquad \text{(A.13)}\\
&= \frac{e^{-\kappa|z-z'|}}{2\kappa} - \frac{\Delta^{-1}}{2\kappa}[e^{-\kappa|z-a|}, e^{-\kappa|z|}] \cdot \begin{bmatrix} t & -te^{-\kappa a}\bar{t} \\ -te^{-\kappa a}\bar{t} & \bar{t} \end{bmatrix} \cdot \begin{bmatrix} e^{-\kappa|z'-a|} \\ e^{-\kappa|z'|} \end{bmatrix}\\
&= \frac{e^{-\kappa|z-z'|}}{2\kappa} - \frac{\Delta^{-1}}{2\kappa}\\
&\times \left(te^{-\kappa(|z'-a|+|z-a|)} - t\bar{t}(e^{-\kappa(|z'|+a+|z-a|)} + e^{-\kappa(|z'-a|+a+|z|)}) + \bar{t}e^{-\kappa(|z'|+|z|)} \right),
\end{aligned}
$$

$$
\text{with } \Delta(\kappa) = 1 - t\bar{t}e^{-2\kappa a}\ , \quad t = \frac{\lambda}{2\kappa+\lambda} \ \text{ and } \bar{t} = \frac{\bar{\lambda}}{2\kappa+\bar{\lambda}}\ . \tag{A.14}
$$

Of particular interest to us is the correlation function in momentum space at $z = z' = a$ and its derivatives ($\phi_n'(\mathbf{x}, a) = \frac{\partial}{\partial a}\phi_n(\mathbf{x}, a), \phi_n''(\mathbf{x}, a) = \frac{\partial^2}{\partial a^2}\phi_n(\mathbf{x}, a)$, etc.),

$$\begin{aligned}
\int d\mathbf{x}\, e^{-i\mathbf{k}\mathbf{x}} \langle \phi_n(\mathbf{x},a)\phi_n(0,a)\rangle^{\|} &= \lim_{z,z'\to a} g^{\|}(z,z';\kappa_n) = \frac{1}{\lambda} - \frac{2\kappa t}{\lambda^2 \Delta}\Big|_{\kappa=\kappa_n}, &\text{(A.15a)}\\
\int d\mathbf{x}\, e^{-i\mathbf{k}\mathbf{x}} \langle \phi_n(\mathbf{x},a)\phi_n'(0,a)\rangle^{\|} &= \lim_{z,z'\to a} \partial_{z'} g^{\|}(z,z';\kappa_n) = \frac{\kappa t \bar{t} e^{-2\kappa a}}{\lambda \Delta}\Big|_{\kappa=\kappa_n}, &\text{(A.15b)}\\
\int d\mathbf{x}\, e^{-i\mathbf{k}\mathbf{x}} \langle \phi_n'(\mathbf{x},a)\phi_n'(0,a)\rangle^{\|} &= \lim_{z,z'\to a} \partial_z \partial_{z'} g^{\|}(z,z';\kappa_n) = \frac{\kappa^2}{\lambda} - \frac{\kappa}{2t\Delta}\Big|_{\kappa=\kappa_n}, &\text{(A.15c)}\\
\int d\mathbf{x}\, e^{-i\mathbf{k}\mathbf{x}} \langle \phi_n(\mathbf{x},a)\phi_n''(0,a)\rangle^{\|} &= \lim_{z,z'\to a} \partial_{z'}^2 g^{\|}(z,z';\kappa_n) = \frac{\kappa^2}{\lambda} - \frac{2\kappa^3 t}{\lambda^2 \Delta}\Big|_{\kappa=\kappa_n}, &\text{(A.15d)}\\
\int d\mathbf{x}\, e^{-i\mathbf{k}\mathbf{x}} \langle \phi_n^{(j)}(\mathbf{x},a)\phi_n^{(l)}(0,a)\rangle^{\|} &= \kappa_n^2 \int d\mathbf{x}\, e^{-i\mathbf{k}\mathbf{x}} \langle \phi_n^{(j-2)}(\mathbf{x},a)\phi_n^{(l)}(0,a)\rangle^{\|}, &\text{(A.15e)}
\end{aligned}$$

where the expressions are to be evaluated at the n-th Matsubara frequency ($\kappa \to \kappa_n = \sqrt{(2\pi n T)^2 + \mathbf{k}^2}$). The correlations in Eq.(A.15) are found by taking normal derivatives of Eq.(A.13) and using that $\lim_{s\to 0} \operatorname{sign}(s) = 0$, $\lim_{s\to 0} \operatorname{sign}^2(s) = 1$ and $\lim_{s\to 0} \delta(s) = \lim_{s\to 0} \operatorname{sign}'(s) = 0$. Eq.(A.15e) expresses the fact that Eq.(3.20) relates correlations on the surface of the rough plate to correlations with two fewer normal derivatives of ϕ. Increasing the number of normal derivatives by two amounts to multiplying the Fourier-space correlation function by κ^2. The three correlation functions of Eqs. (A.15a), (A.15b) and (A.15c) thus generate all correlations with a higher number of normal derivatives such as Eq.(A.15d). This allows us to obtain Feynman rules for vertices with an arbitrary number of h-fields.

Appendix B

B.1 The Green's Dyadic for Three Flat Dielectric Slabs

In Schwinger's formalism [25] the parallel-plate Green's dyadic is determined by reduced electric and magnetic Green's functions. In the coordinate system in which $\mathbf{k} = (k, 0)$ points along the +x axis, this Green's dyadic is,

$$\mathbf{G}^{\|}(k, z, z'; \zeta, a) = \begin{bmatrix} -\frac{1}{\varepsilon_z}\frac{\partial}{\partial z}\frac{1}{\varepsilon_{z'}}\frac{\partial}{\partial z'} g_H & 0 & -\frac{ik}{\varepsilon_z \varepsilon_{z'}}\frac{\partial}{\partial z} g_H \\ 0 & \zeta^2 g_E & 0 \\ \frac{ik}{\varepsilon_z \varepsilon_{z'}}\frac{\partial}{\partial z'} g_H & 0 & \frac{1}{\varepsilon_z}\delta(z - z') - \frac{k^2}{\varepsilon_z \varepsilon_{z'}} g_H \end{bmatrix} \tag{B.1}$$

where the g_E and g_H solve the differential equations,

$$\begin{aligned} \Big[-\frac{\partial^2}{\partial z^2} + k^2 + \zeta^2 \varepsilon_z\Big] g_E(k, z, z'; \zeta) &= \delta(z - z') \\ \Big[-\frac{\partial}{\partial z}\frac{1}{\varepsilon_z}\frac{\partial}{\partial z} + \frac{k^2}{\varepsilon_z} + \zeta^2\Big] g_H(k, z, z'; \zeta) &= \delta(z - z') \end{aligned} \tag{B.2}$$

One recovers the Green's function for arbitrary transverse momentum $\mathbf{k}$ by rotation about the z-axis,

$$\begin{aligned} \mathbf{G}^{\|}(\mathbf{k}, z, z'; \zeta, a) &= \mathbf{R} \cdot \mathbf{G}^{\|}(k = |\mathbf{k}|, z, z'; \zeta, a) \cdot \mathbf{R}^T \\ \mathbf{R} &= \frac{1}{k}\begin{pmatrix} k_x & -k_y & 0 \\ k_y & k_x & 0 \\ 0 & 0 & k \end{pmatrix} \end{aligned} \tag{B.3}$$

The solution to Eq.(B.2) in different regions of z and z' will be denoted,

$$g_i(k, z, z'; \zeta) = \begin{bmatrix} g_i^{++}(k, z > 0, z' > 0; \zeta) & g_i^{+-}(k, z > 0, z' < 0; \zeta) \\ g_i^{-+}(k, z < 0, z' > 0; \zeta) & g_i^{--}(k, z < 0, z' < 0; \zeta) \end{bmatrix} \tag{B.4}$$

with $i = E$ or H .

We divide the reduced Green's functions into $g_i^{|}$ for a single flat plate and its correction $g_i^{|a|}$ due to the presence of a parallel flat plate at a distance a:

$$g_i(k,z,z';\zeta,a) = g_i^{|}(k,z,z';\zeta) + g_i^{|a|}(k,z,z';\zeta,a) \tag{B.5}$$

$$g_E^{|}(k,z,z';\zeta) = \begin{bmatrix} \frac{1}{2\kappa_2}\left(e^{-\kappa_2|z-z'|} - r_2 e^{-\kappa_2(z+z')}\right) & \frac{1}{\kappa_2+\kappa_3} e^{\kappa_3 z' - \kappa_2 z} \\ \frac{1}{\kappa_2+\kappa_3} e^{\kappa_3 z - \kappa_2 z'} & \frac{1}{2\kappa_3}\left(e^{-\kappa_3|z-z'|} + r_2 e^{\kappa_3(z+z')}\right) \end{bmatrix}$$

$$g_H^{|}(k,z,z';\zeta) = \begin{bmatrix} \frac{1}{2\bar\kappa_2}\left(e^{-\kappa_2|z-z'|} - \bar r_2 e^{-\kappa_2(z+z')}\right) & \frac{1}{\bar\kappa_2+\bar\kappa_3} e^{\kappa_3 z' - \kappa_2 z} \\ \frac{1}{\bar\kappa_2+\bar\kappa_3} e^{\kappa_3 z - \kappa_2 z'} & \frac{1}{2\bar\kappa_3}\left(e^{-\kappa_3|z-z'|} + \bar r_2 e^{\kappa_3(z+z')}\right) \end{bmatrix}$$

$$\begin{aligned} g_E^{|a|}(k,z,z';\zeta,a) &= \frac{r_1}{e^{2a\kappa_3} - r_1 r_2} \\ &\times \begin{bmatrix} \frac{1}{2\kappa_2}(1-r_2^2) e^{-\kappa_2(z+z')} & \frac{1}{\kappa_2+\kappa_3}\left(e^{-\kappa_2 z - \kappa_3 z'} + r_2 e^{-\kappa_2 z + \kappa_3 z'}\right) \\ \frac{1}{\kappa_2+\kappa_3}\left(e^{-\kappa_2 z' - \kappa_3 z} + r_2 e^{-\kappa_2 z' + \kappa_3 z}\right) & \frac{1}{2\kappa_3}\left(e^{-\kappa_3 z} + r_2 e^{\kappa_3 z}\right)\left(e^{-\kappa_3 z'} + r_2 e^{\kappa_3 z'}\right) \end{bmatrix} \\ g_H^{|a|}(k,z,z';\zeta,a) &= \frac{\bar r_1}{e^{2a\kappa_3} - \bar r_1 \bar r_2} \\ &\times \begin{bmatrix} \frac{1}{2\bar\kappa_2}(1-\bar r_2^2) e^{-\kappa_2(z+z')} & \frac{1}{\bar\kappa_2+\bar\kappa_3}\left(e^{-\kappa_2 z - \kappa_3 z'} + \bar r_2 e^{-\kappa_2 z + \kappa_3 z'}\right) \\ \frac{1}{\bar\kappa_2+\bar\kappa_3}\left(e^{-\kappa_2 z' - \kappa_3 z} + \bar r_2 e^{-\kappa_2 z' + \kappa_3 z}\right) & \frac{1}{2\bar\kappa_3}\left(e^{-\kappa_3 z} + \bar r_2 e^{\kappa_3 z}\right)\left(e^{-\kappa_3 z'} + \bar r_2 e^{\kappa_3 z'}\right) \end{bmatrix} \end{aligned}$$

Note that continuity of E_x, E_y, and εE_z across the flat interface implies that of g_E, g_H, and $\frac{1}{\varepsilon_z}\frac{\partial}{\partial z}\frac{1}{\varepsilon_{z'}}\frac{\partial}{\partial z'} g_H$ are continuous as well. The components of Eq.(B.1) in different regions domains of z and z' are:

$$\tilde{G}^{|}_{xx}(k,z,z';\zeta) = -\frac{1}{\varepsilon_z}\frac{\partial}{\partial z}\frac{1}{\varepsilon_{z'}}\frac{\partial}{\partial z'}g^{|}_H \tag{B.6}$$

$$= \frac{1}{2}\begin{bmatrix} \bar{\kappa}_2(e^{-\kappa_2|z-z'|} + \bar{r}_2 e^{-\kappa_2(z+z')}) & \bar{\kappa}_3(1-\bar{r}_2)e^{-\kappa_2 z+\kappa_3 z'} \\ \bar{\kappa}_3(1-\bar{r}_2)e^{-\kappa_2 z'+\kappa_3 z} & \bar{\kappa}_3(e^{-\kappa_3|z-z'|} - \bar{r}_2 e^{\kappa_3(z+z')}) \end{bmatrix}$$

$$\tilde{G}^{|}_{yy}(k,z,z';\zeta) = \zeta^2 g^{|}_E$$

$$= \zeta^2 \begin{bmatrix} \frac{1}{2\kappa_2}(e^{-\kappa_2|z-z'|} - r_2 e^{-\kappa_2(z+z')}) & \frac{1}{\kappa_2+\kappa_3}e^{\kappa_3 z'-\kappa_2 z} \\ \frac{1}{\kappa_2+\kappa_3}e^{\kappa_3 z-\kappa_2 z'} & \frac{1}{2\kappa_3}(e^{-\kappa_3|z-z'|} + r_2 e^{\kappa_3(z+z')}) \end{bmatrix}$$

$$\tilde{G}^{|}_{zz}(k,z,z';\zeta) = -\frac{k^2}{\varepsilon_z\varepsilon_{z'}}g^{|}_H$$

$$= -k^2 \begin{bmatrix} \frac{1}{2\varepsilon_2\kappa_2}(e^{-\kappa_2|z-z'|} - \bar{r}_2 e^{-\kappa_2(z+z')}) & \frac{1}{\varepsilon_3\kappa_2+\varepsilon_2\kappa_3}e^{\kappa_3 z'-\kappa_2 z} \\ \frac{1}{\varepsilon_3\kappa_2+\varepsilon_2\kappa_3}e^{\kappa_3 z-\kappa_{z2} z'} & \frac{1}{2\varepsilon_3\kappa_3}(e^{-\kappa_3|z-z'|} + \bar{r}_2 e^{\kappa_3(z+z')}) \end{bmatrix}$$

$$\tilde{G}^{|}_{xz}(k,z,z';\zeta) = -\frac{ik}{\varepsilon_z\varepsilon_{z'}}\frac{\partial}{\partial z}g^{|}_H = \frac{ik}{2}$$

$$\times \begin{bmatrix} \frac{1}{\varepsilon_2}(\mathrm{sgn}(z-z')e^{-\kappa_2|z-z'|} - \bar{r}_2 e^{-\kappa_2(z+z')}) & \frac{1}{\varepsilon_3}(1-\bar{r}_2)e^{-\kappa_2 z+\kappa_3 z'} \\ -\frac{1}{\varepsilon_2}(1+\bar{r}_2)e^{-\kappa_2 z'+\kappa_3 z} & \frac{1}{\varepsilon_3}(\mathrm{sgn}(z-z')e^{-\kappa_3|z-z'|} - \bar{r}_2 e^{\kappa_3(z+z')}) \end{bmatrix}$$

$$\tilde{G}^{|}_{zx}(k,z,z';\zeta) = \frac{ik}{\varepsilon_z\varepsilon_{z'}}\frac{\partial}{\partial z'}g^{|}_H = \frac{ik}{2}$$

$$\times \begin{bmatrix} \frac{1}{\varepsilon_2}(\mathrm{sgn}(z-z')e^{-\kappa_2|z-z'|} + \bar{r}_2 e^{-\kappa_2(z+z')}) & \frac{1}{\varepsilon_2}(1+\bar{r}_2)e^{-\kappa_2 z+\kappa_3 z'} \\ -\frac{1}{\varepsilon_3}(1-\bar{r}_2)e^{-\kappa_2 z'+\kappa_3 z} & \frac{1}{\varepsilon_3}(\mathrm{sgn}(z-z')e^{-\kappa_3|z-z'|} + \bar{r}_2 e^{\kappa_3(z+z')}) \end{bmatrix}$$

The corresponding separation-dependent part is,

$$G^{|a|}_{xx}(k,z,z';\zeta,a) = \frac{-\bar{r}_1}{2(e^{2a\kappa_3}-\bar{r}_1\bar{r}_2)} \tag{B.7}$$
$$\times \begin{bmatrix} \bar{\kappa}_2(1-\bar{r}_2^2)e^{-\kappa_2(z+z')} & \bar{\kappa}_3(e^{-\kappa_2 z}-\bar{r}_2 e^{-\kappa_2 z})(e^{-\kappa_3 z'}-\bar{r}_2 e^{\kappa_3 z'}) \\ \bar{\kappa}_3(e^{-\kappa_2 z'}-\bar{r}_2 e^{-\kappa_2 z'})(e^{-\kappa_3 z}-\bar{r}_2 e^{\kappa_3 z}) & \bar{\kappa}_3(e^{-\kappa_3 z}-\bar{r}_2 e^{\kappa_3 z})(e^{-\kappa_3 z'}-\bar{r}_2 e^{\kappa_3 z'}) \end{bmatrix}$$
$$G^{|a|}_{yy}(k,z,z';\zeta,a) = \frac{\zeta^2 r_1}{e^{2a\kappa_3}-r_1 r_2}$$
$$\times \begin{bmatrix} \frac{1}{2\kappa_2}(1-r_2^2)e^{-\kappa_2(z+z')} & \frac{1}{\kappa_2+\kappa_3}(e^{-\kappa_2 z-\kappa_3 z'}+r_2 e^{-\kappa_2 z+\kappa_3 z'}) \\ \frac{1}{\kappa_2+\kappa_3}(e^{-\kappa_2 z'-\kappa_3 z}+r_2 e^{-\kappa_2 z'+\kappa_3 z}) & \frac{1}{2\kappa_3}(e^{-\kappa_3 z}+r_2 e^{\kappa_3 z})(e^{-\kappa_3 z'}+r_2 e^{\kappa_3 z'}) \end{bmatrix}$$
$$G^{|a|}_{zz}(k,z,z';\zeta,a) = \frac{-k^2\bar{r}_1}{e^{2a\kappa_3}-\bar{r}_1\bar{r}_2}$$
$$\times \begin{bmatrix} \frac{1}{2\varepsilon_2\kappa_2}(1-\bar{r}_2^2)e^{-\kappa_2(z+z')} & \frac{1}{\varepsilon_3\kappa_2+\varepsilon_2\kappa_3}(e^{-\kappa_2 z-\kappa_3 z'}+\bar{r}_2 e^{-\kappa_2 z+\kappa_3 z'}) \\ \frac{1}{\varepsilon_3\kappa_2+\varepsilon_2\kappa_3}(e^{-\kappa_2 z'-\kappa_3 z}+\bar{r}_2 e^{-\kappa_2 z'+\kappa_3 z}) & \frac{1}{2\varepsilon_3\kappa_3}(e^{-\kappa_3 z}+\bar{r}_2 e^{\kappa_3 z})(e^{-\kappa_3 z'}+\bar{r}_2 e^{\kappa_3 z'}) \end{bmatrix}$$
$$G^{|a|}_{xz}(k,z,z';\zeta,a) = \frac{ik\bar{r}_1}{2(e^{2a\kappa_3}-\bar{r}_1\bar{r}_2)}$$
$$\times \begin{bmatrix} \frac{1}{\varepsilon_2}(1-\bar{r}_2^2)e^{-\kappa_2(z+z')} & \frac{1}{\varepsilon_3}(e^{-\kappa_2 z}-\bar{r}_2 e^{-\kappa_2 z})(e^{-\kappa_3 z'}+\bar{r}_2 e^{\kappa_3 z'}) \\ \frac{1}{\varepsilon_2}(e^{-\kappa_3 z}-\bar{r}_2 e^{\kappa_3 z})(e^{-\kappa_2 z'}+\bar{r}_2 e^{-\kappa_2 z'}) & \frac{1}{\varepsilon_3}(e^{-\kappa_3 z}-\bar{r}_2 e^{\kappa_3 z})(e^{-\kappa_3 z'}+\bar{r}_2 e^{\kappa_3 z'}) \end{bmatrix}$$
$$G^{|a|}_{zx}(k,z,z';\zeta,a) = \frac{-ik\bar{r}_1}{2(e^{2a\kappa_3}-\bar{r}_1\bar{r}_2)}$$
$$\begin{bmatrix} \frac{1}{\varepsilon_2}(1-\bar{r}_2^2)e^{-\kappa_2(z+z')} & \frac{1}{\varepsilon_2}(e^{-\kappa_2 z}+\bar{r}_2 e^{-\kappa_2 z})(e^{-\kappa_3 z'}-\bar{r}_2 e^{\kappa_3 z'}) \\ \frac{1}{\varepsilon_3}(e^{-\kappa_2 z'}-\bar{r}_2 e^{-\kappa_2 z'})(e^{-\kappa_3 z}+\bar{r}_2 e^{\kappa_3 z}) & \frac{1}{\varepsilon_3}(e^{-\kappa_3 z}+\bar{r}_2 e^{\kappa_3 z})(e^{-\kappa_3 z'}-\bar{r}_2 e^{\kappa_3 z'}) \end{bmatrix}$$

The limits of these propagators as z and z' approach 0 are of particular interest. In this case the components of the matrices $\tilde{\mathbf{G}}^{|}(k;\zeta) := \tilde{\mathbf{G}}^{|}(k,0,0;\zeta)$ and

$\mathbf{G}^{|a|}(k;\zeta,a) := \mathbf{G}^{|a|}(k,0,0;\zeta,a)$ simplify to,

$$\tilde{G}^{|}_{xx}(k;\zeta) = \frac{\kappa_2\kappa_3}{\varepsilon_2\kappa_3+\varepsilon_3\kappa_2}\begin{bmatrix}1 & 1\\ 1 & 1\end{bmatrix} \tag{B.8}$$

$$G^{|a|}_{xx}(k;\zeta,a) = \frac{-\bar{r}_1(1-\bar{r}_2^2)\kappa_2}{2(e^{2a\kappa_3}-\bar{r}_1\bar{r}_2)\varepsilon_2}\begin{bmatrix}1 & 1\\ 1 & 1\end{bmatrix}$$

$$\tilde{G}^{|}_{yy}(k;\zeta) = \frac{\zeta^2}{\kappa_2+\kappa_3}\begin{bmatrix}1 & 1\\ 1 & 1\end{bmatrix}$$

$$G^{|a|}_{yy}(k;\zeta,a) = \frac{r_1(1-r_2^2)\zeta^2}{2(e^{2a\kappa_3}-r_1r_2)\kappa_2}\begin{bmatrix}1 & 1\\ 1 & 1\end{bmatrix}$$

$$\tilde{G}^{|}_{zz}(k;\zeta) = \frac{-k^2}{\varepsilon_2\kappa_3+\varepsilon_3\kappa_2}\begin{bmatrix}\varepsilon_3/\varepsilon_2 & 1\\ 1 & \varepsilon_2/\varepsilon_3\end{bmatrix}$$

$$G^{|a|}_{zz}(k;\zeta,a) = \frac{-\bar{r}_1(1-\bar{r}_2^2)k^2}{2(e^{2a\kappa_3}-\bar{r}_1\bar{r}_2)\kappa_2\varepsilon_3}\begin{bmatrix}\varepsilon_3/\varepsilon_2 & 1\\ 1 & \varepsilon_2/\varepsilon_3\end{bmatrix}$$

$$\tilde{G}^{|}_{xz}(k;\zeta) = \frac{ik}{\varepsilon_2\kappa_3+\varepsilon_3\kappa_2}\begin{bmatrix}\varepsilon_3\bar{\kappa}_2 & \kappa_2\\ -\kappa_3 & -\varepsilon_2\bar{\kappa}_3\end{bmatrix}$$

$$G^{|a|}_{xz}(k;\zeta,a) = \frac{i\bar{r}_1(1-\bar{r}_2^2)k}{2(e^{2a\kappa_3}-\bar{r}_1\bar{r}_2)}\begin{bmatrix}1/\varepsilon_2 & 1/\varepsilon_3\\ 1/\varepsilon_2 & 1/\varepsilon_3\end{bmatrix}$$

$$\tilde{G}^{|}_{zx}(k;\zeta) = \frac{-ik}{\varepsilon_2\kappa_3+\varepsilon_3\kappa_2}\begin{bmatrix}\varepsilon_3\bar{\kappa}_2 & -\kappa_3\\ \kappa_2 & -\varepsilon_2\bar{\kappa}_3\end{bmatrix}$$

$$G^{|a|}_{zx}(k;\zeta,a) = \frac{-i\bar{r}_1(1-\bar{r}_2^2)k}{2(e^{2a\kappa_3}-\bar{r}_1\bar{r}_2)}\begin{bmatrix}1/\varepsilon_2 & 1/\varepsilon_2\\ 1/\varepsilon_3 & 1/\varepsilon_3\end{bmatrix}.$$

B.2 Signed Correlators of the Roughness Profile

We here obtain the correlation functions of positive and negative components of the roughness profile for a Gaussian generating functional of roughness correlation functions,

$$\langle e^{\int d\mathbf{x}\alpha(\mathbf{x})h(\mathbf{x})}\rangle = e^{\frac{1}{2}\int d\mathbf{x}d\mathbf{y}\alpha(\mathbf{x})D_2(\mathbf{x}-\mathbf{y})\alpha(\mathbf{y})} , \tag{B.9}$$

that is fully determined by the two-point correlation function $\langle h(\mathbf{x})h(\mathbf{y})\rangle = D_2(\mathbf{x}-\mathbf{y})$. We in the following assume that $D_2(0) \geq D_2(\mathbf{x}-\mathbf{y}) > 0$.

Exploiting an integral representation of the $x\theta(x)$ distribution, one has that

$$\begin{aligned} h_\pm(\mathbf{x}) = h(\mathbf{x})\theta(\pm h(\mathbf{x})) &= \pm\frac{1}{2\pi}\lim_{\varepsilon\to 0^+}\int_{-\infty}^{\infty}\frac{d\beta}{(\beta-i\varepsilon)^2}e^{\pm i\beta h(\mathbf{x})} \\ &= \mp\lim_{\varepsilon\to 0^+}\int_0^\infty \lambda d\lambda e^{-\varepsilon\lambda}\int_{-\infty}^{\infty}\frac{d\beta}{2\pi}e^{-i\lambda\beta}e^{\pm i\beta h(\mathbf{x})} . \end{aligned} \tag{B.10}$$

We use Eq.(B.10) to write,

$$\begin{aligned} &\langle h_+(\mathbf{x})h_\pm(\mathbf{y})\rangle \\ &= \pm\lim_{\varepsilon\to 0^+}\int_0^\infty \lambda_1 d\lambda_1\int_0^\infty \lambda_2 d\lambda_2 e^{-\varepsilon(\lambda_1+\lambda_2)}\int\frac{d\beta}{(2\pi)^2}e^{-i\lambda\cdot\beta}\langle e^{i(\beta_1 h(\mathbf{x})\pm\beta_2 h(\mathbf{y}))}\rangle \end{aligned} \tag{B.11}$$

The expectation in Eq.(B.11) is of the form given in Eq.(B.9) with $\alpha(\mathbf{x}') = i(\beta_1\delta(\mathbf{x}'-\mathbf{x}) \pm \beta_2\delta(\mathbf{x}'-\mathbf{y}))$ and therefore evaluates to,

$$\langle e^{i(\beta_1 h(\mathbf{x})\pm\beta_2 h(\mathbf{y}))}\rangle = e^{-\frac{1}{2}\beta^T\cdot M_\pm\cdot\beta} , \tag{B.12}$$

where the symmetric real, and positive 2×2 matrix,

$$M_\pm = \begin{bmatrix} D_2(0) & \pm D_2(\mathbf{x}-\mathbf{y}) \\ \pm D_2(\mathbf{x}-\mathbf{y}) & D_2(0) \end{bmatrix} \tag{B.13}$$

has determinant $\det M_\pm = D_2^2(0) - D_2^2(\mathbf{x}-\mathbf{y}) > 0$ for $|\mathbf{x}-\mathbf{y}| > 0$. Performing the two-dimensional Gaussian integral in $\beta = (\beta_1,\beta_2)$ (for $|\mathbf{x}-\mathbf{y}| > 0$) gives,

$$\langle h_+(\mathbf{x})h_\pm(\mathbf{y})\rangle = \pm\frac{(\det M_\pm)^{-1/2}}{2\pi}\int_0^\infty d\lambda_1\int_0^\infty d\lambda_2\lambda_1\lambda_2 e^{-\frac{1}{2}\lambda^T\cdot M_\pm^{-1}\cdot\lambda} . \tag{B.14}$$

Converting to polar coordinates $(\lambda_1, \lambda_2) = \lambda(\cos\theta, \sin\theta)$ and noting that the integral extends over the first quadrant with $0 < \theta < \pi/2$ only,

$$
\begin{aligned}
&\langle h_+(\mathbf{x}) h_\pm(\mathbf{y})\rangle \\
&= \pm\frac{(\det M_\pm)^{-1/2}}{2\pi}\int_0^{\pi/2} d\theta \frac{\sin(2\theta)}{2}\int_0^\infty \lambda^3 d\lambda e^{-\frac{1}{2}\lambda^2(D_2(0)\mp\sin(2\theta)D_2(\mathbf{x}-\mathbf{y}))/\det M_\pm} \\
&= \pm\frac{(\det M_\pm)^{3/2}}{4\pi}\int_0^{\pi} d\theta \frac{\sin\theta}{(D_2(0)\mp D_2(\mathbf{x}-\mathbf{y})\sin\theta)^2} \\
&= \pm\frac{D_2(0)}{2\pi}(\sin\phi + (\frac{\pi}{2}\pm\frac{\pi}{2}-\phi)\cos\phi) \qquad \text{(B.15)}
\end{aligned}
$$

with $\cos\phi = D_2(\mathbf{x}-\mathbf{y})/D_2(0), 0 < \phi < \pi/2$. This result is reproduced in Eq.(4.43). The last expression uses that the lengths $D_2(0), D_2(\mathbf{x}-\mathbf{y})$ and $\det M_\pm$ can be interpreted as the sides of a right triangle with hypotenuse $D_2(0)$.

B.3 Angular Integrals

For the class of correlations functions,

$$D_s(q) = 2\pi\sigma^2 l_c^2 (1 + q^2 l_c^2/(2s))^{-1-s} \quad \text{with} \quad s > 0, \qquad \text{(B.16)}$$

the angular integrals of Eqs. (4.62), (4.64), (4.69) and (4.70) are all of the form,

$$
\begin{aligned}
A_n(s) &= \int_{-\pi}^{\pi} \frac{d\theta \cos^n\theta}{(1+a-b\cos\theta)^{s+1}} \qquad \text{(B.17)} \\
&= \frac{\Gamma(s+1-n)}{\Gamma(s+1)}\frac{\partial^n}{\partial b^n}\frac{2\pi}{(1+a+b)^{s+1-n}}\ {}_2F_1(\tfrac{1}{2}, s+1-n; 1; \frac{2b}{1+a+b}),
\end{aligned}
$$

with $a = \frac{1}{2}(k^2 + k'^2)l_c^2/s \geq b = kk' l_c^2/s > 0$ and $n = 0, 1, 2$. They are given by values of the generalized hypergeometric function ${}_2F_1(\frac{1}{2}, \nu; 1; x)$ for any $s > 0$.

The exponential roughness correlation D_{Exp} of Eq.(4.49) corresponds to $s =$

1/2 and the relevant angular integrals in this case are complete elliptic integrals,

$$\begin{aligned} A_0(1/2) &= \frac{4}{(1+a-b)\sqrt{1+a+b}} E(\frac{2b}{1+a+b}) \\ A_1(1/2) &= \frac{4}{(1+a-b)b\sqrt{1+a+b}} \\ &\times \left((1+a)E(\frac{2b}{1+a+b}) - (1+a-b)K(\frac{2b}{1+a+b})\right) \\ A_2(1/2) &= \frac{4}{(1+a-b)b^2\sqrt{1+a+b}} \\ &\times \left((2(1+a)^2-b^2)E(\frac{2b}{1+a+b}) - 2(1+a)(1+a-b)K(\frac{2b}{1+a+b})\right) \end{aligned} \tag{B.18}$$

with $a = (k^2 + k'^2)l_c^2$ and $b = 2kk'l_c^2$.

The limit $s \to \infty$ of the Gaussian correlation in Eq.(4.46) is best obtained directly. The angular integrals in this limit are,

$$\begin{aligned} A_n(\infty) &= e^{-l_c^2(k^2+k'^2)/2} \int_{-\pi}^{\pi} d\theta \cos^n\theta \; e^{l_c^2 kk' \cos\theta} \\ &= 2\pi e^{-l_c^2(k^2+k'^2)/2} \left. \frac{\partial^n}{\partial\alpha^n} I_0(\alpha) \right|_{\alpha=l_c^2 kk'}, \end{aligned} \tag{B.19}$$

where $I_0(x)$ is the modified Bessel function of the first kind of 0-th order. The relevant angular integrals for Gaussian roughness correlation thus are,

$$\begin{aligned} A_0(\infty) &= 2\pi e^{-l_c^2(k^2+k'^2)/2} I_0(l_c^2 kk') \\ A_1(\infty) &= 2\pi e^{-l_c^2(k^2+k'^2)/2} I_1(l_c^2 kk') \\ A_2(\infty) &= \pi e^{-l_c^2(k^2+k'^2)/2} (I_0(l_c^2 kk') + I_2(l_c^2 kk')) \end{aligned} \tag{B.20}$$

B.4 The Response Function

The roughness correction to the Casimir free energy of order σ^2 is given in Eq.(4.58). This correction is linear in $D(q)$ and one may define [3] the response function $R_T(q,a)$ of Eq.(4.88) defined by,

$$\begin{aligned} \Delta F_T^{Cas}[a] &= \tfrac{1}{2}\langle \mathrm{Tr}\tilde{\mathbf{V}}^h \mathbf{G}^{|a|}\rangle - \tfrac{1}{2}\langle \mathrm{Tr}\tilde{\mathbf{V}}^h \tilde{\mathbf{G}}^{|}\tilde{\mathbf{V}}^h \mathbf{G}^{|a|}\rangle + \tfrac{1}{2}\mathrm{Tr}\delta\tilde{\mathbf{V}}^h \mathbf{G}^{|a|} - \tfrac{1}{4}\langle \tilde{\mathbf{V}}^h \mathbf{G}^{|a|}\tilde{\mathbf{V}}^h \mathbf{G}^{|a|}\rangle \\ &= \int_0^\infty \frac{q\,dq}{2\pi} D(q) R_T(q,a) \end{aligned} \tag{B.21}$$

To obtain $R_T(q,a)$ we change the integration variable from $\mathbf{k}'$ to $\mathbf{q} = \mathbf{k}' - \mathbf{k}$ in Eqs. (4.59), (4.62), (4.66) and (4.64) and choose $\mathbf{k} = (k, 0)$ to define the positive x-axis. In these coordinates $k'_x = k + q\cos\theta, k'_y = q\sin\theta$ and explicit expressions for the response function $R_T(q,a)$ can be read off from,

$$
\begin{aligned}
&\tfrac{1}{2}\langle \mathrm{Tr}\tilde{\mathbf{V}}^h \mathbf{G}^{|a|}\rangle && \text{(B.22a)}\\
&\quad = \int_0^\infty \frac{qdq}{2\pi} D(q) \sum_n (-AT) \int_0^\infty \frac{kdk}{2\pi} \kappa\kappa_\varepsilon \Big(\frac{\bar{r}^2}{e^{2a\kappa} - \bar{r}^2} + \frac{r^2}{e^{2a\kappa} - r^2}\Big) \\
&- \tfrac{1}{2}\langle \mathrm{Tr}\tilde{\mathbf{V}}^h \tilde{\mathbf{G}}^{|}\tilde{\mathbf{V}}^h \mathbf{G}^{|a|}\rangle && \text{(B.22b)}\\
&\quad = \int_0^\infty \frac{qdq}{(2\pi)^2} D(q) \sum_n (-AT)(\varepsilon - 1)^2 \int_0^\infty \frac{kdk}{2\pi} \int_{-\pi}^{\pi} d\theta \\
&\quad \times \Big[\frac{r(1-r^2)\zeta^2}{4(e^{2a\kappa} - r^2)\kappa_\varepsilon} \times \left(\frac{\kappa'\kappa'_\varepsilon}{\varepsilon\kappa' + \kappa'_\varepsilon} \Big(\frac{k'_y}{k'}\Big)^2 + \frac{\zeta^2}{\kappa' + \kappa'_\varepsilon} \Big(\frac{k'_x}{k'}\Big)^2 \right) \\
&\quad + \frac{\bar{r}(1-\bar{r}^2)}{4(e^{2a\kappa} - \bar{r}^2)\varepsilon} \left(\frac{\varepsilon k^2 k'^2}{\kappa_\varepsilon(\varepsilon\kappa' + \kappa'_\varepsilon)} - kk'_x\bar{r}' - \frac{\kappa_\varepsilon\kappa'\kappa'_\varepsilon}{\varepsilon\kappa' + \kappa'_\varepsilon} \Big(\frac{k'_x}{k'}\Big)^2 - \frac{\kappa_\varepsilon\zeta^2}{\kappa' + \kappa'_\varepsilon} \Big(\frac{k'_y}{k'}\Big)^2 \right) \Big] \\
&- \tfrac{1}{4}\langle \mathrm{Tr}\tilde{\mathbf{V}}^h \tilde{\mathbf{G}}^{|a|}\tilde{\mathbf{V}}^h \mathbf{G}^{|a|}\rangle && \text{(B.22c)}\\
&\quad = \int_0^\infty \frac{qdq}{(2\pi)^2} D(q) \sum_n (-AT)(\varepsilon - 1)^2 \int_0^\infty \frac{kdk}{2\pi} \int_{-\pi}^{\pi} d\theta \\
&\quad \times \Big[\frac{r(1-r^2)\zeta^2}{16(e^{2a\kappa} - r^2)\kappa_\varepsilon} \left(\frac{r'(1-r'^2)\zeta^2}{(e^{2a\kappa'} - r'^2)\kappa'_\varepsilon} \Big(\frac{k'_x}{k'}\Big)^2 - \frac{2\bar{r}'(1-\bar{r}'^2)\kappa'_\varepsilon}{(e^{2a\kappa'} - \bar{r}'^2)\varepsilon} \Big(\frac{k'_y}{k'}\Big)^2 \right) \\
&\quad + \frac{\bar{r}\bar{r}'(1-\bar{r}^2)(1-\bar{r}'^2)}{16(e^{2a\kappa} - \bar{r}^2)(e^{2a\kappa'} - \bar{r}'^2)} \left(\frac{k^2k'^2}{\kappa_\varepsilon\kappa'_\varepsilon} + \frac{2kk'_x}{\varepsilon} + \frac{\kappa_\varepsilon\kappa'_\varepsilon}{\varepsilon^2} \Big(\frac{k'_x}{k'}\Big)^2 \right) \Big] \\
&\tfrac{1}{2}\mathrm{Tr}\delta\tilde{\mathbf{V}}\mathbf{G}^{|a|} && \text{(B.22d)}\\
&\quad = \int_0^\infty \frac{qdq}{2\pi} D(q) \sum_n AT(\varepsilon - 1)^2 \int_0^\infty \frac{kdk}{2\pi} \\
&\quad \times \Big[\frac{\bar{r}(1-\bar{r}^2)}{4(e^{2a\kappa} - \bar{r}^2)} \frac{k^2q^2}{\kappa_\varepsilon(\varepsilon\kappa' + \kappa'_\varepsilon)} \\
&\quad + \left(\frac{r(1-r^2)\zeta^2}{4(e^{2a\kappa} - r^2)\kappa_\varepsilon} - \frac{\bar{r}(1-\bar{r}^2)\kappa_\varepsilon}{4(e^{2a\kappa} - \bar{r}^2)\varepsilon} \right) \left(\frac{\kappa'\kappa'_\varepsilon/2}{\varepsilon\kappa' + \kappa'_\varepsilon} + \frac{\zeta^2/2}{\kappa' + \kappa'_\varepsilon} - \frac{g^2\zeta}{1+\sqrt{\varepsilon}} \right) \Big]
\end{aligned}
$$

In the last (counter term) expression of Eq.(B.22d) $\kappa' = \sqrt{\mathbf{q}^2 + \zeta^2}$ and $\kappa'_\varepsilon = \sqrt{\mathbf{q}^2 + \zeta^2\varepsilon(\zeta)}$. Note that the angular integration in these coordinates cannot be performed analytically.

Hua-Yao Wu C.V. Jul. 2014

Personal Details and Contact Information

Birth date: 09/Octorber/1980
Nationality: Taiwan
Physics Department, Rutgers University
Room 211, Smith Hall
101 Warren Street
Newark, NJ 07102, USA
TEL: +1(973)-204-1788 (cell)
EMAIL: huayaowu@physics.rutgers.edu

Education

- 2009 - 2014: **Ph.D.** (expected) in Physics, Rutgers, The State University of New Jersey, USA
- 2003 - 2005: **M.S.** in Mechanical Engineering, National Taiwan University, TW
- 1999 - 2003: **B.S.** in Mechanical Engineering, National Taiwan University, TW

Conferences and Workshops

- **Casimir Workshop 2014 at Ecole de Physique**, March 30 – April 4, 2014, Les Houches, France
- **APS DAMOP Meeting** "Renormalized Perturbative Corrections to Casimir Energies due to the Roughness of a Dielectric Plate and Finite Temperature – An Effective Field Theory Approach," June 3 – 7, 2013, Quebec City, Canada
- **PASI on "Frontiers of Casimir Physics,"** October 6 – 17, 2012, Ushuaia, Argentina
- **Casimir Workshop 2012 at Lorentz Center,** March 5 – 16, 2012, Leiden, The Netherlands

Teaching Experience

- Teaching Assistant Fellowship in physics at Rutgers University, 2009 - present

Publications

1. H. Y. Wu, and M. Schaden, "Field Theoretic Approach to Roughness Corrections," Phys. Rev. D **85**, 045008 (2012)

2. H. Y. Wu, and M. Schaden, "Perturbative Roughness Corrections to Electromagnetic Casimir Energies," Phys. Rev. D **89**, 105003 (2014)